FACULTY OF ENGINEERING
AND ARCHITECTURE

Spray Modeling for Medium Speed Diesel Engines

Haohan Li

Doctoral dissertation submitted to obtain the academic degree of
Doctor of Electromechanical Engineering

Supervisors

Prof. Sebastian Verhelst, PhD* - Prof. Tarek Beji, PhD**

* Department of Electromechanical, Systems and Metal Engineering
Faculty of Engineering and Architecture, Ghent University

** Department of Structural Engineering and Building Materials
Faculty of Engineering and Architecture, Ghent University

October 2021

GHENT
UNIVERSITY

FACULTY OF ENGINEERING
AND ARCHITECTURE

Spray Modeling for Medium Speed Diesel Engines

Haohan Li

Doctoral dissertation submitted to obtain the academic degree of
Doctor of Electromechanical Engineering

Supervisors
Prof. Sebastian Verhelst, PhD* - Prof. Tarek Beji, PhD**

* Department of Electromechanical, Systems and Metal Engineering
Faculty of Engineering and Architecture, Ghent University

** Department of Structural Engineering and Building Materials
Faculty of Engineering and Architecture, Ghent University

October 2021

GHENT
UNIVERSITY

ISBN 978-94-6355-538-8
NUR 977, 969
Wettelijk depot: D/2021/10.500/86

Members of the Examination Board

Chair

Prof. Hennie De Schepper, PhD, Ghent University

Other members entitled to vote

Prof. Xue-Song Bai, PhD, Lund University, Sweden
Prof. Francesco Contino, PhD, Université catholique de Louvain
Toon Demeester, PhD, Ghent University
Prof. Steven Lecompte, PhD, Ghent University

Supervisors

Prof. Sebastian Verhelst, PhD, Ghent University
Prof. Tarek Beji, PhD, Ghent University

"Scientists discover the world that exists; engineers create the world that never was."

THEODORE VON KARMAN

Acknowledgments

Doing a Ph.D. is not an easy task, at least for me. In the past years, I got a lot of support and help from the kind people around me.

First, I would like to express my sincere gratitude to Prof. Sebastian Verhelst. I know Prof. Verhelst put much time and effort to supervise me even though he has a very busy schedule. In the past four years, my knowledge width, depth, and horizon have benefited much from Prof. Verhelst. My scientific writing has improved significantly after his revision. I also have gained a better knowledge of the internal combustion engine and its future development under his supervision.

Also, my co-promoter, Prof. Tarek Beji, is the one I want to thank. Prof. Beji always encourages me to think more about the physics behind the phenomena, which also improves my learning skills.

I would like to express my gratitude to the jury members for the effort and time put in. I have greatly benefited from these comments.

I also want to thank the ICE group at Politecnico di Milano, especially Prof. Tommaso Lucchini, for sharing the codes and giving me technical support using OpenFOAM.

My dear colleagues, Tom, Jeroen, Ward, Yi-Hao, Louis, Gilles, Roel, Stijn, Ahmed, Khanh also offered me much support in my work and daily life. My thanks also go to the ladies (Annie, Annick, Griet) and gentlemen (Yves, Koen, Thomas, Frederik) of the STFES group. I really enjoy the time with these nice people.

Last but not least, I would like to express my gratitude to my family for their endless love, support, and encouragement.

Ghent, October 2021
Haohan Li

Table of Contents

Nomenclature

Symbols

Δh_{evap}	latent heat of evaporation	J/kg
$\dot{Q}_d$	heat rate transferred to liquid droplet	W
$\dot{Q}_h$	heat rate transferred that results in the temperature rise	W
$\dot{Q}_{evap}$	heat rate transferred that results in evaporation	W
$\dot{S}_k$	source term of turbulent energy	$kg/(m^2\ s^3)$
$\dot{S}_M$	source term of momentum exchange	$kg/(m^2\ s^2)$
$\dot{S}_p$	source term of mass exchange	$kg/(m^3\ s)$
$\dot{S}_Q$	source term of energy exchange	$J/(m^3\ s)$
$\dot{S}_\varepsilon$	source term of turbulent energy dissipation rate	$kg/(m\ s^4)$
$\dot{S}_{p,i}$	source term of species *i* due to evaporation	$kg/(m^3\ s)$
$\tilde{S}$	dimensionless penetration length	–
$\tilde{t}$	dimensionless time	–
A	area	m^2
B	model constant of KH mechanism	–
C_a	area contraction coefficient	–
C_d	drag coefficient	–
C_v	velocity coefficient	–
C_{dc}	discharge coefficient	–
$c_{p,l}$	specific heat of liquid droplet	J/(kg K)
$c_{p,v}$	specific heat of fuel vapor	J/(kg K)
C_{RT}	RT model constant	–

D_d	droplet diameter	m
D_n	nozzle diameter	m
D_t	turbulent diffusion coefficient	m^2/s
F_{darg}	drag force	N
G	production rate of turbulent energy	$kg/(m^2\ s^3)$
g	gravitational acceleration	m/s^2
h	enthalpy	J/kg
k	turbulent kinetic energy	m^2/s^2
k_h	mixture thermal conductivity	W/(m K)
L_{bu}	breakup length	m
m_d	droplet mass	kg
Nu	Nusselt number	–
Oh	Ohnesorge number	–
$p_{v,\infty}$	partial fuel vapor pressure far from the droplet surface	Pa
$p_{v,\infty}$	partial fuel vapor pressure at the droplet surface	Pa
Pr	Prandtl number	–
r	radius of parent droplet	m
r_c	radius of child droplet	m
R_v	gas constant for fuel vapor	J/(kg K)
Re	Reynolds number	–
Sc	Schmidt number	–
Sh	Sherwood number	–
t	time	s
T_d	droplet temperature	K
T_g	ambient gas temperature (constant value)	K
T_m	mean temperature	K
t_{bu}	breakup time	s
Ta	Taylor number	–
U	velocity of gas phase	m/s
u_d	droplet velocity	m/s
V_0	initial velocity	m/s
We	Weber number	–
X	mole fraction	–
Y_i	mass fraction of species i	–

Greek symbols

α	thermal diffusivity	$\mathrm{kg/(m\,s)}$
α_t	turbulent thermal diffusivity	$\mathrm{kg/(m\,s)}$
δ	ratio of penetration length and nozzle diameter	–
Λ_KH	wavelength of KH mechanism	m
Λ_RT	wavelength of RT mechanism	m
$\mathcal{D}$	mass diffusion coefficient	$\mathrm{m^2/s}$
μ	gas dynamic molecular viscosity	$\mathrm{kg/(m\,s)}$
μ_l	liquid viscosity	$\mathrm{kg/(m\,s)}$
μ_t	turbulent viscosity of gas phase	$\mathrm{kg/(m\,s)}$
Ω_KH	wave growth rate of KH mechanism	$\mathrm{s^{-1}}$
Ω_RT	wave growth rate of RT mechanism	$\mathrm{s^{-1}}$
ϕ	equivalence ratio	–
ρ	gas density	$\mathrm{kg/m^3}$
ρ_d	droplet density	$\mathrm{kg/m^3}$
ρ_g	gas density (constant value)	$\mathrm{kg/m^3}$
ρ_l	liquid fuel density (constant value)	$\mathrm{kg/m^3}$
ρ_m	density of gas and fuel mixture	$\mathrm{kg/m^3}$
ρ_nor	normalized density	–
σ	surface tension	$\mathrm{kg/s^2}$
σ_i	scattering cross section	–
σ_m	standard deviation of distribution function	–
τ	time scale	s
τ_u	momentum relaxation time	s
τ_evap	evaporation relaxation time	s
τ_RT	RT breakup time	s
θ	spreading angle of spray	deg
$\tilde{\rho}$	ratio of liquid fuel density and ambient gas density	–
ε	turbulent energy dissipation rate	$\mathrm{m^2/s^3}$

Subscripts

0	initial condition
amb	ambient
bu	breakup
evap	evaporation
rel	relative
st	stoichiometric

Acronyms

ABC	Anglo Belgian Cooperation
AHRR	apparent heat release rate
ASOI	after the start of injection
ATDC	after top dead center
BEV	battery electric vehicles
CA	crank angle
CFD	computational fluid dynamics
CI	compression-ignition
DBI	diffused backlight illumination
DI	direct-injection
DNS	Direct Numerical Simulation
DOC	diesel oxidation catalyst
DPF	diesel particulate filter
DWI	direct water injection
ECA	emission control area
ECN	Engine Combustion Network
EE	Eulerian-Eulerian
EEDI	energy efficiency design index
EGR	exhaust gas recirculation
EL	Eulerian-Lagrangian
EU	European Union
FCEV	fuel cell electric vehicles
GHG	greenhouse gas
GUCCI	Ghent University Combustion Chamber I
HAM	Humin Air Motor
HD	heavy-duty
HEV	hybrid electric vehicle
ICE	internal combustion engine
IMO	international maritime organization
KH	Kelvin-Helmholtz
LD	light-duty
LED	light-emitting diode
LES	large eddy simulation
LIF	laser-induced fluorescence-particle
LII	laser-induced incandescence
LTC	low-temperature combustion
PAH	poly-aromatic hydrocarbon
PLN	pump-line-nozzle
PLRS	planar laser Rayleigh scatter
PPCI	partially premixed compression ignition

RT	Rayleigh-Taylor
SA	Spray A
SCR	selective catalytic reactor
SD	Spray D
SEEMP	ship energy efficiency management plan
SI	spark-ignition
SOC	start of combustion
SOI	start of injection
TDC	top dead center
UHC	unbruned hydrocarbonds
WFE	water-in-fuel emulsion
ZEV	zero emission vehicle

List of publications

Publications in peer reviewed international journals

1. **Li, H.**, Verschaeren, R., Beji, T., Verhelst, S. (2021). Investigation of evaporating sprays in a medium speed marine engine. *Experimental Thermal and Fluid Science*, 121, 110278.

2. **Li, H.**, Beji, T., Verhelst, S. (2021). Improving the calculation of evaporating sprays for medium-speed marine-engine-like conditions. *Atomization and Sprays*, 31, 8.

Publications in proceedings of international conferences

1. **Li, H.**, Verschaeren, R., Decan, G., Beji, T., Verhelst, S. (2019). Evaluation of breakup models for marine diesel spray simulations. *29th European Conference on Liquid Atomization and Spray Systems, Paris, France*.

Nederlandse samenvatting –Summary in Dutch–

Verbrandingsmotoren zijn mensen van dienst geweest in een breed spectrum van hun dagelijkse leven sinds hun uitvinding aan het einde van de 19e eeuw. In de afgelopen decennia is er echter steeds meer kritiek gekomen op de opwarming van de aarde en de daarmee gepaard gaande luchtvervuiling. Met de ontwikkeling van elektrificatie heeft de verbrandingsmotor, met zijn bijdrage tot de broeikasgassen en schadelijke uitstoot, zijn voorkeurspositie verloren.

Uit gepubliceerde literatuur blijkt dat vervoer over land in de nabije toekomst waarschijnlijk zal worden gekenmerkt door een mix van technologieën bestaande uit volledig elektrische voertuigen, hybride elektrische voertuigen en conventionele voertuigen met verbrandingsmotor, afhankelijk van de specifieke toepassing en kosten. Er zijn echter minder opties voor vervoer over water. Meer dan 90% van het wereldwijde vrachtvervoer wordt uitgevoerd door schepen, die voornamelijk worden aangedreven door dieselmotoren. Om haar visie voor het verminderen van de uitstoot van vervuilende stoffen kracht bij te zetten, heeft de Internationale Maritieme Organisatie dan ook beslist om een strengere emissiewetgeving, en strengere emissievoorschriften en -normen voor motoren in te voeren.

Als bewezen technologie voor de aandrijflijn wordt de verbrandingsmotor de komende jaren brandstof flexibel. Verschillende gasvormige (bijv. waterstof, aardgas) en vloeibare (bijv. methanol) alternatieve brandstoffen, die op groene en duurzame manieren kunnen worden geproduceerd, winnen geleidelijk aan, aan belangstelling vanwege hun propere en koolstofarme verbrandingskarakteristieken. Om het gebruik van deze opkomende alternatieve brandstoffen te initialiseren bij de scheepvaart, blijven motoren met compressieontsteking de meest betrouwbare en efficiëntste bron. Bij compressieontsteking wordt de vloeibare brandstof geïnjecteerd vanuit een hogedrukinjectiesysteem en ondergaat het een reeks processen, zoals verneveling, verdamping, brandstof-damp/luchtmenging voordat de ontsteking of verbranding plaatsvindt. Het is algemeen bekend dat de verstuiving en de prestaties van het injectiesysteem rechtstreeks van invloed zijn op de verbrandingsefficiëntie van de motor, het brandstofverbruik en de uitstoot van vervuilende stoffen.

Optimalisatie van de brandstofinjectie, de vorming van de verstuiving en het daaropvolgende verbrandingsproces wordt daarom ook gezien als een van de meest effectieve middelen voor dieselmotoren om te voldoen aan de emissienormen zonder verlies aan motorprestaties. Er is uitgebreid onderzoek gedaan naar dieselsprays voor de auto- en vrachtwagenmotoren die worden gebruikt voor vervoer over land. Vanwege de hoge technische vereisten en kosten is onderzoek van verstuiving gericht op middelhoge viertaktmotoren echter nog steeds zeldzaam. Gebaseerd op de eerdere experimentele studies in de 'Ghent University Combustion Chamber I' ofwel GUCCI opstelling, richt dit doctoraat zich op het modelleren van vernevelende verstuiving onder motorachtige condities.

Computational fluid dynamics (CFD)-simulatie is een essentieel hulpmiddel geweest voor het ontwerp en de optimalisatie van motoren. In dit werk werd de OpenFOAM-code gebruikt om het verstuiving-proces in dieselmotoren te bestuderen op basis van de Reynolds-gemiddelde Navier-Stokes-methode. Deze code werd eerst gevalideerd met behulp van de zeer betrouwbare verstuiving-gegevens van het Engine Combustion Network (ECN). Een bevredigende overeenstemming met de ECN-gegevens toonde aan dat de simulatie de verstuiving-processen correct kan vastleggen. Er werd echter een discrepantie gevonden bij het simuleren van de scheepsmotor verstuiving gemeten in de GUCCI-opstelling. Na een samenvatting en analyse van de waarden van de turbulentiemodelconstante gebruikt uit gepubliceerde literatuur (C_1 van het standaard $k-\varepsilon$ model), werd een lagere waarde voor C_1 aangenomen, en een goede overeenstemming onder een breed spectrum aan omgevingsfactoren bereikt (dichtheid variërend van 7.6 tot 22.5 kg/m^3, en temperatuur varirend van 700 tot 950 K). Ook de onenigheid die werd opgemerkt in de vloeistofpenetratie voor een geval bij lage temperaturen, kon worden verklaard door het fenomeen van losraken van de ligamenten dat door de simulatie werd vastgelegd.

Vanwege de eenvoud en wijdverspreide acceptatie in motorsimulatiecodes, zijn ook empirische correlaties van verstuiving, die worden gebruikt om de penetratie van de verstuiving tip te voorspellen, van belang voor dit werk. Twee klassieke penetratiemodellen (zijnde het model van Dent en het model van Arai) werden gebruikt om de penetratieresultaten van de experimentele ECN gegevens te voorspellen vooraleer ze werden gebruikt voor de scheepsmotor verstuiving verkregen in de GUCCI-opstelling. Gezien de transiënte eigenschappen van het PLN injectiesysteem in de doelmotoren, werd een tijdsafhankelijk injectiedrukprofiel voorgesteld voor de berekening van de verstuiving penetratie. De penetratie van de verstuiving tip op grote afstand onder omstandigheden met een lage dichtheid (7.6 en 15.2 kg/m^3) zou naar verwachting evenredig zijn met $t^{2/3}$, wat wordt ondersteund door eerder theoretisch onderzoek. Het klassieke model van de $t^{1/2}$ wet is nog steeds geldig onder omstandigheden van hoge dichtheid (22.5 kg/m^3).

Dit werk vergelijkt het verschil tussen diesel verstuiving voor motoren voor vervoer over land en motoren voor vervoer over water met nadruk op de manier van modelleren. De conclusies die uit dit werk worden getrokken, leggen een basis voor toekomstig onderzoek naar verstuiving voor scheepsmotoren.

English summary

Internal combustion engines (ICEs) have served human beings in a broad scope of our daily life since their invention in the late 19th century. In recent decades, global warming and air pollution have drawn increasing criticism. With the development of electrification, the internal combustion engine, as a contributor to greenhouse gases and noxious emissions, is not favored by many people.

From published literature, in the foreseeable future, land transportation is likely going to be characterized by a mix of solutions in battery electric vehicles, hybrid electric vehicles, and ICE vehicles, according to the specific application and cost. However, there are less options for marine transportation. In fact, more than 90% of global cargo transportation is carried out by ships, which are mainly powered by diesel engines. To confirm its commitment to reduce pollutant emissions, the International Maritime Organization introduced stringent emission legislation, regulations and standards for engine emissions.

As a tried and tested tool for the powertrain, the internal combustion engine is also becoming fuel-flexible in recent years. Different gaseous (e.g., hydrogen, natural gas) and liquid (e.g., methanol) alternative fuels, which can be produced in green and sustainable ways, are gaining gradual interest due to their clean and low-carbon combustion characteristics. Compression ignition remains the reliable and efficient way for marine engines to initialize the combustion for traditional and emerging alternative fuels. In compression ignition engines, the liquid fuel is injected from the high-pressure injection system and undergoes a series of processes, such as atomization, evaporation, fuel-vapor/air mixing before the ignition or combustion occurs. It is widely acknowledged that the spray or the performance of the injection system directly affects engine combustion efficiency, fuel consumption, and pollutant emissions.

Optimization of the fuel injection, spray formation and the subsequent combustion process is seen as one of the most effective means for diesel engines to meet emission regulations without a loss in engine performance. Extensive research on diesel sprays has been performed for the automotive and truck engines used for land transportation. However, due to high technical requirements and expense, spray research targeting medium speed four-stroke engines is still rare. Based on the previous experimental studies in the Ghent University Combustion Chamber

I (GUCCI) setup, this Ph.D. focuses on the modeling work of evaporating sprays under engine-like conditions.

Computational fluid dynamics (CFD) simulation has been an essential tool for engine design and optimization. In this work, the OpenFOAM code was employed to study the spray process in diesel engines based on the Reynolds-averaged Navier-Stokes method. This code was first validated using the highly reliable spray data provided by the Engine Combustion Network (ECN). A satisfactory agreement with the ECN data demonstrated that the simulation can correctly capture the spray processes. However, a discrepancy was found when simulating the marine engine sprays measured in the GUCCI setup. After summarizing and analyzing the values of the turbulence model constant (C_1 of the standard $k-\varepsilon$ model) used from published literature, a lower value of C_1 was adopted, and good agreement under a wide range of ambient conditions (density varying from 7.6 to 22.5 $\mathrm{kg/m^3}$, and temperature varying from 700 to 950 K) was achieved. Also, the disagreement that was noted for the liquid penetration for a low-temperature case could be explained by the ligament detachment phenomenon which was captured by the simulation.

Due to its simplicity and widespread adoption in engine simulation codes, empirical spray penetration models or spray correlations, used to predict the spray tip penetration, are also an interest of this work. Two classical empirical penetration models (i.e., Dent's model and Arai's model) were utilized to predict the penetration results of the ECN experimental data before using them for the marine engine sprays obtained in the GUCCI setup. Considering the transient characteristics of the pump-line-nozzle injection system in the target engines, a time-dependent injection pressure profile is suggested for the calculation of spray penetration. The spray tip penetration at a large distance under low density (7.6 and 15.2 $\mathrm{kg/m^3}$) conditions was expected to be proportional to $t^{2/3}$, which is supported by a previous theoretical investigation. The classical model of $t^{1/2}$ law, is still valid under high density (22.5 $\mathrm{kg/m^3}$) conditions.

This work compares the difference between diesel sprays for land transportation engines and marine transportation engines in terms of modeling approaches. The conclusions drawn from this work lay a foundation for future research on marine engine sprays.

1 Introduction

1.1 Research background

Internal combustion engines (ICEs) date back to 1876 when Otto invented the spark-ignition (SI) engine and 1892 when Diesel developed the compression-ignition (CI) engine. After more than a century, the number of ICEs in use worldwide is about two billion [1]. These ICEs, mostly operating on fossil fuels, propel many vehicles, generate electricity, and provide mechanical power in a broad scope of our daily applications.

It can be seen from Figure 1.1 that fossil fuel oil is still the largest energy supply, and its leading position has been kept for many years, even though its share has started to drop in the past 20 years. About 70% of the oil is consumed in ICEs. They produce a vast amount (e.g., about 5 billion tons [2] in 2016) of the world's greenhouse gases (GHG), which causes global warming and climate change.

In recent decades, global warming (as shown in Figure 1.2) has drawn increasing attention. Human emissions of carbon dioxide (CO_2) and other GHGs are a primary driver of climate change and present one of the world's most pressing challenges [4]. Global temperature increases exceeding 2 ^{o}C above pre-industrial levels are likely to result in severe global consequences [5]. Additionally,

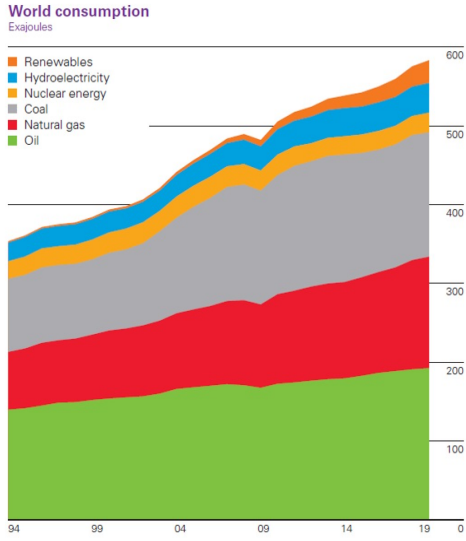

(a) The unit for the Y-axis (energy consumption) is exajoules (1×10^{18} joules).

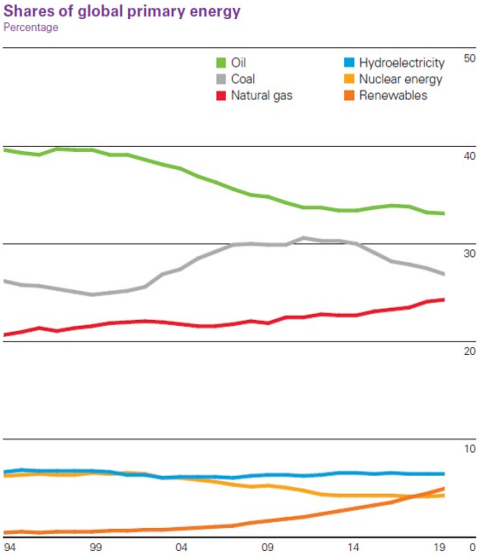

(b) The unit for the Y-axis (share) is percentage.

Figure 1.1: Evolution of global energy consumption and shares of primary energy over time (from 1994 to 2019) [3]. The horizontal axis represents the year for both subfigures.

epidemiologic research also reported that combustion-generated emissions from ICEs have undesirable effects on human health [6].

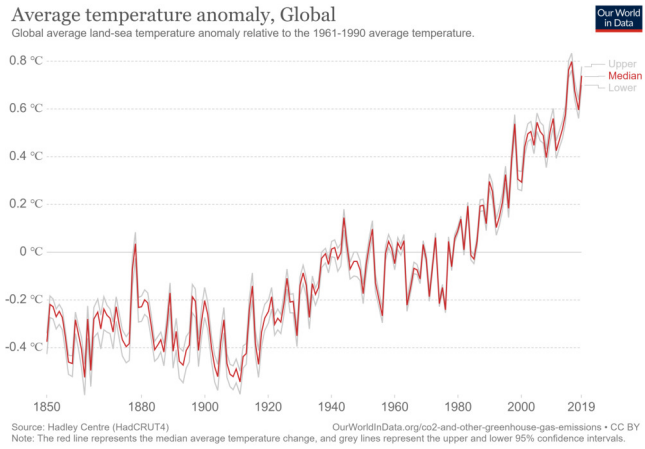

Figure 1.2: Global temperature variation since pre-industrial times [7]

In contrast, battery electric vehicles (BEVs) produce no pollutants such as particulates, nitrogen oxides (NO_x), carbon monoxide (CO), and unburned hydrocarbons (UHC) at the tailpipe. Recent years have seen the development of electrification. An increasing number of people have thoughts that the ICEs should be replaced by electricity-driven motors and that the end of the ICE is in sight [8].

For example, the Zero Emission Vehicle (ZEV) Network, proposed by the C40[1] group, is currently pursuing zero-emission vehicle technologies to reduce transport emissions by eliminating ICE vehicles from inner cities and using renewable energies (e.g., solar and wind) as a primary energy source. To reach the objective of climate neutrality by 2050, the European Union (EU) presented the Fit for 55 package, which is a set of proposals to revise and update EU legislation for GHG emission, on 14 July 2021. The Connecting Europe Facility will deploy new funding to support decarbonization of the transport sector.

In order to achieve the goal of GHG emissions reduction, we must first figure out where the emissions come from.

It is clear from Figure 1.3 that the largest GHG emission is not from the transport sector. As shown in the figure, the GHG emissions contribution by the transport sector is 16.2% in 2016, which includes a small amount of electricity as well

[1] C40 is a network of the world's megacities committed to addressing global warming and climate change. Its member cities include 96 of the world's largest and most influential cities, representing 700+ million citizens and 1/4 of the worldwide economy.

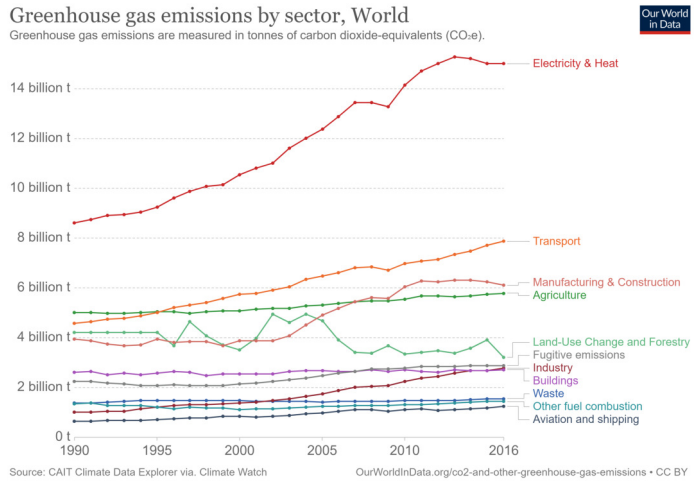

(a) GHG emissions by sector from 1990 to 2016

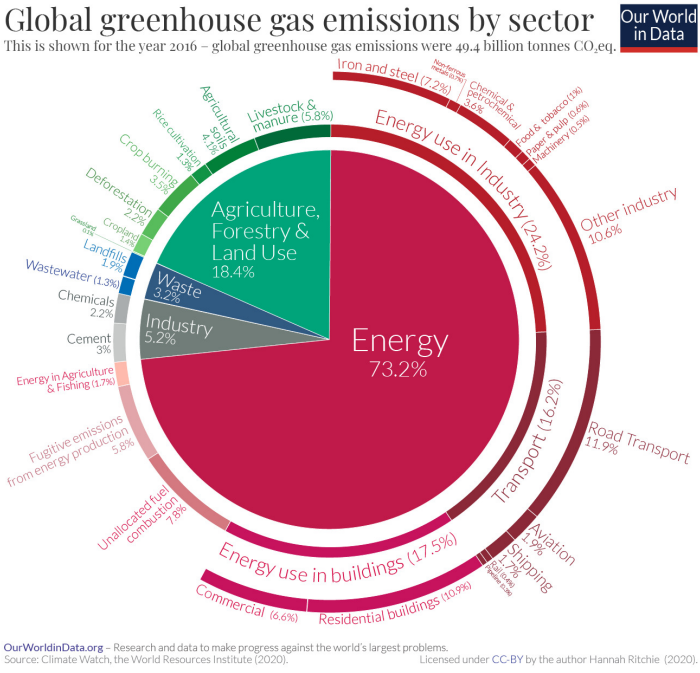

(b) Pie chart of GHG emissions by sector for the year 2016

Figure 1.3: GHG emissions by sector

as a direct emission from ICEs burning fossil fuels. This data has historically remained at this level [2]. This also means that if the whole transport sector could be electrified and powered in a decarbonized way, the global GHG emission would be reduced by about 10%. Of course, this scenario is totally idealized, at least for the foreseeable future.

The 'clean' energy, such as renewables, for example, hydroelectricity, only supplies a small fraction of current energy needs. Another obstacle to overcome is the stable energy supply or energy storage. For example, when there is no wind blowing or no sun shining.

Based on a life-cycle analysis [9–11], which accounts for all the effects on CO_2 during the entire vehicle's lifetime [12], the CO_2 difference between the conventional ICE vehicles and BEVs is limited.

The global transportation infrastructure nowadays is largely based on the ICEs burning liquid fuels. Widespread adoption of BEVs requires a tremendous investment in charging infrastructure and electricity generation, which may also need decades.

There are some bottlenecks for battery technology to overcome.

- The toxicity caused during the production process of battery metals [13].
- Fast charging rates increase the fire risk and reduce the battery life [14].
- The complicated recycling for the Li-ion battery and battery packs [15, 16].

The energy density limitations and cost for current technology limit the use of electrification essentially to small passenger cars or light-duty vehicles (LDVs) for land transport.

1.2 Land and Marine transportation

Future land transportation is likely going to be characterized by a mix of solutions involving BEVs, hybrid electric vehicles (HEVs), fuel cell electric vehicles (FCEVs), and ICEVs, according to the specific application and cost [2].

Replacement of ICEs in heavy-duty (HD) applications seems technically feasible but not practical [2, 17] in terms of power requirement and charging time, not to mention in the marine sector, as explained in the following example.

Consider a large container ship, which carries 17 million liters of fuel, i.e., around 170 million kWh of fuel energy. Here are two questions: 1) what is the weight of a battery pack that holds half[2] the energy of the fuel energy; 2) how long does it need to charge, for instance, even at an improbable charging rate of 100 MW (the Supercharger of Tesla works at 0.25 MW). The calculations[3] below give the answers.

$$\text{Battery pack weight: } \frac{\text{Energy}}{\text{Energy density of battery}} = \frac{85\times10^6}{0.4}\frac{\text{kWh}}{\text{kWh/kg}} = 212.5\times10^6 \text{ kg} = 2.125\times10^5 \text{ Ton}$$

$$\text{Charge time: } \frac{\text{Energy}}{\text{Charging rate}} = \frac{85\times10^6}{100}\frac{\text{kWh}}{\text{MW}} = 850 \text{ h} = 35.4 \text{ days}$$

This is clearly not desirable. In fact, more than 90% of global cargo transportation is carried out by ships, which are mainly powered by diesel engines.

Due to its large cargo loading, economic advantage and long-distance transportation, waterway transportation is the main transportation mode for today's international trade among many cargo transportation methods. Diesel engines are widely used in transportation as the primary equipment for power generation due to their high thermal efficiency and reliability.

The International Maritime Organization (IMO), a specialized agency of the United Nations, is the global standard-setting authority for international shipping's

[2] It is assumed that the electric drive motor is twice as efficient as an internal combustion engine based on the research performed by Gustafsson et al. [18].

[3] The battery pack energy density is assumed to be 0.4kWh/kg. This value is a threshold that Tesla claimed may be achieved in five years.

safety, security, and environmental performance. The International Convention for the Prevention of Pollution from Ships, also known as MARPOL, is the main international convention covering pollution prevention of the marine environment by ships from operational and accidental causes.

According to the Third IMO GHG study [19], total shipping emissions were approximately 938 million tons CO_2 and 961 million tons CO_2e (GHG combining CO_2, CH_4, and N_2O) for 2012. Moreover, maritime GHG emissions are projected to increase significantly in the coming decades. An increase ranging from 50% to 250% in the period to 2050 is estimated depending on future economy and energy development.

Therefore, further action should be performed to mitigate the emissions' growth. To achieve the goal of GHG emissions reduction, a chapter was adopted in MARPOL Annex VI to ensure an energy efficiency standard for ships:

- The Energy Efficiency Design Index (EEDI), which aims at promoting the use for more energy-efficient and less polluting equipment and engines, is the most important technical measure for new ships.
- The Ship Energy Efficiency Management Plan (SEEMP), establishing a mechanism to improve energy efficiency, is an operational measure for new and existing ships.

To confirm its commitment to reduce GHG emissions from international shipping, IMO adopted an initial strategy representing a framework for further action in 2018. This strategy includes candidate short-, mid-, and long-term measures, such as further improvement of the EEDI and the SEEMP, enhanced technical cooperation, research and development, effective uptake of alternative low-carbon and zero-carbon fuels, innovative emission reduction mechanism, etc.

The "1997 Protocol" (Tier I) to MARPOL, which includes Annex VI, set limits on SO_x and NO_x emissions from ship exhaust (shown in Figure 1.4) and prohibited deliberate emissions of ozone-depleting substances. In 2008, Annex VI amendments (Tier III) were adopted, which introduced more stringent regulations on SO_x and NO_x emissions. Furthermore, designated Emission Control Areas (ECAs)[4] set stricter standards.

To keep up with these standards and regulations, further development and optimization of important engine components is necessary for diesel engine

[4] The four ECAs are: the Baltic Sea area; the North Sea area; the North American area (covering designated coastal areas off the United States and Canada); and the United States Caribbean Sea area (around Puerto Rico and the United States Virgin Islands).

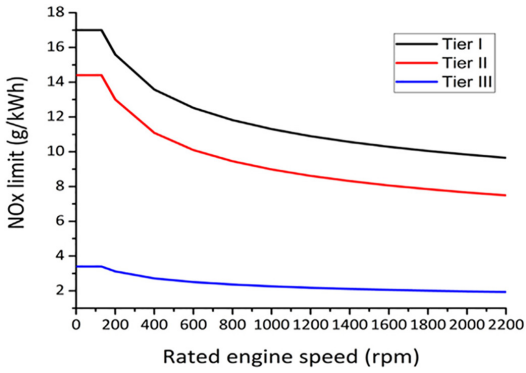

(a) NO_x emission limits

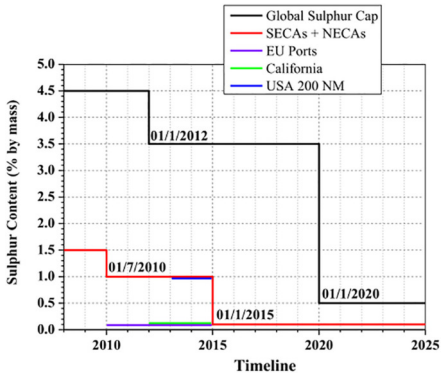

(b) Sulfur limits on fuel. The SO_x in diesel engine exhaust is mainly from the combustion of sulfur contained in the fuel. Therefore, Annex VI regulations include caps on the sulfur content of fuel oil to control SO_x emissions.

Figure 1.4: MARPOL limits on NO_x and fuel sulfur content [20].

designers and manufacturers. The exhaust emission at the ICE tailpipe equals the production in the cylinder during the combustion process minus the reduction by the engine after-treatment systems. This can be expressed in the equation below, which also hints at several directions for the reduction of GHG and pollutant emissions from ICEs. The next section will introduce recent emission reduction technologies for marine diesel engines.

$$\text{Exhaust (tailpipe)} = \text{Production (in-cylinder)} - \text{Abatement (after-treatment)} \quad (1.1)$$

1.3 Recent developments for marine engines

Figure 1.5 is a schematic illustrating the technologies used in marine engines to reduce emissions. The left column represents the 'Production' in Eq. (1.1), while the middle column is the second item, 'Abatement'. The effect of ship operations is not considered in this work. The corresponding content can be found in the paper by Perera et al. [21].

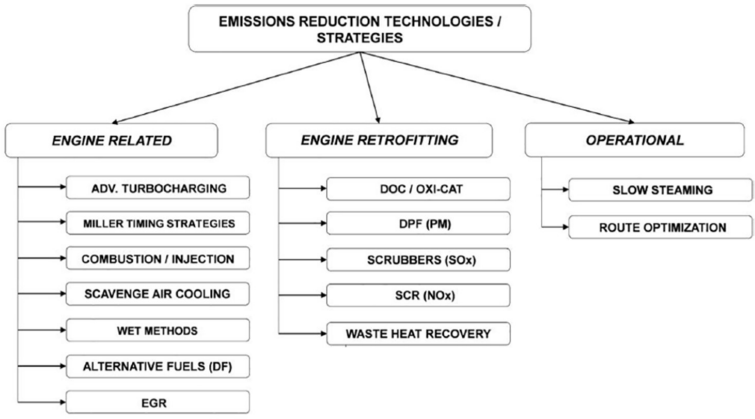

Figure 1.5: Emission reduction technologies for marine engines [22].

Turbocharging, which is used in most medium and low speed marine engines [22], is a mature technology. In order to increase the engine boost pressure, the enthalpy of the exhaust gas is used to drive a turbine connected to a compressor, thus raising the volumetric and mechanical efficiency and reducing fuel consumption.

Miller timing [23], or the Miller cycle, has drawn much attention from engine researchers due to its potential to control NO_x formation in the cylinder [24]. The NO_x emission reduction by Miller timing is through the change of the valve timing to make the effective expansion process longer than the compression process. Then the in-cylinder temperature and pressure are dropped at the end of the compression.

Wet technologies reduce NO_x formation through the introduction of water in the combustion chamber [25]. The water increases in-cylinder mixture heat capacity, thus reduces the peak pressure and temperature of the combustion process. The wet technologies mainly include Humid Air Motor (HAM), Direct Water Injection (DWI), and Water-in-Fuel Emulsion (WFE).

Similar to wet technologies, Exhaust Gas Recirculation (EGR) also increases the charge mixture's heat capacity due to the CO_2 and H_2O in the EGR. Therefore,

the NO_x formation is reduced due to the decreased peak combustion temperatures. EGR technology, which has a high NO_x reduction potential, is commonly used in automotive diesel engines. Its application to marine engines is far from straightforward, mostly because of the properties of marine diesel fuel (e.g., high sulfur level[5]).

Installing a Selective Catalytic Reactor (SCR) in the engine exhaust line can satisfy the IMO Tier III standard [20]. After the catalytic reactions with ammonia (urea), NO_x in the exhaust is converted to nitrogen and water. SCR technology has been recognized as a standard and mature method and is the only technology approved by the IMO for NO_x emissions reduction. In an exhaust after-treatment system, the diesel oxidation catalyst (DOC) and diesel particulate filter (DPF) are installed upstream of the SCR. The function of the DOC is to oxidize most of the NO in the exhaust to NO_2, and the DPF is used to collect and oxidize soot particles (partly with NO_2).

An exhaust gas scrubber, which can remove the majority of SO_x emissions, is a device to separate pollutants from the waste gas by the realization of close contact between the exhaust gas and a liquid. A recent paper [26] proposed a scrubbing system based on seawater electrolysis technology and found the maximum removal rates of NO_x and SO_2 reached 92% and 100% under optimal conditions.

For modern large diesel engines, about 50% of the fuel energy is utilized for useful shaft power, while the remainder is lost to the environment as waste heat. Effective utilization of this wasted energy can improve efficiency and reduce emissions. Many waste heat recovery systems [22] have been designed for utilization on ships.

In diesel engines, the liquid fuel is injected from the high-pressure injection system and undergoes a series of processes, such as atomization, evaporation, fuel-vapor/air mixing before the ignition or combustion occurs. That is, the fuel spray provides boundary conditions for the diesel combustion and subsequent events like NO_x and soot formation. It is widely acknowledged that the spray or the performance of the injection system directly affects diesel engine combustion efficiency, fuel consumption, and pollutant emissions. Many parameters such as in-cylinder temperature and density, injector nozzle size, injection pressure, fuel properties, injection duration, and injection timing influence the temporal and/or spatial distribution of the fuel-air mixture in the chamber, thus affecting the combustion reactions.

The use of alternative fuels (e.g., hydrogen, natural gas, methanol, ammonia, etc.) produced in a sustainable and green way can also help decarbonize marine

[5] The sulfur content in land vehicle diesel is much lower. For example, the limited sulfur content for the Euro VI standard is 10 parts per million.

transportation [27]. Recently, the dual-fuel combustion concept is gaining interest as an economic way to meet the upcoming standards and reduce GHG emissions [12]. The power of dual-fuel engines is mainly from the combustion of alternative fuels, often initialized by a pilot spray. For example, for methanol there are two types of methanol/diesel dual-fuel concept: (1) methanol is directly injected into the combustion chamber, and (2) methanol is injected in the intake manifold (fumigation concept). According to the analysis of Dierickx et al. [28, 29], the fumigation concept is an easy and cost-effective retrofit solution compared to the other one. This concept is also applicable to dual-fuel engines operating on other alternative fuels mentioned above [30–33]. In this fumigation mode, most of the thermal energy is provided by the burning of alternative fuels with a high hydrogen-to-carbon ratio. Thus, the fumigation dual-fuel concept is the main interest of discussion here. Typically, the base diesel engine is kept as is and the alternative fuel (e.g., natural gas, ammonia, methanol, etc.) is premixed with the intake air. As these alternative fuels have high octane number (high autoignition temperature), a small amount of diesel (also known as a pilot spray) is used as an ignition source. This type of combustion process is illustrated in Figure 1.6. In these dual-fuel engines, the characteristics of the pilot spray are also important for the engine operation and exhaust emissions.

For both conventional and dual-fuel diesel engines, the spray process, which involves the turbulent flow, multiphase heat and mass transfer etc., is complex. Despite difficulties and challenges, significant progress has been made by research groups all over the world to provide better insight into this topic, as will be returned to later in Chapter 2.

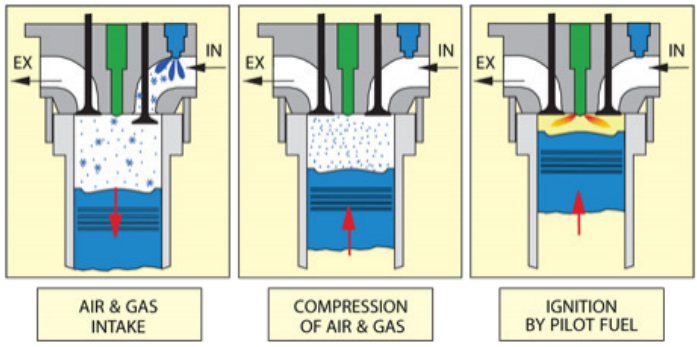

Figure 1.6: Dual-fuel fumigation engine principle. Alternative fuels with high octane number (e.g., natural gas, methanol) are injected in the intake manifold and premixed with intake air. Because this premixed charge is difficult to autoignite, diesel fuel is injected to initialize combustion.

1.4 Goal statement

Thanks to the development of measurement technology and computing capacity, a better understanding of the spray combustion process in diesel engines has been gained. Extensive work has been performed over the past decades. However, these studies typically consider land transportation applications, such as LD engines for passenger cars and HD engines for trucks.

ICEs for marine and industrial use are typically classified by the crankshaft rotational speed [34–36]. The high speed engines have a rotational speed of 1400 revolutions per minute (rpm) and higher; medium speed engines have a nominal speed range from 400 to 1200 rpm; low speed engines have a nominal speed of less than 400 rpm. Generally, high speed engines are used for land transportation, while medium and low speed engines are used for marine transportation and industrial use [37].

Different from those of car- and trucked-sized engines, marine engines have larger injector nozzles and cylinders. For example, medium speed marine engines typically have a bore size of 240 mm or even larger [38], while HD engines have a bore of about 100 mm or less [39]. The injector nozzle diameter for medium speed marine engines is also three times (or even more) larger than that of the HD engines. This leads to differences in the diameter of the fuel droplets and, thus, the evaporation, mixing, and combustion processes. According to the calculations in published literature [40, 41], some representative dimensionless numbers (e.g., Reynolds number, Weber number, and Ohnesorge numbers) are also higher for marine engines. However, few studies can be found on spray characteristics for the larger marine engines compared to the smaller sized engines due to higher technical requirements and expense. Regarding the spray characteristics and combustion process in low speed two-stroke marine engines, both experimental and numerical studies have been conducted by Winterthur Gas & Diesel [42–45]. However, research targeting medium speed four-stroke marine engines is still rare due to the aforementioned reasons.

In recent years, the Transport Technology group at Ghent University cooperated with Anglo Belgian Corporation (ABC) and built the Ghent University Combustion Chamber I (GUCCI), an optically accessible constant volume combustion chamber aiming at studying the spray characteristics for medium speed marine engines. Over the past years, many experimental studies have been performed in the GUCCI setup. This Ph.D. focuses on the modeling work of evaporating diesel sprays under conditions typical of medium speed marine engines. The goal of the research is to deepen the understanding of the relevant physical processes, which can be used for engine development and simulation.

1.5 Scope and outline

Spray research is vital to marine engine development and optimization. However, there is limited research into the spray process for medium speed marine engines, especially numerical research. Advanced computational fluid dynamics (CFD) simulation which involves detailed modeling of sub-processes, and simplified modeling (empirical penetration model), are the two main research directions of this work because these two directions are also helpful to fundamental research and practical applications. Moreover, comparative studies are performed to seek the modeling difference between heavy-duty engines and marine engines. The following paragraphs give a brief introduction of this work:

Chapter 2 presents a comprehensive review of fuel spray behavior in diesel engines. Several groundbreaking publications are introduced to further explain the importance of the spray and its impact on the subsequent processes, such as evaporation, fuel-air mixing, combustion, and pollutant formation. The experiments used to validate the modeling results are also included in this chapter.

Chapter 3 first describes the CFD modeling process of diesel sprays. Detailed governing equations for the gas phase and liquid phase are established. The CFD results of evaporating sprays for different types of diesel engines are analyzed with respect to several modeling options.

Compared with CFD modeling, spray correlations or empirical spray penetration models are relatively simple and widely used in many engine simulation codes. Aiming at improving the spray correlation modeling for medium speed marine engines, the predictive capability of some classical spray correlations is first evaluated through comparison with experimental measurements in Chapter 4. Some improvements are then considered to achieve better agreement.

Finally, Chapter 5 summarizes the conclusions drawn from this Ph.D. study and gives an outlook for future research.

2

Diesel sprays - a systematic review

As mentioned briefly in Chapter 1, the diesel spray characteristics play a vital role in the combustion efficiency and pollutant formation in diesel engines. In this chapter, section 2.1 gives a detailed discussion on the spray combustion process in direct-injection (DI) diesel engines, with the aid of groundbreaking conceptual models. Through this discussion, fuel injection, atomization, evaporation, mixing, combustion, and pollutant formation processes are linked. The following section 2.2 introduces the experimental data used to validate the spray modeling in this work, i.e., the spray measurements within the Engine Combustion Network (ECN) representing diesel engines for land transportation, and the measurements performed in the Ghent University Combustion Chamber I (GUCCI) that are typical for the medium speed engine conditions. Section 2.3 presents the recent advances in diesel spray CFD simulations.

2.1 Spray combustion in diesel engines

In this section, a detailed description of how spray combustion proceeds in DI diesel engines is presented. Spray combustion in diesel engines is a complex, three-dimensional process that involves turbulence, multiphase physics and chemical reactions, and where the physical processes affect the relevant

chemical processes, e.g., ignition, pollutant formation. The description of spray combustion as an integrated process will give a better insight into the relevant problems.

An accurate conceptual model, or phenomenological description, helps explain the relevant processes, interpret experimental data, and provide guidance for the numerical model development. The conceptual model proposed by Dec [46] in 1997 will be introduced comprehensively in section 2.1.1 because the relevant processes are similar to those in the medium-speed marine engine this work is focusing on. After that, the partially premixed compression ignition (PPCI) low-temperature combustion (LTC) model is presented briefly due to its application on heavy-duty engines operating at low-load conditions.

2.1.1 Conventional diesel combustion conceptual model

With the advent of optically accessible engines and advanced laser diagnostics, much information on spray combustion in diesel engines could be obtained. Dec proposed a conceptual model for conventional diesel combustion[1] based on different optical techniques (listed in Table 2.1). These measurements include liquid-phase penetration, vapor-fuel/air mixture ratio, autoignition, and soot formation.

Table 2.1: Optical techniques used by Dec [46]

	Optical technique
Liquid fuel penetration	Elastic-scatter
Equivalence ratio	Planar laser Rayleigh scatter (PLRS)
Autoignition location	Chemiluminescence
Poly-aromatic hydrocarbon (PAH) concentrations	Planer laser-induced fluorescence (PLIF)
Soot concentration	Laser-induced incandescence (LII)
Soot particle size	Elastic-scatter
Diffusion combustion zone	OH radical PLIF

Figure 2.1 illustrates the optically accessible engine used in the studies of Dec. This was a single-cylinder, direct-injection, 4-stroke diesel engine based on a

[1] "Conventional" means diesel injection starts shortly before top dead center (TDC) when compared with the injection timing of LTC concepts.

Cummins heavy-duty diesel production engine, with a stroke of 152 mm and a bore of 140 mm. An 8-hole nozzle solenoid valve-controlled injector was employed. The hole diameter was 0.194 mm.

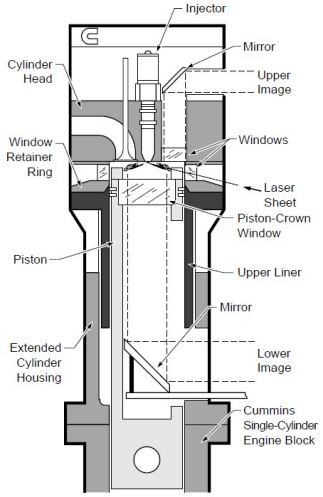

Figure 2.1: Schematic of optically accessible diesel engine use by Dec [46]. Images were taken through both the piston-crown window ("lower image" in the figure) and cylinder-head window ("upper image" in the figure). All the images were taken at an engine speed of 1200 rpm.

Figure 2.2 shows the apparent heat release rate (AHRR), cylinder pressure and injector needle lift profile for the diesel spray combustion process performed by Dec. The fuel injection starts at -11.5^{o} after top dead center (ATDC), which is also defined as 0^{o} after the start of injection (ASOI). As is typical of diesel combustion, a negative dip is first clearly observed from the AHRR curve. Near -7.5^{o} ATDC, the AHRR increases to zero, and then undergoes a rapid rise and fall. From -2.5^{o} ATDC, the AHRR curve goes through a second peak and drops back down more slowly. According to the characteristics of the AHRR curve, the combustion process under conventional diesel conditions can be divided into three phases.

- Ignition delay. The time interval between the start of injection (SOI) and the start of combustion (SOC). For Figure 2.2, the ignition delay is from -11.5^{o} ATDC to -7.5^{o} ATDC. During this period, diesel fuel mainly undergoes a physical process, i.e., the liquid fuel atomizes into smaller droplets, heats up and vaporizes in the hot combustion chamber, as it entrains the hot surrounding air. A fuel-rich vapor fuel/air mixture is formed.

- Premixed combustion. The fuel-rich mixture formed during the preceding period is ignited and burns rapidly. A rapid increase of cylinder pressure is also seen in Figure 2.2. This initial sharp rise and fall is also commonly referred to as the "premixed burn" or the "premixed burn spike".

- Mixing-controlled combustion. The AHRR in this period undergoes a second broader hump, as shown in Figure 2.2. The burning rate at this phase is determined by the fuel/air mixing rate.

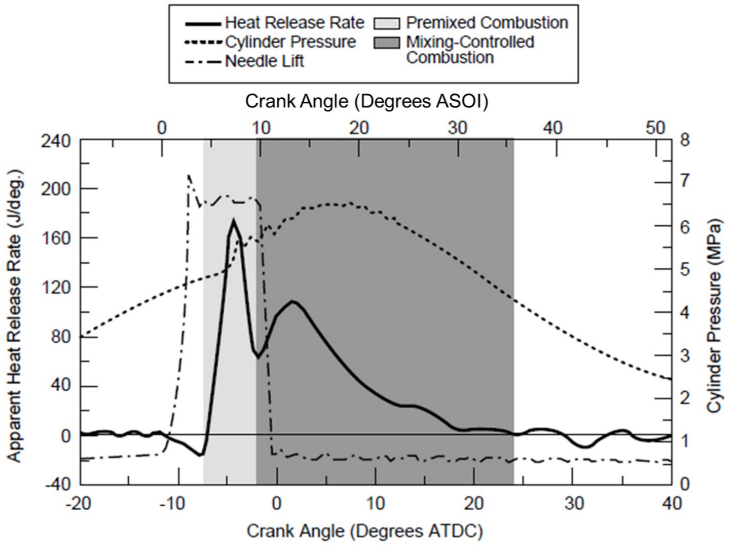

Figure 2.2: Apparent heat release rate, cylinder pressure, and injector needle lift [46]. The engine speed was 1200 rpm, and the data were ensemble-averaged over 20 cycles.

The interpretation of the conceptual model will follow the temporal sequence, using the time unit crank angle[2] ASOI. The composite schematics shown in Figure 2.3 illustrate the idealized cross-section slices through the mid-plane of the jet [46]. It should be noted that wall impingement and air swirl are not considered in this model.

- **Initial Jet Development** (0.0^o - 4.5^o ASOI) - At 1.0^o ASOI, the jet contains only liquid fuel (droplets, ligaments, and/or an intact liquid core) labeled dark brown. From 2.0^o ASOI, a vapor-fuel region starts to develop as the liquid fuel heats up and vaporizes by the entrainment of the ambient hot

[2] For the engine speed of 1200 rpm, 1.0^o crank angle (CA) = 139μs.

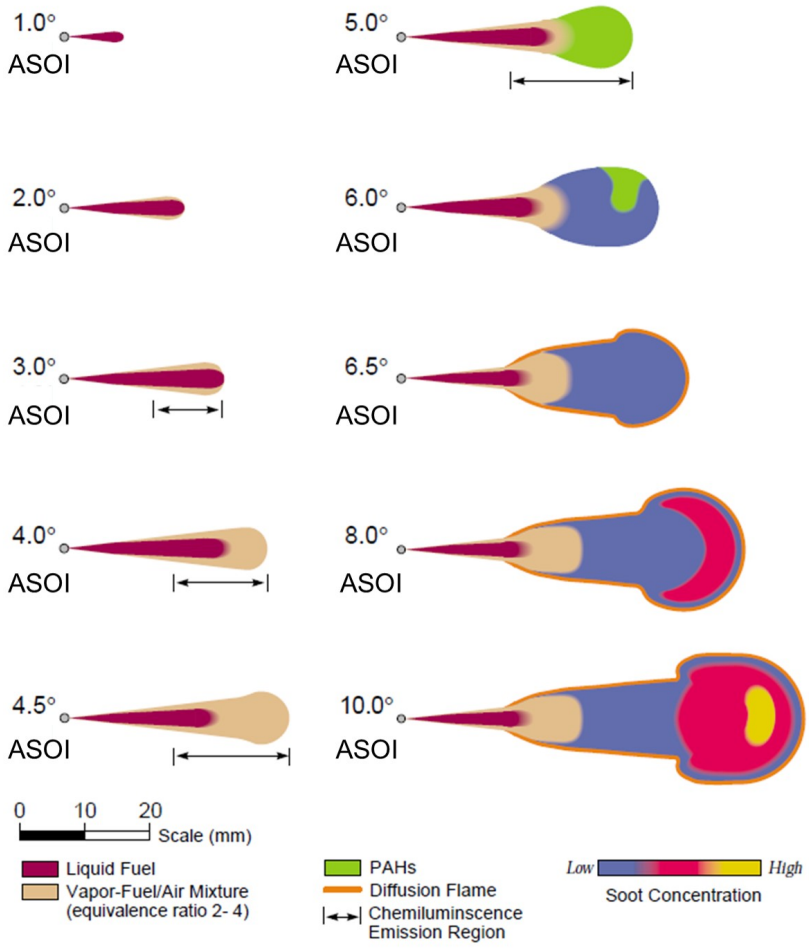

Figure 2.3: Schematics showing the evolution of DI diesel combustion from the start of injection till the mixing-controlled combustion phase [46]. It is noted that the soot distribution in the 6.0^o ASOI schematic is not symmetric. This is because the measurement showed that soot occurs throughout large (not the entire) portions of the cross-section with the locations varying from cycle to cycle, as explained by Dec. The crank angle degree ASOI is given at the side of each schematic

air. The vapor region first appears on the sides of the liquid region and grows thicker as the jet penetrates further into the combustion chamber. By 3.0^o ASOI, the liquid fuel reaches a maximum and fairly constant distance (about 23 mm, for Dec's experiment). The maximum liquid penetration, termed "liquid length", is where the hot entrained ambient air vaporizes all

the liquid fuel. After the liquid fuel is vaporized completely, momentum carries the vapor fuel to penetrate and entrain more hot ambient gases. By 4.5^{o} ASOI, a head vortex is formed at the jet's leading portion, as is typical of gas jets. At the same time, a fuel-rich and relatively uniform fuel/air mixture is formed in the downstream region. According to the measurement by PLRS (see Table 2.1), the equivalence ratios range from about 2 to 4.

- **Autoignition** (3.0^{o} - 5.0^{o} ASOI) - As shown in Table 2.1, chemiluminescence imaging was utilized to examine autoignition. The chemiluminescence images show that the flame emission is first detected as early as 3.0^{o} ASOI. At this time, the vapor penetration is barely longer than the liquid. The chemiluminescent region, indicated by the double-ended arrows in the schematics, is mainly from the vapor region on the jet side. While from 4.0^{o} to 5.0^{o} ASOI, most of the chemiluminescence is emitted from the leading vapor portion. A distinct difference that can be seen in the 5.0^{o} ASOI schematic is that the PAH (labeled with the green color), i.e. the soot precursors species, is formed in the leading portion. The chemiluminescence at 5.0^{o} ASI is about twice as bright as that of 4.5^{o} ASI. This sudden large increase in image intensity is due to the fuel breakdown and PAH formation.

- **First Part of Premixed Burn Spike** (4.0^{o} - 6.5^{o} ASOI) - The chemiluminescence images at 6.0^{o} ASOI are much more intense in the leading region of the jet, with the brightest areas about 1000 times brighter than that at 5.0^{o} ASOI, suggesting that soot luminosity is dominating in this region. As illustrated in the 6.0^{o} ASOI schematic, the PAHs formed in the leading portion of the jet at 5.0^{o} ASOI are consumed, and soot is formed in the same region. Soot images verify this because the LII and elastic-scattering imaging cannot detect soot before 6.0^{o} ASOI. By 6.5^{o} ASOI, small soot particles are distributed throughout the leading region. The LII images at 6.5^{o} ASOI show a strong signal in the leading portion. In contrast, the corresponding elastic-scatter images detect a weak signal in the center of this region and a relatively high signal around the jet periphery. This indicates that small soot particles form in the center, and relatively large soot particles exist at the jet periphery. Note that the AHRR curve (Figure 2.2) starts to head up at 4.0^{o} ASOI and undergoes a rapid rise after 4.5^{o} ASOI. As discussed earlier, the fuel breakdown and PAH formation occur at 5.0^{o} ASOI, which coincides with the sharp increase of the AHRR curve. This suggests that the rapid rise of the AHRR is caused by the premixed combustion of the fuel-rich mixture that forms in the preceding processes.

- **Onset of the Diffusion Flame** (5.5^{o} - 6.5^{o} ASOI) - In the 6.5^{o} ASOI schematic, a thin layer that encircles the downstream portion of the jet can be

observed, and this thin layer extends back toward the nozzle exit to a certain location just upstream of the liquid length. The distance between nozzle exit and the upstream most extent of combustion in the fuel jet is defined as the "lift-off length" [47]. As indicated by the OH-PLIF images, this thin layer consists of the OH radicals produced by the diffusion combustion[3]. As discussed previously, the soot images show that the soot particles at the jet periphery are larger than those at the center region. This is because the surrounding diffusion flame creates a hot oxygen-depleted region that promotes the formation and agglomeration of soot particles. At the same time, the liquid length becomes shorter as the heat released by diffusion combustion increases the temperature.

- **Last Part of Premixed Burn Spike** (7.0^o - 9.0^o ASOI) - After 6.5^o ASOI, the jet continues to penetrate further downstream the combustion chamber. The main difference occurs in terms of soot concentration and soot particle size distribution. The LII images show that the soot concentrations increase progressively, and after 7.5^o ASOI, soot concentrations at the leading portion are generally higher than those upstream. But soot concentration has a relatively uniform distribution at any axial position, i.e., the concentration in the center is almost the same as that at the edge. As depicted in the 8.0^o ASOI schematic, a high soot concentration region is formed in the head-vortex region at the tip. The elastic-scatter images show that large soot particles are produced by the diffusion flame cluster at the jet periphery, but a small part of them travel inward due to the turbulent mixing.

- **First Part of the Mixing-Controlled Burn** (9.0^o ASOI to end of injection) - It can be seen from Figure 2.2 that the AHRR curve starts to increase after the first spike, which suggests that the premixed fuel is burning out, and the combustion in the next phase will be controlled by mixing. Compared with the schematic at 8.0^o ASOI, the jet appearance only has a slight difference. Besides the longer penetration, the soot concentration becomes even higher throughout the head vortex, as depicted in the 10.0^o ASOI schematic. The elastic-scatter measurement also shows that the soot particle size in this region is larger.

Before the end of injection, the diesel fuel jet enters a quasi-steady (or "developed") stage, i.e., the mixing-controlled combustion phase, as shown in Figure 2.4. This schematic of mixing-controlled combustion has a similar overall

[3] The OH radical does not exist in the fuel-rich (equivalence ratio from 2 to 4) premixed combustion. Under typical diesel combustion conditions, high OH radical concentrations are the diffusion combustion products near stoichiometry. Thus, the diffusion flame zone is marked by the OH PLIF signal [48].

appearance with the 10.0° ASOI schematic in Figure 2.3. But the jet penetration is somewhat longer, the soot concentration is higher, and the soot particle size is larger in the head vortex. Considering the turbulent nature of the diesel jet, a ragged edge is drawn in the jet boundaries.

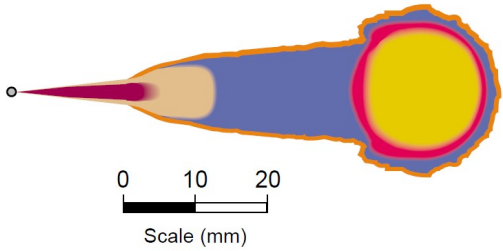

Figure 2.4: A schematic illustrating the mixing-controlled combustion [46]. This figure shares the same color coding with Figure 2.3.

Flynn et al. [49] extended Dec's model by combining the optical data with chemical kinetics analyses. Due to the similar combustion characteristics and cetane number with diesel fuel, n-heptane was chosen as a surrogate fuel. The kinetics simulation was performed using a detailed oxidation mechanism (550 species and 2454 reactions) of n-heptane.

Figure 2.5 shows an integrated mixing-controlled combustion model incorporating physical and chemical features. After the cold fuel is injected into the combustion chamber, the hot air is entrained, which heats and vaporizes the liquid fuel within a few milliseconds, creating a vapor-fuel/air region with temperatures of approximately 825 K. At about 750 K, low-temperature oxidation reactions occur, and diesel fuel starts to break down. The vapor-fuel/air mixture's temperature increases as the ambient air continues to be entrained and chemical reactions release heat. When the temperature reaches 825 K, the rapid oxidation mechanism starts and consumes all available oxygen in this region, raising the temperature to about 1600 K. These rapid oxidation reactions also produce an amount of C4 compounds, C_2H_2, C_2H_4, C_3H_3, which are generally thought to be elemental building blocks of PAH. A fuel-rich premixed flame (labeled light blue color) with an equivalence ratio of 3 to 5 is assumed to exist downstream the vapor-fuel/air region (equivalence ratio of 2 to 4). This would create an ideal environment for soot formation, considering the low oxygen concentration mentioned above. Therefore, the initial soot formation (grey color in Figure 2.5) is believed to occur just downstream of this fuel-rich premixed flame. The soot particles and fuel fragments are transported toward the head vortex and outward jet periphery. The diffusion flame temperature at the jet periphery is very high (about 2700 K) because the combustion is almost stoichiometric. Soot oxidization (indicated by

the dashed white line) occurs at this high temperature. Additionally, the production rates of thermal NO (shown in green color) are also expected to be promoted in this high-temperature edge.[4]

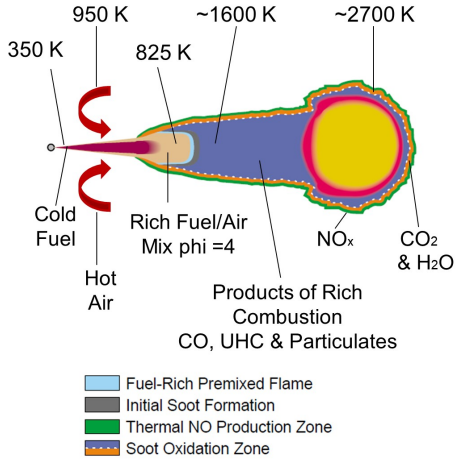

Figure 2.5: An integrated view of mixing-controlled combustion of a diesel spray [49].

2.1.2 Partially premixed compression ignition conceptual model

As discussed previously, thermal NO_x is the primary contributor to a diesel engine's NO_x emission, and its production rates increase exponentially with in-cylinder temperature [52]. Therefore, low-temperature combustion (LTC) strategies have been proposed. To reduce the in-cylinder temperatures, high levels of EGR are used to dilute the in-cylinder mixtures. At the same time, the in-cylinder oxygen concentration also reduces, thus decreasing the relevant oxidation reaction rates. However, the combustion efficiency drops at high EGR levels, and CO and UHC emissions increase.

Recently, the "partially premixed compression ignition" (PPCI) strategies have become attractive due to their lower emissions in terms of NO_x and PM. In addition to the utilization of high dilution by EGR, a short injection duration is also employed to achieve a longer ignition delay. Thus, the PPCI LTC strategies are typically most easily applied for low-load operating conditions.

[4] There are three mechanisms for NO formation: thermal, prompt and nitrous oxide. The thermal mechanism based on Zeldovich's theory [50] is thought to be the dominant one under diesel engine conditions. More information about the NOx formation can be found in Refs. [1, 51].

Figure 2.6 presents a comparison of the conventional diesel combustion conceptual model as explained above, and the PPCI conceptual model by Musculus et al. [52].

For the initial stage (e.g., before 3.0^o ASOI in Figure 2.6), there is no obvious difference between conventional and PPCI conditions regarding the penetration behavior. For early-injection PPCI conditions, the penetration is somewhat longer because the in-cylinder temperature and in-cylinder density are lower. For late-injection LTC conditions, the in-cylinder conditions are similar to conventional diesel conditions due to the injection being close to TDC.

For PPCI conditions, shortly after the quasi-steady liquid length is reached, the injection ends. An entrainment wave is created during the ramp-down of the injection process. As shown in the 5.0^o ASOI schematic, the entrainment wave head is at the nozzle exit. Afterward, it moves downstream and passes through the liquid length at 7.0^o ASOI. Within 1.0^o CA, the liquid fuel is completely vaporized, as illustrated in the 8.0^o ASOI schematic. Research [53] shows that the entrainment wave under PPCI conditions promotes the vaporization and mixing of the liquid fuel after the end of the injection, thus shortening the liquid penetration compared to the conventional diesel conditions.

The ignition processes for PPCI also differ from those of the conventional diesel mode. Chemiluminescence is first detected near 6.0^o ASOI (see Figure 2.6), which is about 3 degrees later than for the conventional conditions. By 8.0^o ASOI, formaldehyde (violet), an important product of low-temperature oxidation reactions, is distributed throughout most of the jet. In contrast, formaldehyde only forms in the fuel-rich regions for conventional conditions. It should also be noted that the jet boundaries become wavy after the end of injection. For PPCI conditions, the second-stage ignition occurs at about 9.0^o ASOI, immediately after the end of injection. OH radicals (green) appear mainly in the downstream region when the AHRR curve reaches the peak, and surround some fuel-rich pockets (black). After a few crank angles, soot precursors and/or soot (red) form within these pockets and eventually are oxidized (40.0^o ASOI schematic).

From the introduction above, it is known that the chemical processes, like ignition, soot formation, largely depend on the "boundary conditions" provided by the physical processes (e.g., atomization, evaporation, mixing, etc.) that occur earlier. The main objective of this work, as mentioned in Chapter 1, is to gain a better understanding of the physical processes of diesel sprays in marine engines. In Chapter 3, CFD simulations involving detailed modeling of the sub-processes are utilized to predict the spray formation under engine-like conditions. Through studying the influences of the sub-processes on the spray characteristics, better insight into the "mixing-controlled" concept is obtained.

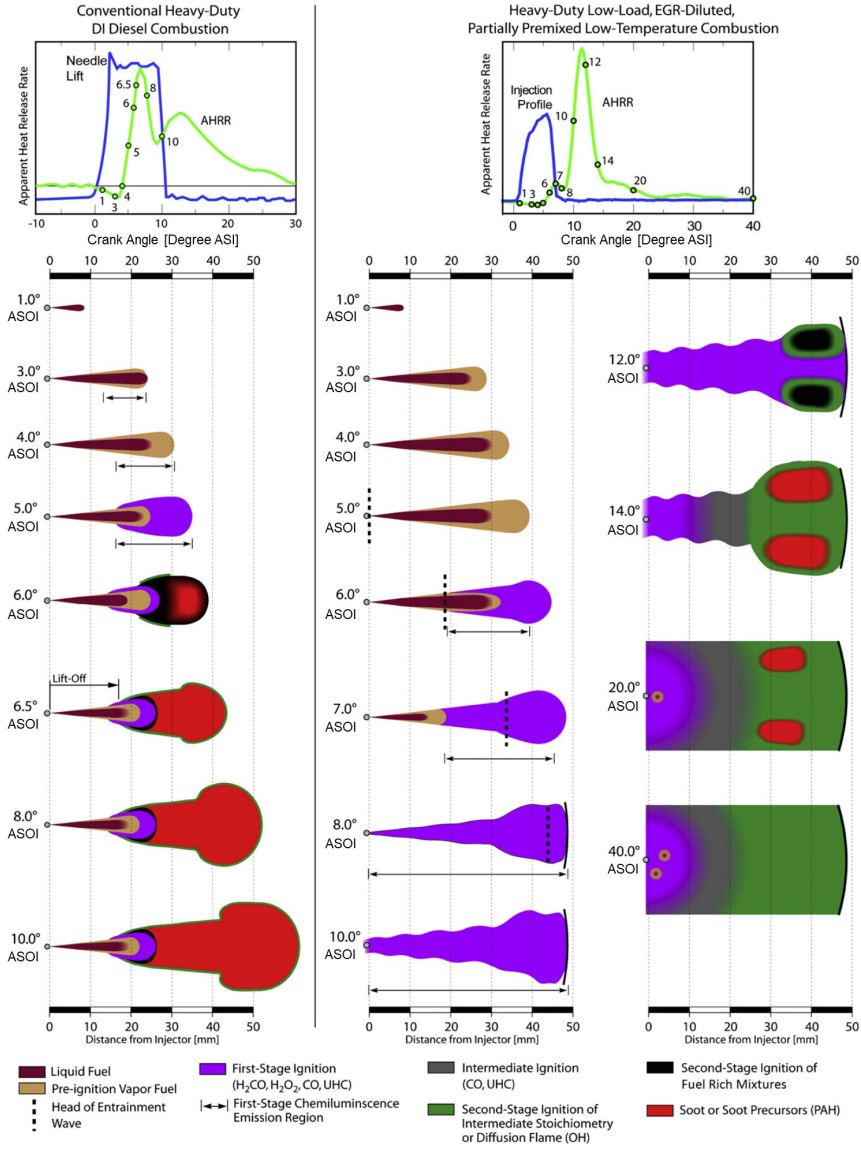

Figure 2.6: Comparison of Dec's conceptual model (left column) and PPCI LTC conceptual model [52] (middle and right column).

2.2 Spray research in optically accessible chambers

The optically accessible engine is definitely a helpful and beneficial tool for engine combustion research because its measurement represents the actual in-cylinder processes. However, this type of engine is costly and technically demanding, as can be seen from Figure 2.1. Therefore, the optically accessible combustion chamber is an alternative for spray research. In combustion chambers, a high-temperature high-pressure environment is created to mimic the real engine conditions at the start of injection.

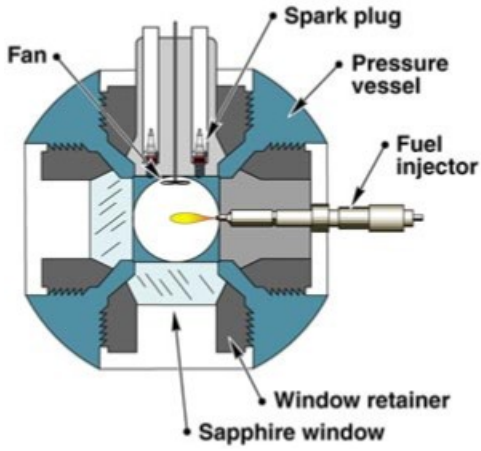

(a) A schematic of the Sandia Combustion Vessel [54].

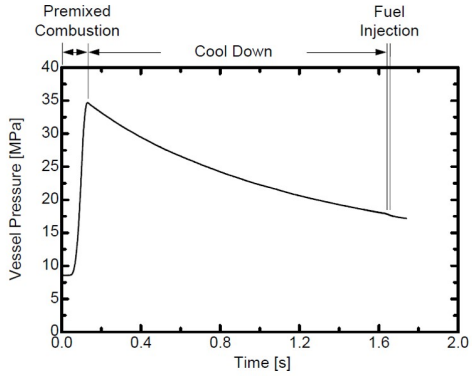

(b) Pressure history in a pre-combustion chamber [55].

Figure 2.7: The Sandia Combustion Vessel using the pre-combustion method.

Two methods are used to provide the high-temperature and high-pressure conditions:

- Pre-combustion. Figure 2.7 shows the combustion chamber used by Siebers et al. [55–57]. A spark plug in the combustion chamber ignites a pre-computed gas mixture (e.g., C_2H_2, H_2, O_2, N_2). Fuel injection starts when the pressure and temperature in the chamber, resulting from the combustion, reach the target condition. The time constant of the cooling process is much larger than that of the spray penetration experiments (typically less than 5 ms), as can be seen in Figure 2.7, so that the pressure during the fuel injection process can be considered as constant to a good approximation.
- Constant pressure flow. Figure 2.8 illustrates the constant pressure flow chamber used by Payri et al. [58, 59]. Unlike the pre-combustion method, the gas is first pressurized and heated outside and then flows into the chamber.

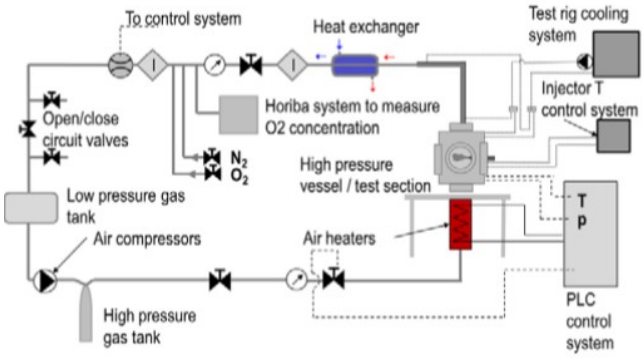

Figure 2.8: The constant pressure flow chamber [58, 59].

Extensive research has been conducted in optically accessible combustion chambers worldwide. The following sections will introduce the experimental data used to validate the spray modeling in this work.

2.2.1 Engine Combustion Network

Due to its complexity, engine combustion research requires substantial effort. Quantitative measurement data under engine-like conditions gives a better understanding of the relevant problems and is necessary for model development and simulation validation. To ensure the reliability and reproducibility of the measurement data, the Engine Combustion Network (ECN), an international collaboration among researchers in engine combustion, was launched in 2009, initialized by Sandia National Laboratories.

Within the ECN, "identical" injection systems, which represent modern advanced injection systems with high-pressure capability, donated by Robert Bosch LLC made the experimental collaboration among different working groups possible. A low-temperature combustion condition relevant to engines using moderate EGR was set as the baseline case, namely "Spray A", for the first target diesel spray research. To keep the boundary conditions the same in different combustion chambers (including the pre-combustion and pressure flow types mentioned above), extensive work has been done. Finally, results obtained from different facilities show good agreement [60]. To date, over 75 different diagnostics have been performed by more than 20 institutions at Spray A conditions [61].

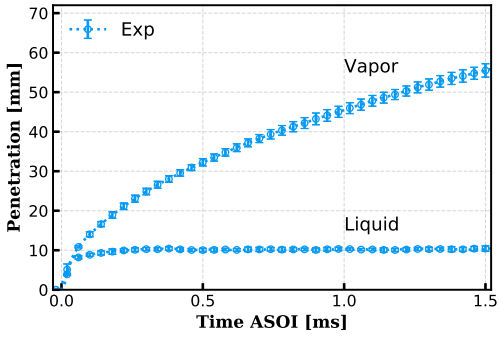

Figure 2.9: Experimental data of vapor and liquid penetration of Spray A

Over the last decade, large databases with high-quality experimental results have been generated and now are available on the ECN website[5]. The Spray A (SA) database, with a prescribed injector nozzle (90 μm), contains vapor and liquid penetrations, mixture distributions, ignition delay [62], lift-off length [63], and soot volume fraction [64, 65]. In recent measurements [66], a larger nozzle hole (190 μm) was used to characterize the Spray D (SD).

[5] Experimental data are available at http://ecn.sandia.gov/.

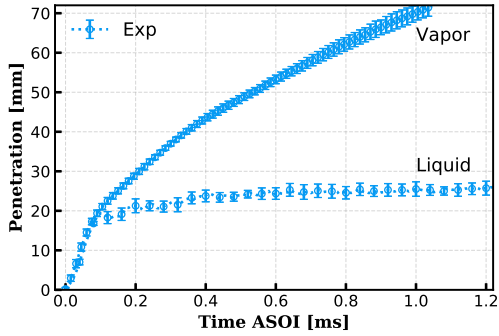

Figure 2.10: Experimental data of vapor and liquid penetration of Spray D

In this work, the ECN cases SA and SD are first used to validate the spray models. The data employed for validation is the vapor-phase and liquid-phase penetration. The macroscopic or global characteristics (e.g., vapor-phase penetration, liquid-phase penetration, shown in Figure 2.9 and 2.10) are often employed for validation because their measurements are relatively straightforward [67]. As mentioned, many diagnostics have been conducted for the SA case. The fuel/air mixture distribution is also utilized for further validation (see Figure 2.11).

Extensive numerical work [68–74] has also been performed by different research groups within the ECN. These studies typically consider orifice diameters that are representative of passenger car and heavy-duty engines.

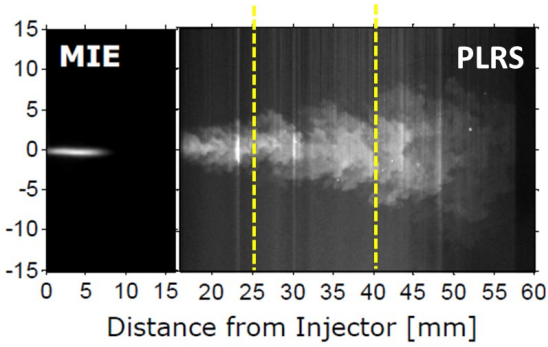

(a) A composite schematic of Mie scattering and PLRS. Two dashed yellow lines indicate the mixture formation data used for validation. The original image is taken from Ref. [67].

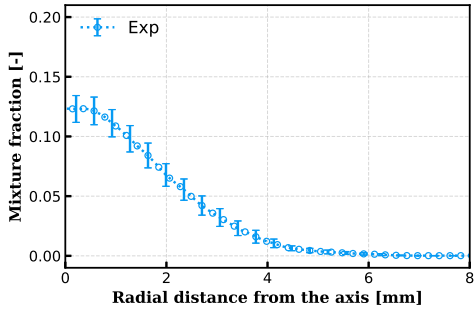

(b) Mixture formation distribution along the radial position at 25 mm downstream the nozzle exit.

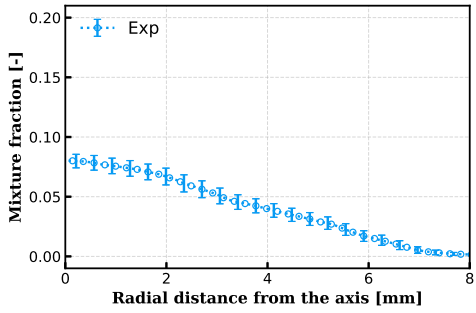

(c) Mixture formation distribution along the radial position at 40 mm downstream the nozzle exit.

Figure 2.11: Quantitative mixing measurements of Spray A.

2.2.2 Spray research for medium speed marine engines

As mentioned in Chapter 1, due to the larger nozzle and cylinder size, the evaporation, mixing, and combustion processes differ from those of car and truck sized engines. Waldenmaier et al. [75] designed an endoscopic optical access on an MAN Diesel single cylinder medium speed engine, and performed CFD simulations with a modified version of KIVA3V incorporating their in-house models. The authors found that although the simulation shows very good agreement of cylinder pressure, temperature, heat release rate and the overall soot concentration in comparison to engine data, the local soot distribution deviates. Therefore, the study of spray characteristics in optically accessible combustion chambers is still very valuable to deepen the understanding of the process.

The following sections present recent advances in spray research in optical chambers for medium speed marine engines, mainly from Shanghai Jiao Tong University (SJTU) and Ghent University (UGent).

Spray research at SJTU

In recent years, researchers at SJTU collaborated with the Shanghai Marine Diesel Engine Research Institute and conducted a series of works for sprays in a large constant volume chamber based on medium speed marine engine size. This chamber has an inner diameter of 300 mm and is equipped with three 140-mm-diameter quartz windows to capture the spray images. Unlike the Sandia Combustion Vessel, this chamber is a constant pressure flow chamber, as shown in Figure 2.12. A pre-heating device heats high-pressure nitrogen before it enters the chamber. The maximum temperature and pressure that can be achieved are 900 K and 6 MPa, respectively.

Employing three kinds of optical techniques (backlight high speed imaging technique, Ultraviolet/Visible Laser absorption-scatter and Laser-induced fluorescence/Mie), Zhang et al. [77] studied the spray and evaporation process. The authors also introduced a correction factor of temperature in the empirical correlation of Sauter mean diameter proposed by Hiroyasu et al. [78] and obtained good agreement with the experimental data.

As discussed in Section 1.3, turbocharging is a mature technology that has been used in marine engines. With a further increase of charge pressure, the in-cylinder conditions can exceed the critical point of diesel fuel. Due to significant enhancement in liquid gas mixing under supercritical conditions, the supercritical diesel combustion concept was proposed by Tavlarides et al. [79–81]. Xia et

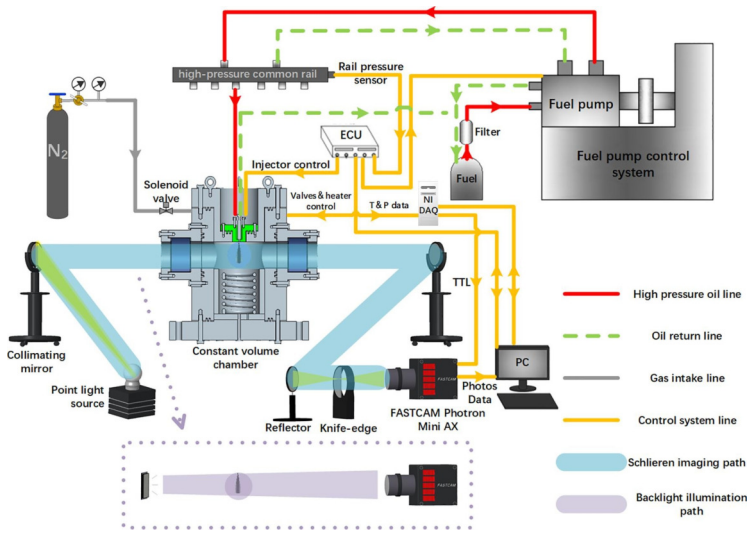

Figure 2.12: The constant volume chamber at SJTU [76].

al. [76, 82, 83] conducted experimental investigations of diesel spray under subcritical, transcritical, and supercritical conditions. Some important findings are listed as follows:

- The liquid phase boundary under supercritical conditions is quite smooth and stable compared with that under sub/transcritical conditions. This is mainly due to the reduced gas-liquid interface and surface tension forces under supercritical conditions.
- Under the same ambient gas temperature, the vapor penetration decreases rapidly when the ambient gas pressure increases from subcritical to supercritical values.
- When the ambient pressure is above the critical point, the reduction of liquid length is more pronounced with ambient temperature.
- Huang et al. [84] formulated a six-component surrogate of commercial diesel. Xia et al. [82] compared the spray characteristics of surrogate fuel and diesel under a wide range of ambient conditions, and found this six-component surrogate can emulate important spray parameters (e.g., penetrations, cone angles) under trans/supercritical conditions with 5% errors.
- The liquid length and spray cone angle correlations proposed based on the previous experimental results [58, 85–87] of automobile engines are also

examined by Xia et al. [83], and the authors found that these correlations are generally applicable to marine engines. The ambient gas temperature is a dominating factor for the liquid length under transcritical conditions, while the nozzle diameter demonstrates its importance under supercritical conditions. For spray cone angle, the ambient pressure has an obvious influence for both trans/supercritical conditions.

Spray research at UGent

In this work, measurements of marine engine sprays will be used, that were conducted in the GUCCI setup by a previous researcher [88]. This constant volume combustion chamber has a volume of 160^3 mm^3 and optical access in two directions through quartz windows of 150 mm in diameter. Figures 2.13 - 2.15 show the general features of the GUCCI setup. Following the procedures within the ECN, n-dodecane, as reference fuel, is used for all the measurements.

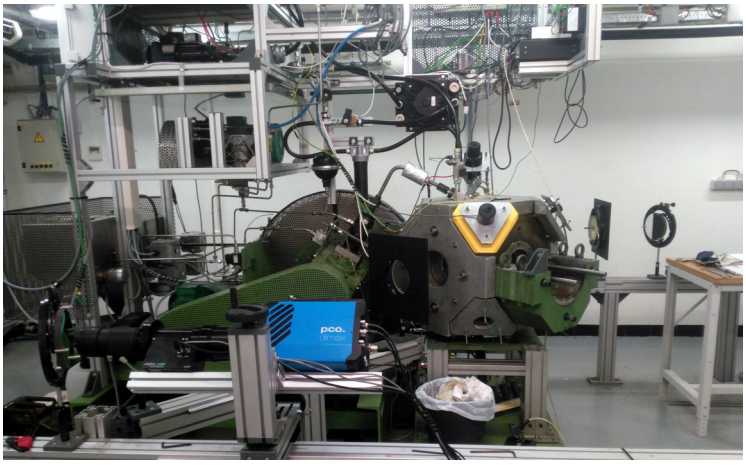

Figure 2.13: Picture of the entire GUCCI setup [88].

The results from a calibrated 1D engine simulation code [88] showed that, for a typical medium speed marine engine with a power of around 200 kW per cylinder, ambient conditions vary from 10 kg/m^3 and 750 K (25% load) to 40 kg/m^3 and 900 K (100% load) at the start of injection without EGR. In this work, a slightly lower density is chosen to protect the test bench. The target condition (high density and temperature) is achieved by using the pre-combustion method. The measurements are performed in accordance with the conditions summarized in the test matrix shown in Table 2.2, and the ambient conditions and injection profile for each case are plotted in Figure 2.16.

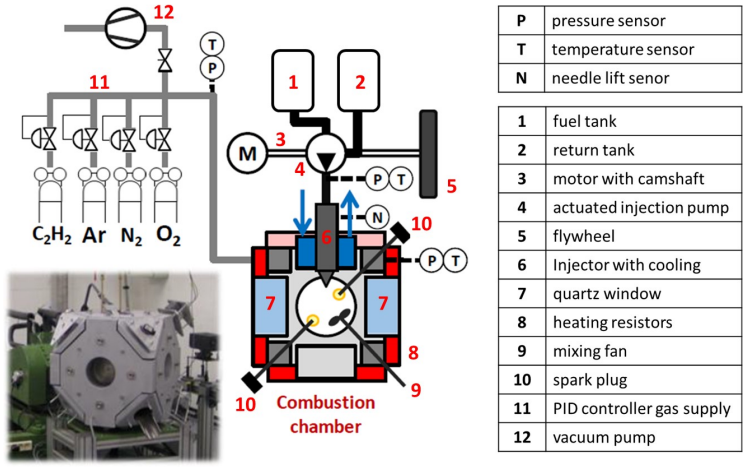

P	pressure sensor
T	temperature sensor
N	needle lift senor

1	fuel tank
2	return tank
3	motor with camshaft
4	actuated injection pump
5	flywheel
6	Injector with cooling
7	quartz window
8	heating resistors
9	mixing fan
10	spark plug
11	PID controller gas supply
12	vacuum pump

Figure 2.14: Schematic overview of the GUCCI setup

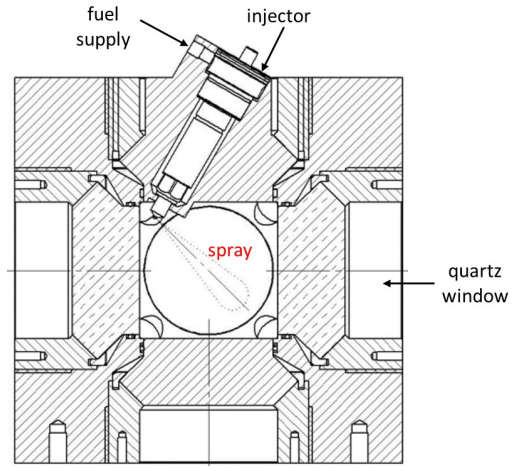

Figure 2.15: Technical drawing of the GUCCI chamber

Table 2.2: Test conditions summary. T_g is the ambient gas temperature, ρ_g is the ambient gas density, D_n is the injector nozzle diameter, P_{pe} is the peak injection pressure, and LL is the liquid length, respectively.

Case	T_g (K)	ρ_g (kg/m^3)	D_n (mm)	P_{pe} (MPa)	LL (mm)
1	700	15.2	0.44	65 ± 2	68.3 ± 1.5
2	850	7.6	0.44	65 ± 2	77.0 ± 1.7
3	850	15.2	0.44	65 ± 2	55.5 ± 2.1
4	850	22.5	0.44	65 ± 2	52.6 ± 1.5
5	850	22.5	0.44	79 ± 3	49.6 ± 1.8
6	850	22.5	0.38	79 ± 3	43.1 ± 2.8
7	950	15.2	0.44	65 ± 2	42.4 ± 1.4

A Pump-Line-Nozzle (PLN) fuel injection system, originating from a medium speed marine engine manufactured by Anglo Belgian Corporation, is used. While the 10-hole nozzle with individual hole diameter of 0.38 mm is used for Case6, the 8-hole nozzle with hole diameter of 0.44 mm is used for the other tested cases. To study a single fuel spray from the multi-hole injector, to avoid interference and optical obstruction, a thimble is constructed covering all but one orifice. The fuel delivered by the other covered orifices is led to the bottom of the combustion chamber by a drainpipe. The influence of the thimble on the spray has been studied previously [89, 90]: the influence on the injection pressure and spray momentum were compared in the cases with and without a thimble. No significant difference in injection pressure or spray momentum could be detected. Different from many high speed diesel engines, where common rail injection systems are usually utilized, the injection system consists of a line pump that feeds the PLN system. While the PLN system is being replaced by the common rail injection system in new engine designs, this fuel injection system is still the most widely used system in marine markets. In contrast to the common rail system, which shows a "top hat" injection profile, used in many studies [55, 56, 58, 91, 92], the PLN system has a "triangle-shaped" injection profile (see Figure 2.16(b)). Case5 and Case6, in which more fuel is injected, represent the injection behaviors at a relatively higher engine load compared to the other five cases.

The visualization setup in this paper is a classical Z-type system, shown schematically in Figure 2.17, which has been extensively used for spray measurements [93–97]. A Schlieren technique is used to measure the vapor penetration and spray spreading angle. The light source is a green LED

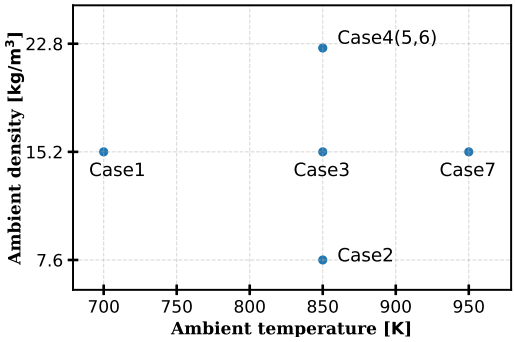

(a) Ambient temperature and density

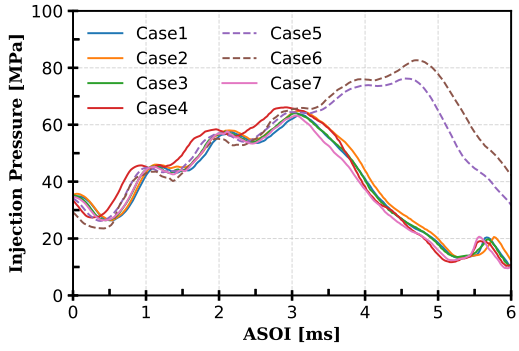

(b) Injection profile

Figure 2.16: Ambient conditions and injection profile for each case.

(light-emitting diode). The light beam, produced by the LED, is focused through a pinhole and collimated by a lens (the right one in Figure 2.17). The beam is then guided through the test zone (i.e. spray injected) by a reflecting mirror. The portion of the beam passing through the combustion chamber is refocused by a second lens (the left one in Figure 2.17) located downstream of the chamber. Refracted light is prevented from entering the camera lens by positioning a Schlieren stop in the focal point right before the camera.

Mie scattering imaging is used for liquid phase detection. Liquid droplets are illuminated by another LED light source, mounted perpendicular to the Schlieren optical axis. One line of sight technique (e.g. Schlieren) and one perpendicular technique (e.g. Mie scattering) can be combined by the frame straddling approach [98, 99]: the Schlieren and Mie LED light sources were alternately activated at

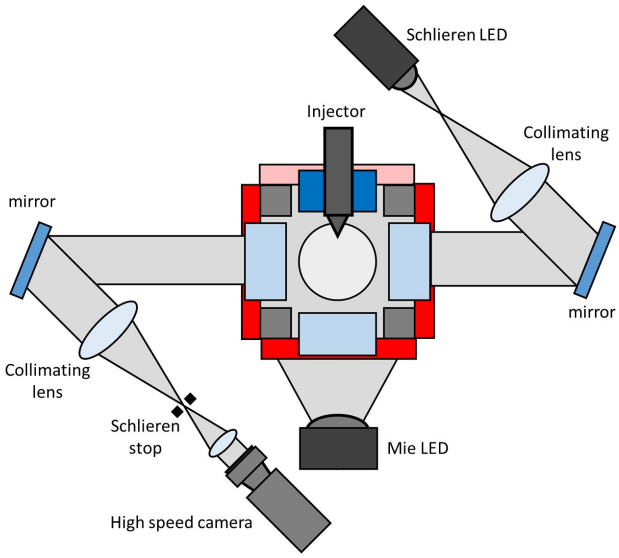

Figure 2.17: Schematic of optical setup

half the camera frequency to acquire both techniques with one camera during each measurement. Images were recorded at a frequency of 20 kHz and a pixel resolution of 460×288 by a high-speed camera (PCO DiMax). Exposure time was kept constant at 5 μs during the experiments and was determined by the electronic shutter (gate) of an image intensifier (Lambert Instrument HiCATT).

More detailed descriptions about the setup, optical technique and image processing have been reported by previous Ph.D. students [88, 100]. In this work, as the thimble obstructs the very first part of the spray penetration, the definition of the SOI is from Naber and Siebers [56]. As shown in Figure 2.18, a function is used to fit the penetration data within 30 mm, and its intersection with the horizontal axis is defined as the SOI.

The effects of ambient temperature, ambient density, nozzle diameter and injection profile on marine engine sprays are now presented briefly.

The effect of ambient gas temperature on the spray (vapor and liquid) penetration is studied with different temperatures (700 K, 850 K and 950 K) while keeping the gas density and injection pressure constant. Figure 2.19(a) shows the temporal evolution of the vapor penetration at different ambient temperatures for the same ambient density and injection pressure. It shows that all curves overlap from 0 to 0.8 ms ASOI, but small deviations are observed afterwards. At the highest temperature (950 K) tested, the vapor phase penetration drops slightly compared

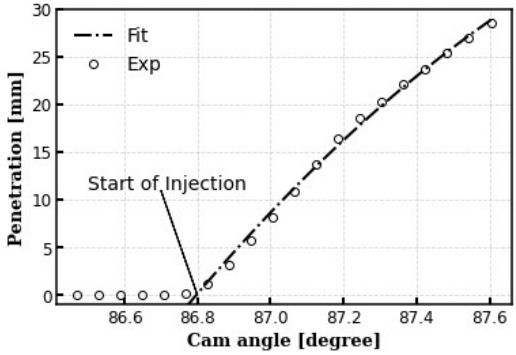

Figure 2.18: An example showing the definition of the start of injection.

to other conditions (700 K and 850 K). The observations in Figure 2.19(a) are consistent with other works [58, 59, 77, 101].

Concerning the liquid phase, the influence of ambient temperature, as expected, is obvious. The liquid penetration is longer when the ambient temperature is lower. But the overlapping of three curves still exists before 0.8 ms ASOI, which is similar to the vapor phase. As explained by Zhang et al. [77], due to the relatively large droplet size and long evaporation time during a certain period of time after injection, the ambient temperature has little effect on the liquid penetration. Another phenomenon observed in this study is that for some cases (such as, Case1, Case3 and Case2 in Figure 2.20(b)) the liquid penetration first reaches a peak and then suddenly drops to a lower relatively stable length. This is likely due to the combination of two effects: one effect is the evolution of the injection pressure caused by the Pump-Line-Nozzle system used in this work. As shown in Figure 2.16(b), the pressure profile is "triangle-shaped" with fluctuations. This phenomenon will be discussed in more detail in the next chapter with the CFD results, and the other effect (named ligament detachment) is also investigated. The liquid length, is the maximum length of liquid in the spray that has reached stabilized conditions, where the evaporation rate is the same as the fuel renovation rate [58]. As opposed to the liquid penetration (S_l), which depends on time, the liquid length is a stabilized value. In the present work, the maximum length of liquid is not so stable compared to the measurements in Ref. [58], this is due to the pressure waves [102] and unsteady injection pressure in the PLN system as mentioned above. In order to make quantitative comparisons, the determination of the liquid length for each case (see Table 2.2) is similar to the method used by Siebers [55] and Payri et al. [58]. The liquid length decreases by approximately 30% when ambient temperature increases from 700 K (68.3 mm) to 850 K (55.5 mm) but decreases by a maximum of 12% when the temperature further increases

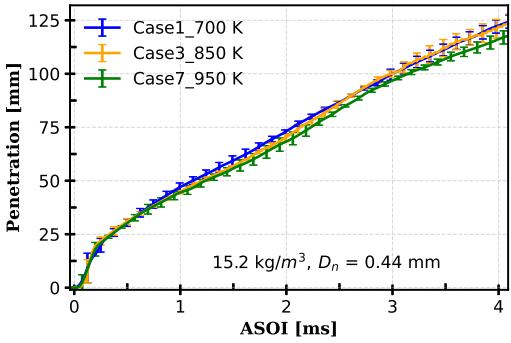

(a) Vapor

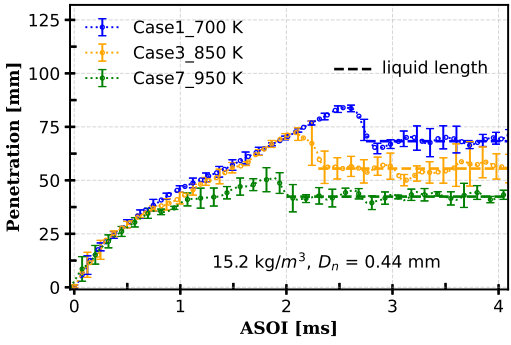

(b) Liquid

Figure 2.19: Penetration comparison between different ambient temperatures

to 950 K (42.4 mm).

Figure 2.20 demonstrates the effect of ambient gas density on spray penetration. The data were obtained at an ambient temperature of 850 K over a gas density range from 7.6 to 22.5 kg/m^3 with the 0.44 mm orifice diameter. Due to stronger resistance with higher ambient gas density, a slower penetration, of both vapor and liquid phase, can be observed with ambient gas density increasing. However, this effect is non-linear, since the difference between Case3 and Case4 is less evident compared to that between Case2 and Case3. Similarly, it is also noticeable in Figure 2.20(b) that the higher gas density is, the lower the liquid length that is obtained, but the decrease from Case3 (55.5 mm) to Case4 (52.6 mm) is slight compared to the decrease from Case2 (77.0 mm) to Case3. Siebers [55] derived a simple conceptual spray model by applying conservation of mass and momentum

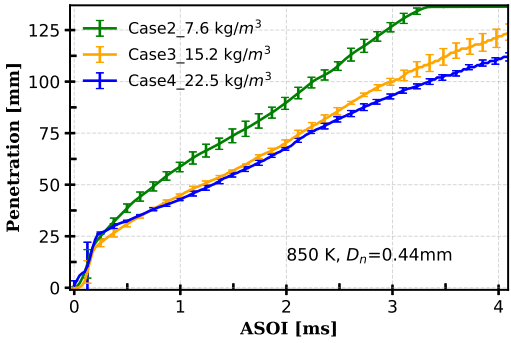

(a) Vapor

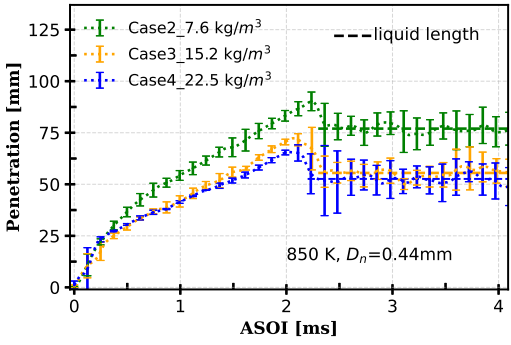

(b) Liquid

Figure 2.20: Penetration comparison between different ambient densities

and found the entrained gas mass is proportional to the square-root of the gas density, which partially explains the non-linear effect of ambient gas density. The non-linear effect of gas density, observed by many authors [55, 58, 91, 101], however, is more complex than the description above and still needs more detailed analysis.

The influence of nozzle diameter is shown in Figure 2.21. From the observations, the diameter effect is not evident, which might be due to the relatively high density value used here. Payri et al. [58] combined the results from Refs. [101, 103] and found that the diameter influence is more evident at the low gas density condition, but the effect becomes less important when the density is high. The effect of the nozzle diameter is studied under a relatively high ambient density condition. As can be seen in Figure 2.16(b), the injection profiles for these two cases are not

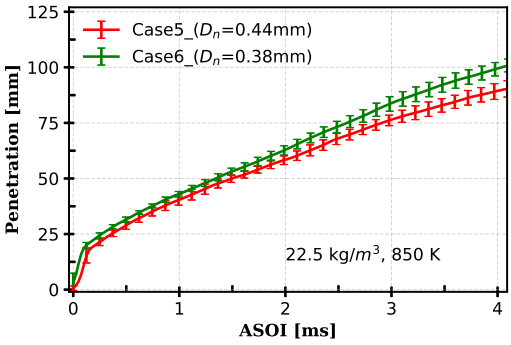

(a) Vapor

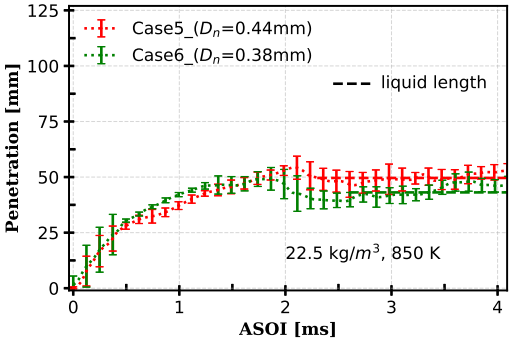

(b) Liquid

Figure 2.21: Penetration comparison between different nozzle diameters

exactly the same. For vapor phase penetration (S_v), the difference between the two cases is slight from 0 to 2 ms ASOI, but after that, Case6 with the smaller nozzle diameter has a higher penetration compared to Case5. A possible explanation is that after 2 ms ASOI, the injection pressure for Case6 is higher. On the other hand, the comparison of two nozzles (D194 with diameter of 194.4 μm, D228 with diameter of 228.8 μm) by Payri et al. [58] showed that the influence of the nozzle diameter is very small, although it is suggested in the literature that a larger diameter increases spray penetration [101]. Concerning the liquid phase, Figure 2.21(b) shows that the nozzle diameter has a negligible effect at the beginning of the injection event, nonetheless once the stabilized liquid length is reached, the effect is evident, where the bigger nozzle diameter leads to a longer liquid length (Case5 of 49.6 mm, Case6 of 43.1 mm). The observation is in agreement with other researchers [57, 101, 103].

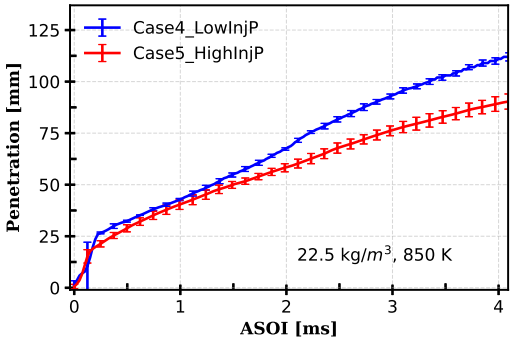

(a) Vapor

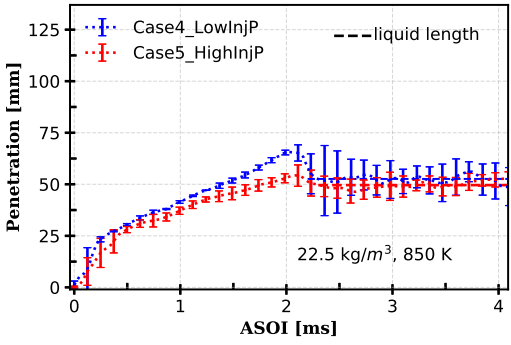

(b) Liquid

Figure 2.22: Penetration comparison between different engine loads

The influence of engine load (or injection profile) is investigated by comparing Case4 and Case5. It is shown in Figure 2.22(a) that the vapor penetration of Case4 (with lower and earlier peak injection pressure) is longer than the measured data of Case5, but before approximately 1.5 ms ASOI the difference between the two cases is small. The liquid length is less sensitive to the engine load according to the results shown in Table 2.2. Similar results are also found by other researchers by performing measurements with a wider injection pressure range (110-160 MPa in Ref. [77], 50-150 MPa in Ref. [91]). The liquid phase morphology and spray angle is strongly coupled with nozzle flows [91], which need to consider the effect of cavitation and turbulence. A possible reason for the vapor penetration behavior will be discussed in Chapter 4 with the empirical spray penetration model.

Thus, to summarize the above, evaporating sprays for medium speed marine engines were measured in a constant volume combustion chamber. The influence of ambient gas temperature, ambient gas density and injector nozzle diameter on spray development was investigated under engine-like conditions. The ambient condition effects on spray characteristics for large size marine engines are generally consistent with the findings in automobile size diesel engines: the ambient gas temperature has only a slight influence on the vapor phase, but promotes the evaporation; the higher gas density leads to slow penetration speed, lower liquid length and wider spray angle, but the effect is non-linear. The nozzle hole diameter has a negligible effect on the global spray morphology at relatively high ambient gas density (22.5 kg/m^3).

2.3 A literature review on CFD simulations of diesel sprays

The previous discussion shows that experimental research for engine sprays is expensive, especially for marine engines. For this reason, CFD simulation is essential and indispensable in engine research and development. In this section, the recent advances in CFD simulation of engine sprays are presented.

Engine spray atomization and breakup is a popular research direction. Since Reitz [104] introduced the Kelvin-Helmholtz (KH) instability in 1987, this aerodynamic-induced regime has been seen as one of the dominant factors of breakup. Through the experimental observation [105], the Rayleigh-Taylor (RT) instability, caused by the rapid deceleration of the droplet, is also considered another important breakup mechanism for engine sprays. The combined KHRT model, in which both models are implemented in a competing manner, is widely used for diesel spray simulations [106, 107]. A more detailed discussion on the model and mathematical description will be given in Chapter 3.

In recent years, many researchers [108–111] have developed more accurate models based on this classical KHRT model. Som et al. [110] found that the classical KHRT model slightly overpredicted liquid length and vapor penetration. The X-Ray adsorption measurement [112, 113] from Argonne National Laboratory showed that this overprediction is caused by the near nozzle flow conditions. Som et al. [109, 110] developed the KH-ACT model, which considers the turbulence-induced and cavitation-induced breakup. This KH-ACT was validated under a wide range of non-reacting and reacting conditions. The inclusion of cavitation and turbulence enhances the spray breakup process and increases the radial dispersion. The results of KH-ACT also showed better agreement with the

flame lift-off length measurement. The KH-ACT model has been incorporated into the CONVERGE CFD code. Mohan et al. [111] also implemented this model into the KIVA4 CFD code. But the near nozzle flow condition from the X-ray data is not easily available in most engine spray test benches.

Zhu et al. [114, 115] combined the laser-induced fluorescence-particle image velocimetry (LIF-PIV) technique and CFD simulations to investigate the ambient gas entrainment of non-evaporating diesel sprays. The authors categorized the spray into three regions according to the spray-ambient gas interaction from the numerical and experimental results.

- Entrainment section: In this region, surrounding gas is entrained to the spray due to the pressure gradient induced by the fuel injection.
- Recirculation section: The droplets upstream push aside the droplets at the tip, causing the motion in the radial direction. At the same time, the entrainment of surrounding gas continues. These two factors create this recirculation.
- Tip section: The surrounding gas is pushed away by the spray.

Zhu et al. [115] also investigated the influence of injection pressure, ambient gas density, and nozzle hole diameter on air entrainment, and concluded the following:

- The air entrainment is improved with the increase in injection pressure, but the ultra-high injection pressure would not significantly increase the entrainment.
- A higher ambient gas density increases the mass flow rate of ambient gas entrained.
- The decrease of nozzle hole diameter reduces the entrainment rate of the surrounding gas.

Gong et al. [116] performed large eddy simulations to study the air entrainment and mixing phenomenon in diesel sprays and found the three-category regions proposed by Zhu et al. [114, 115] to also be applicable to evaporating (non-reacting) and reacting sprays. The flow field comparison between non-reacting and reacting diesel sprays showed combustion-induced thermal expansion improves the penetration at the spray tip and enhances the gas recirculation. Cool flame reduces air entrainment to the spray.

Due to the complex nature of the turbulent flow, turbulence modeling in diesel spray CFD is also an important research area. The standard $k-\varepsilon$ model and the RNG $k-\varepsilon$ model are often used in spray simulation codes. For example, many researchers [72, 108–110, 117, 118] found the performance of the RNG model is better than the standard model from the simulation results obtained by the KIVA code and CONVERGE code. On the other hand, recent studies [68, 69, 119] from the ECN groups showed the standard model provides a better fit with the experimental data in OpenFOAM. Wei et al. [72] using the KIVA code compared the performance of these two models on diesel spray simulations and found the standard model can also obtain the same good agreement by adjusting the value of the important model constant. Chapter 3 will further discuss the effect of turbulence modeling.

2.4 Closure

The objective of Chapter 2 was to give a comprehensive introduction to diesel sprays. Thus, this chapter first described how a fuel spray combustion develops in diesel engines. The relevant physical and chemical problems are discussed with a well-known diesel combustion conceptual model, in which fuel vaporization, autoignition, and soot formation are included. The PPCI LTC conceptual model is also introduced due to its potential for emission reduction, but its application is currently mainly at low-load operating conditions of heavy-duty engines. After that, the experimental data used in this work for validation was presented, with the main features that should be captured in the numerical work which is the topic of the next chapter. Section 2.3 presents the recent advances in some aspects of diesel spray CFD simulations related to the research in this work. Further discussion on CFD simulations will also be given in Chapter 3.

3

CFD studies of diesel sprays

This chapter describes the content relating to the CFD studies of diesel sprays: section 3.1 gives an overview of the governing equations for both the gas phase and liquid phase; section 3.2 briefly introduces the numerical methods and the CFD code employed in this study; section 3.3 covers the CFD results obtained from different types of diesel engine sprays and explores the difference in terms of the numerical modeling processes; section 3.4 summarizes the conclusions drawn from the CFD studies in the chapter.

3.1 Governing equations

As introduced in previous chapters, the diesel spray is a two-phase flow, which brings challenges for numerical modeling, because the interaction between the liquid phase and gas phase needs to be considered [120]. Generally, there are two approaches for spray modeling: the Eulerian-Eulerian (EE) approach and the Eulerian-Lagrangian (EL) approach. In the EE approach, both liquid and gas are treated in a Eulerian way, i.e., they are a continuum. The same discretization and similar numerical techniques are employed for both phases, thus requiring the cell size to be small to track the interface between different phases [121]. This is also a challenge for computational power. The EE approach is mainly used to

study physical phenomena (liquid jet instability, primary atomization, etc.) that occur at the dense spray region near the nozzle exit (as shown in Figure 3.1, the dense regime). In the EL approach, the gas phase is treated as a continuous phase in a Eulerian way, whereas the liquid fuel is described as computational parcels, which represent droplets with the same properties (diameter, mass, velocity, etc.). Source terms are introduced to consider the phase interaction. Compared to the EE approach, the computational cost of the EL approach is lower [121].

Jenny et al. [122] proposed a general suggestion for choosing the approach for the spray modeling following the classification based on liquid-phase volume fraction: if the research mainly focuses on the dense regime, the EE approach is preferred. Otherwise, the EL approach is a better choice.

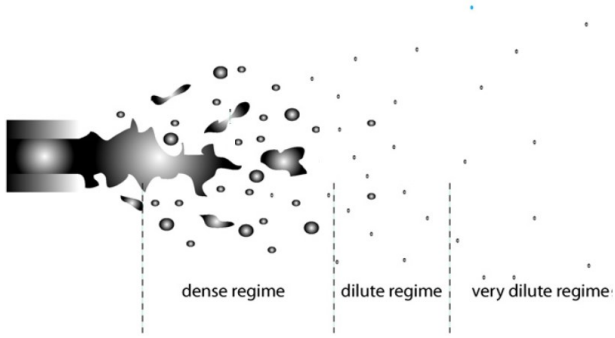

Figure 3.1: Sketch of flow regimes in sprays [122].

The main research interest of this work is the dilute regime. Thus the EL approach is employed to model the fuel spray.

3.1.1 Gas phase

In a Eulerian method, the conservative form of the transferable property (mass, momentum, energy, etc.)[1] can be described using the Reynolds transport theorem [123].

The conservation equation of mass can be written as follows:

$$\frac{\partial \rho}{\partial t} + \nabla \cdot (\rho U) = \dot{S}_p \tag{3.1}$$

[1] The corresponding expression in OpenFOAM code is given the Appendix A.

where ρ is the gas density, t is time, U is the velocity vector field, and $\dot{S}_p$ is the source term[2] representing the rate of change in vapor mass by evaporation.

Generally, the gas mixture in ICEs can have a varying composition. Additionally, the liquid evaporation and combustion reactions also change the composition of the mixture. The mass conservation equations for individual species should thus also be considered:

$$\frac{\partial Y_i}{\partial t} + \nabla \cdot (\rho U Y_i) = \nabla \cdot [(\mu + \mu_t)\nabla Y_i] + \dot{S}_{p,i} + \dot{S}_{chem,i} \tag{3.2}$$

where Y_i is the mass fraction of species i in the mixture, i.e. :

$$Y_i = \frac{\rho_i}{\rho} \tag{3.3}$$

Here, ρ_i is the partial density of species i. μ is the dynamic molecular viscosity of the gas phase and μ_t is the turbulent viscosity.[3] The source terms $\dot{S}_{p,i}$ and $\dot{S}_{chem,i}$ denote the rate of change due to evaporation and chemical reactions (for non-reacting sprays, this latter term is 0).

The momentum equation for the gas mixture can be written as:

$$\begin{aligned} \frac{\partial \rho U}{\partial t} + \nabla \cdot (\rho U U) = &-\nabla p + \nabla \cdot [(\mu + \mu_t)(\nabla U + (\nabla U)^T)] \\ &-\nabla \cdot [(\mu + \mu_t)(\frac{2}{3}\mathbf{tr}(\nabla U)^T)] + \rho g + \dot{S}_M \end{aligned} \tag{3.4}$$

In this equation, $\dot{S}_M$ is the momentum exchange rate between the liquid droplets and the gas phase. The gravitational effect g is reported to have a minor effect on the spray, and is thus often neglected in spray simulations [124]. The term **tr** denotes the trace operator on matrices.

The energy conservation equation is expressed in term of enthalpy h as:

$$\frac{\partial \rho h}{\partial t} + \nabla \cdot (\rho U h) = \nabla \cdot [(\alpha + \alpha_t)\nabla h] + \dot{S}_Q + \frac{Dp}{dt} \tag{3.5}$$

where α and α_t are respectively the thermal diffusivity and the turbulent thermal diffusivity of the gas phase. The source term $\dot{S}_Q$ in the equation above accounts for the energy exchange between the gas (Eulerian) and liquid (Lagrangian) phases.

According to the theory developed by Kolmogorov [125], turbulence consists of eddies with different length and time scales. The larger eddies transfer their energy

[2] A detailed description of source terms in governing equations is presented in the Appendix B.

[3] The calculation of the turbulent viscosity μ_t (and the turbulent thermal diffusivity α_t in Eq. (3.5)) will be introduced in the turbulence modeling.

to smaller eddies until they reach the smallest turbulent eddies characterized by the Kolmogorov scales. To fully resolve the Kolmogorov scales, the Direct Numerical Simulation (DNS), which needs a very small time step and fine mesh, is necessary. This type of simulation is clearly not desirable in practical applications due to its prohibitive computational demand. The large eddy simulation (LES), in which large energy-containing scales are directly resolved and small scales are modeled, is used to capture the unsteady features of the flow [126]. The computational expense of the LES is less compared with the DNS but still high. The Reynolds Averaged Navier-Strokes (RANS) simulation, which reduces the computational cost by resolving the field variables into average and fluctuating components through different turbulence models [127], is employed in this work.

As briefly discussed in Chapter 2, according to the literature, many researchers [68, 69, 119] suggest using the standard $k-\varepsilon$ model in OpenFOAM. Therefore, in this work, the standard $k-\varepsilon$ model was used for turbulence modeling. Section 3.3 will give further clarification.

The turbulent viscosity (in Eq. (3.2) and (3.4)) and turbulent thermal diffusivity (in Eq. (3.5)) are calculated as follows [123]:

$$\mu_t = C_\mu \rho \frac{k^2}{\varepsilon}, \quad \alpha_t = \frac{\mu_t}{Pr_t} \tag{3.6}$$

where the model constant $C_\mu = 0.09$, turbulent Prandtl number $Pr_t = 1.0$[4], and the turbulent kinetic energy k and turbulent dissipation rate ε equations in OpenFOAM are expressed as:

Turbulent kinetic energy k:

$$\begin{aligned}\frac{\partial}{\partial t}(\rho k) + \nabla\cdot(\rho U k) =& \nabla\cdot\left[(\mu + \frac{\mu_t}{\sigma_k})\nabla k\right] + G - \frac{2}{3}\rho k(\nabla\cdot U) \\ & - \rho\varepsilon + \dot{S}_k\end{aligned} \tag{3.7}$$

Turbulent dissipation ε:

$$\begin{aligned}\frac{\partial}{\partial t}(\rho \varepsilon) + \nabla\cdot(\rho U \varepsilon) =& \nabla\cdot\left[(\mu + \frac{\mu_t}{\sigma_\varepsilon})\nabla \varepsilon\right] + C_1 G\frac{\varepsilon}{k} \\ & - (\frac{2}{3}C_1 - C_3)\rho\varepsilon(\nabla\cdot U) - C_2\rho\frac{\varepsilon^2}{k} + \dot{S}_\varepsilon\end{aligned} \tag{3.8}$$

where $G = \sigma_t : \nabla U$[5] is the production rate (generation) of turbulent energy due to the anisotropic part of the Reynolds-stress tensor σ_t, $\dot{S}_k$ and $\dot{S}_\varepsilon$ represent source

[4] The value of 1.0 is the default value in the OpenFOAM code. Previous studies [54, 70, 128, 129] show that the value of the turbulent Prandtl number has minor influence on simulation results.

[5] More details on the double dot product operator ":" can be found in Refs. [123, 130]

terms [131] involving the interaction with the spray (liquid phase). In the present work, values for the model coefficients C_2, C_3, σ_k and σ_ε were taken as 1.92, -0.33, 1.0, 1.3, respectively, as suggested by Ref. [106]. The value of C_1 is of importance in this work, which will be discussed later on in this chapter.

3.1.2 Liquid phase

The properties (position, velocity, temperature, etc.) of the droplets are determined in a Lagrangian way.

Injection model

The liquid fuel injection was simulated using the 'blob' method [131], in which the fuel drops at the nozzle exit are assumed to have a characteristic diameter equal to the nozzle hole diameter, see Figure 3.2. In recent years, research [109–111] has also focused on developing more accurate models that are linked with the nozzle flow conditions and relevant primary (e.g., cavitation-induced, turbulence-induced, and aerodynamic-induced) breakup mechanisms. The more detailed the model, the more data is needed. This blob-method is seen as the simplest and most popular way [106] to provide the starting condition for the diesel spray simulations.

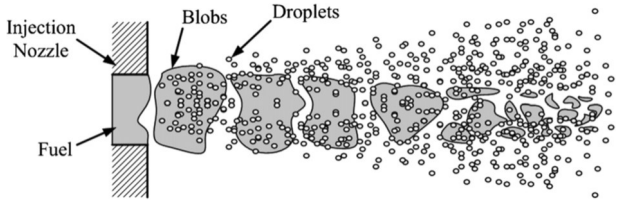

Figure 3.2: Blob injection model [121]

Breakup model

For the spray in diesel engines, the KH instability (see Figure 3.3(a)), resulting from unstable waves growing at the liquid surface [104], and the RT instability (see Figure 3.3(b)), which is caused by the rapid deceleration [105], are both important breakup mechanisms [132].

The KH mechanism postulates that the radius of child droplets (r_c) stripping from the parent droplet is proportional to the wavelength of the fastest growing unstable

wave:

$$r_c = \begin{cases} B_0\Lambda_{KH} & , B_0\Lambda_{KH} \leq r \\ \min\begin{bmatrix} (3r^2\Lambda_{KH}/4)^{1/3} \\ (3\pi r^2 u_{rel}/2\Omega_{KH})^{1/3} \end{bmatrix} & , B_0\Lambda_{KH} > r \end{cases} \tag{3.9}$$

where Λ_{KH} and Ω_{KH} are the corresponding wavelength and growth rate, r is the radius of the droplet, $u_{rel} = |u_d - U|$ is the relative velocity between liquid (u_d) and gas phase, and $B_0 = 0.61$ is a model constant. According to the work of Sazhin [133], $B_0 = 0.61$ corresponds to the well-known condition of the bag breakup. Therefore, the value of B_0 is fixed. Λ_{KH} and Ω_{KH} are calculated as follows:

$$\Lambda_{KH} = 9.02r\frac{(1+0.45Oh^{0.5})(1+0.4Ta^{0.7})}{(1+0.87We_g^{1.67})^{0.6}} \tag{3.10}$$

$$\Omega_{KH} = \left(\frac{\sigma}{\rho_d r^3}\right)^{0.5}\frac{(0.34+0.38We_g^{1.5})}{(1+Oh)(1+1.4Ta^{0.6})} \tag{3.11}$$

with

$$Oh = \frac{\sqrt{We_l}}{Re_l}, \quad Ta = Oh\sqrt{We_g},$$
$$We_g = \frac{\rho r u_{rel}^2}{\sigma}, \quad We_l = \frac{\rho_d r u_{rel}^2}{\sigma}, \quad Re_l = \frac{\rho_d r u_{rel}}{\mu_l}$$

where Oh, Ta, We_g, We_l, Re_l, σ, μ_l, ρ_d are the Ohnesorge number, the Taylor number, the Weber number for gas phase, the Weber number for liquid phase, the Reynolds number for liquid phase, surface tension, liquid viscosity and density of the liquid droplet, respectively. The droplet size is reduced according to the reduction rate:

$$\frac{dr}{dt} = -\frac{r-r_c}{\tau}, \quad \tau = \frac{3.788B_1 r}{\Lambda_{KH}\Omega_{KH}} \tag{3.12}$$

Here, B_1 is the time constant for the KH breakup model, which was set to 40 [134, 135] for all the simulations in this work. It is well acknowledged that the breakup time is affected by many factors, like initial disturbance levels and nozzle flow conditions, and nozzle designs. Due to the existing difficulties in quantifying these effects, B_1 is regarded as an adjustable model constant [104]. The influence of its value on spray prediction will be studied in the following diesel spray cases.

In the RT mechanism, the equations for the wavelength (Λ_{RT}) and frequency (Ω_{RT})

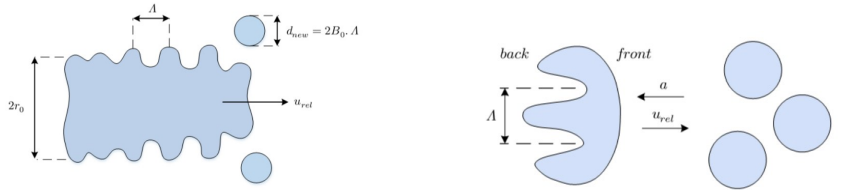

(a) KH (b) RT

Figure 3.3: Schematics of KH and RT breakup mechanism [124]

of the fastest growing waves are:

$$\Omega_{RT} = \sqrt{\frac{2}{3\sqrt{3\sigma}} \frac{[g_t(\rho_d - \rho)]^{3/2}}{\rho_d + \rho}} \tag{3.13}$$

$$K_{RT} = \sqrt{\frac{g_t(\rho_d - \rho)}{3\sigma}} \tag{3.14}$$

$$g_t = (g + \frac{du_d}{dt}) \frac{u_d}{|u_d|} \tag{3.15}$$

$$\Lambda_{RT} = 2\pi C_{RT}/K_{RT} \tag{3.16}$$

If Λ_{RT} is smaller than the droplet diameter, the RT waves are assumed to grow on the surface. After the RT breakup time $\tau_{RT} = 1/\Omega_{RT}$ has elapsed, the droplet disintegrates into a collection of smaller droplets with diameter of Λ_{RT} [136]. C_{RT} is set to 0.1 [137] in this study. Likewise, the influence of the adjustable model constant C_{RT} will also be studied.

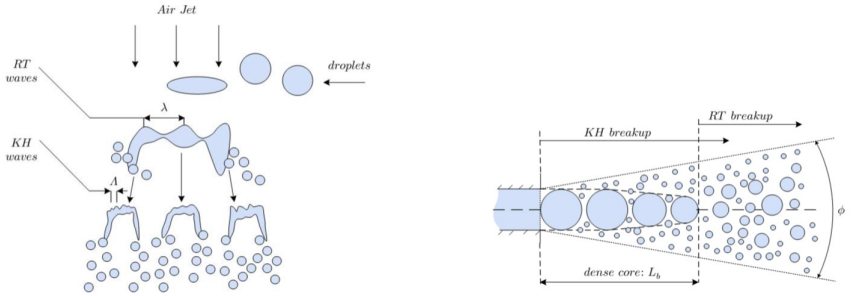

(a) Without (b) With

Figure 3.4: Illustrations about the combined KHRT model without/with breakup length concept [124]

As mentioned in Chapter 2, the combined KHRT model is widely used for diesel spray simulations. The incorporation of the breakup length concept [134], which

avoids the unphysical formation of too small droplets in the vicinity of the nozzle exit (see Figure 3.4), further improves the prediction accuracy of the combined KHRT model. Therefore, the KHRT breakup model with the breakup length concept was used for the computations in the present study.

Drag model

Due to the momentum exchange with the ambient gas, the droplet velocity is decreased. The drag force F_{drag} can be expressed in Eq. (3.17) by applying Newton's second law [106, 138]:

$$F_{\text{drag}} = m_d \frac{du_d}{dt} = -\frac{\pi D_d^2}{8} \rho C_d u_{rel}^2 \tag{3.17}$$

where m_d is the mass of the droplet, u_d is the velocity of the droplet, D_d is the diameter of the droplet, C_d is the drag coefficient. This drag coefficient is given by [139]

$$C_d = \begin{cases} \frac{24}{Re_d}\left(1 + \frac{1}{6} Re_d^{2/3}\right), & Re_d < 1000 \\ 0.424, & Re_d > 1000 \end{cases} \tag{3.18}$$

where the Reynolds number Re_d for a droplet is calculated through

$$Re_d = \frac{\rho u_{rel} D_d}{\mu} \tag{3.19}$$

In order to solve this motion equation, a momentum relaxation time τ_u is defined as

$$\tau_u = \frac{4}{3} \frac{\rho_d D_d}{\rho C_d u_{rel}}. \tag{3.20}$$

Evaporation model

When the liquid fuel is injected into a high-temperature combustion chamber, a mass change of the liquid droplets is caused by evaporation. Some assumptions are often made to model the droplet evaporation process:

- The radiative heat transfer is ignored as it is small compared to the convective heat transfer.
- The droplet interior is well mixed, i.e., the distribution of temperature, fuel concentration, and other relevant quantities is considered uniform.

- Droplet interactions, like deformation, breakup, collision, etc., do not influence the evaporation process.

The droplet evaporation rate is calculated from the equation [127, 138] given below:

$$\begin{aligned} \dot{m}_d = \frac{dm_d}{dt} &= -\pi D_d \mathcal{D} \rho_v Sh \ln \frac{p - p_{v,\infty}}{p - p_{v,s}} \\ &= -\pi D_d \mathcal{D} \rho_v Sh \ln(1 + B) \end{aligned} \tag{3.21}$$

$$B = \frac{p_{v,s} - p_{v,\infty}}{p - p_{v,s}} \tag{3.22}$$

where $\mathcal{D}$ is the mass diffusion coefficient [138], Sh the Sherwood number, p the total pressure of the gas mixture, $p_{v,s}$ and $p_{v,\infty}$ represent the partial fuel vapor pressure at the droplet surface and far from it. The fuel vapor density, ρ_v is evaluated from the ideal gas law

$$\rho_v = \frac{p}{R_v T_m} \tag{3.23}$$

where T_m denotes the mean temperature, and R_v stands for the fuel vapor gas constant.

The Sherwood number is calculated:

$$Sh = 2.0 + 0.6 Re_d^{1/2} Sc^{1/3} \tag{3.24}$$

where the Schmidt number Sc

$$Sc = \frac{\mu}{\rho \mathcal{D}} \tag{3.25}$$

The mass conservation equation is solved by using an evaporation relaxation time, τ_{evap}, defined as:

$$\tau_{\text{evap}} = \frac{m_d}{\pi D_d \mathcal{D} \rho_v Sh \ln(1 + B)} = \frac{\rho_d D_d^2}{6 \mathcal{D} \rho_v Sh \ln(1 + B)} \tag{3.26}$$

Droplet energy equation

The temperature change of the liquid droplet can be obtained from an energy balance [106]. The total heat rate $\dot{Q}_d$ transferred from the hot gas to the

liquid droplet results in an increase of droplet temperature (heating, $\dot{Q}_h$) and in evaporation ($\dot{Q}_{\text{evap}}$) [106, 127].

$$\dot{Q}_d = \dot{Q}_h + \dot{Q}_{\text{evap}} \tag{3.27}$$

$$\dot{Q}_h = m_d c_{p,l} \frac{dT_d}{dt} \tag{3.28}$$

$$\dot{Q}_{\text{evap}} = \Delta h_{\text{evap}} \frac{dm_d}{dt} \tag{3.29}$$

where $c_{p,l}$ is the specific heat capacity of the liquid droplet, T_d is the droplet temperature, and Δh_{evap} is the latent heat of the evaporation.

The rate of heat transfer between the gas and the droplet by convection $\dot{Q}_d$ is calculated as [140]:

$$\dot{Q}_d = \pi D_d k_h Nu f (T - T_d) \tag{3.30}$$

$$f = \frac{z}{e^z - 1} \tag{3.31}$$

$$z = -\frac{c_{p,v}\dot{m}_d}{\pi D_d k_h Nu} \tag{3.32}$$

where f is a factor which corrects the amount of heat exchange due the presence of mass transfer, $c_{p,v}$ is the fuel vapor specific heat at constant pressure, k_h the mixture thermal conductivity.

The Nusselt number is evaluated according to the Ranz-Marshall correlation [141, 142]:

$$Nu = 2.0 + 0.6 Re_d^{1/2} Pr^{1/3} \tag{3.33}$$

where Pr is the Prandtl number

$$Pr = \frac{c_p \mu}{k_h} \tag{3.34}$$

The heat transfer relaxation time is introduced to solve the energy equation:

$$\tau_h = \frac{m_d c_{p,l}}{\pi D_d k_h Nu} = \frac{\rho_d D_d^2 c_{p,l}}{6 k_h Nu} \tag{3.35}$$

3.2 Numerical methods

For the simulations, the OpenFOAM framework extended with the LibICE library, developed by the ICE group at Politecnico di Milano [143–146], was used.

OpenFOAM is short for Open Source Field Operation and Manipulation. An excerpt from its user guide [130] reads: "OpenFOAM is first and foremost a C++ library." The OpenFOAM solvers are designed to solve specified problems in continuum mechanics, and its utilities are for corresponding data manipulation, which involves simple pre- and post-processing tasks. Figure 3.5 shows the overall structure of OpenFOAM. A set of precompiled libraries are dynamically linked during the compilation of the utilities and solvers. An advantage of OpenFOAM is that new solvers and utilities can be implemented by the user with some relevant knowledge of physics and programming skills.

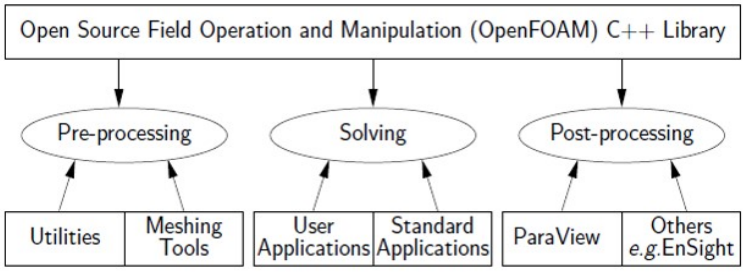

Figure 3.5: OpenFOAM structure overview [130]

LibICE is a set of libraries and solvers for ICE simulation (see Figure 3.6) based on the OpenFOAM platform. There are primarily three categories that LibICE has been working on:

- Mesh generation for CFD simulations. The motion of some engine components (e.g., valves and pistons) needs to be taken into account when modeling some processes in ICEs. A refinement strategy is also necessary for the near nozzle region of diesel sprays. Therefore, some techniques have been proposed and implemented, such as automatic mesh motion, adaptive local mesh refinement and spray-oriented mesh generation, to ensure mesh quality and save computational resources.
- In-cylinder process modeling. For example, advanced combustion models with detailed chemical kinetics are needed to better predict the ignition, flame propagation, and pollutant formation processes.

- Exhaust after-treatment modeling. The full-scale DPF simulation is used to optimize the DPF geometry accounting for flow non-uniformities.

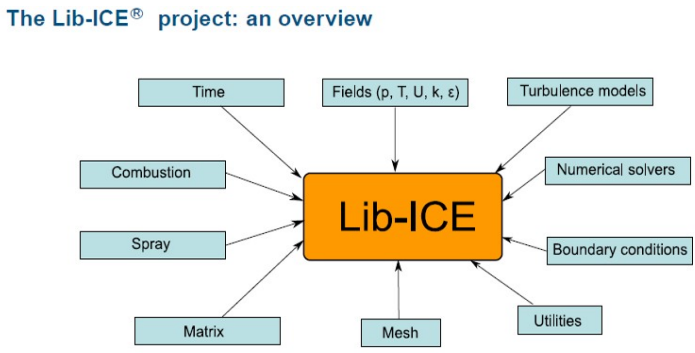

Figure 3.6: An overview of LibICE [147]

In the present study, the diesel spray is simplified as being axisymmetric (as shown in Figure 3.7(a)), which can save computational time. For this two-dimensional axisymmetric case in OpenFOAM, the geometry is specified as a wedge of small angle and one cell thick running along the symmetry plane, straddling one of the coordinate planes, as seen in Figure 3.7(b). In addition, many experimental studies [46, 56, 67, 148] also validate this axisymmetric simplification.

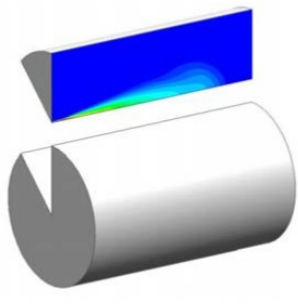

(a) Spray simplification [124]

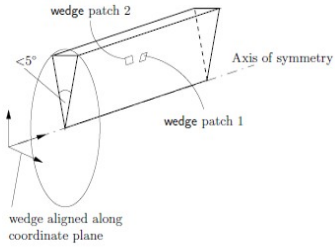

(b) Wedge type in OpenFOAM [130]

Figure 3.7: Diesel spray simplification for the present study

The detailed processes concerning discretization, EL coupling, and algorithms can be found in previous work [124, 127, 138, 149–151].

3.3 CFD results

In this section, the proposed models are first employed to simulate the ECN sprays. Then, the same methods are used for the GUCCI spray cases.

3.3.1 The ECN results

The vapor and liquid penetration measurement data are two parameters often used to validate the simulation models. The definitions employed to calculate the experimental vapor and liquid penetrations are recommended by the ECN. In simulations, the liquid penetration is defined as the axial distance from the injector where 95% of the liquid mass was found [152], and the vapor penetration is defined as the maximum distance of 0.1% fuel mass fraction. This simulation data, liquid and vapor penetration as a function of time, is generated and stored in a data file by implementing the definition above in the code.

Figure 3.8 presents the comparison of the computed results against experimental data in terms of spray (vapor and liquid phase) penetration. While the vapor penetration is found to be slightly lower than the measurement, the liquid penetration fits the experimental data well.

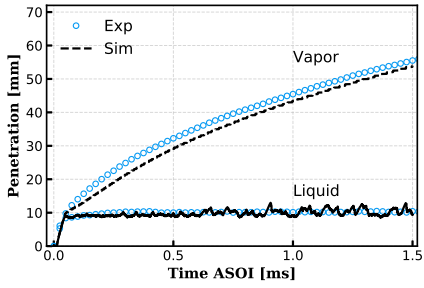

Figure 3.8: Comparison of liquid length and vapor penetration of case SA

As introduced in Dec's conceptual model in Chapter 2, the evaporating diesel sprays are mixing-controlled, which means the local combustion rate is determined by the local mixing rate (or the local mixture fraction). Moreover, the mixing process also influences the autoignition of the premixed fuel/air mixture. Thus, the mixture fraction distribution, which represents the mixing process in diesel sprays, is also used to validate the computed results. Figure 3.9 shows the radial distributions of mixture fraction at 25 mm and 40 mm downstream of the injector.

The computed mixture profile is the time-averaged value (1.0 ms - 1.5 ms ASOI time interval). This period is chosen because the upstream part of the spray has reached the statistical steady state [116, 153]. From the comparison with the Spray A (SA) case, the employed models can be concluded to be capable of reproducing the spray penetration and mixture formation processes in diesel engines.

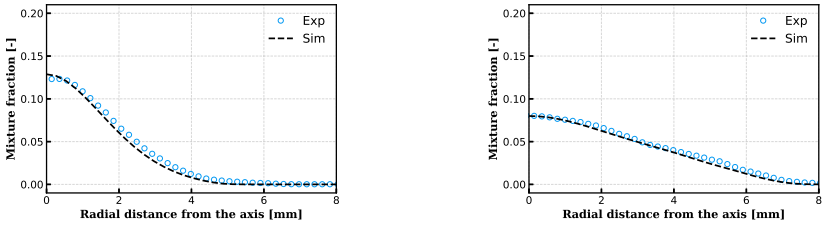

(a) 25 mm (b) 40 mm

Figure 3.9: Mixture fraction at different locations of the SA case.

In addition, the simulation results of the SA case also indicate that the accurate predictions of the global quantities (e.g., vapor and liquid penetrations) are the prerequisite for the agreement on local ones (e.g., mixture fraction). This is important because, for diesel sprays, the measurement of the local fuel-air mixture is more difficult than the measurement of the spray penetration [67].

Mesh sensitivity

Table 3.1: Tested meshes summary

Mesh	Radial direction		Axial direction	
	Number of cells	Refine ratio	Number of cells	Refine ratio
M0	108	0.1	216	0.5
M1	54	0.1	216	0.5
M2	162	0.1	216	0.5
M3	108	0.1	162	0.5
M4	108	0.1	270	0.5

The mesh quality is very important for trustworthy simulation results. Previous studies [119, 145] have drawn the following conclusions considering the influence of the mesh on the CFD results:

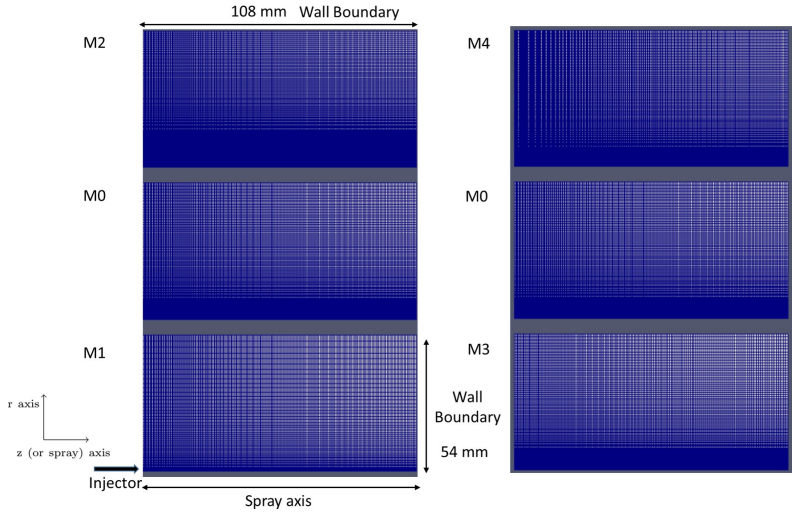

Figure 3.10: Different mesh configurations use for mesh sensitivity study. The meshes on the left show the variation in radial direction; the meshes on the right show the variation in axial direction.

- The vapor penetration is less sensitive to the cell size compared to the liquid phase penetration;
- The cell size on the radial direction has more evident influence on the liquid penetration;
- A coarse mesh, due to the incorrect description of liquid and gas interaction, underestimates the liquid penetration, while an excessively refined mesh (that would violate the EL approach assumptions [154]) results in the overestimation because of the unphysically fast diffusion of momentum from the liquid to the gas phase.

The mesh handling for the case SA and SD has been studied by many researchers [69, 71, 155] within the ECN community. Based on their experience, the meshes need to be refined progressively close to the nozzle because of the relatively smaller nozzle diameter of case SA and SD. This is because the spray process mainly occurs near the region close to the spray axis, as demonstrated in the experimental and numerical literature [67, 69, 71]. In order to better predict the spray behavior, the mesh near the axis region should be refined. This type of mesh can also save computational expense compared to the uniformly refined mesh. On the other hand, as mentioned earlier, the mesh size cannot be smaller than the droplet size; otherwise, it would violate the EL approach assumptions.

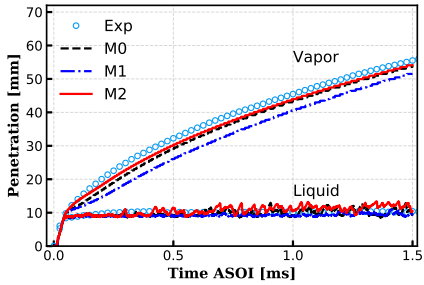

(a) Radial direction

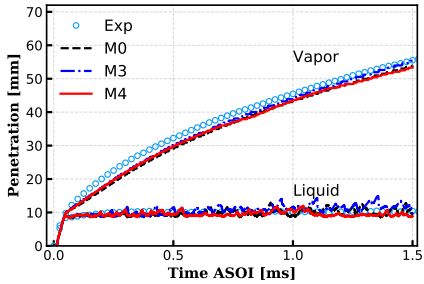

(b) Axial direction

Figure 3.11: The influence of the mesh on the CFD result. The top image (a) shows the results from a different mesh quality in the radial direction, while the bottom image (b) shows the results from a different mesh quality in the axial direction.

A mesh sensitivity study was performed in order to check the mesh quality. Meshes used for the sensitivity study are shown in Figure 3.10, in which the left-hand column presents the difference in the radial direction, and the right-hand column presents the difference in the axial direction. When the radial direction mesh is varying for comparison, the mesh on the axial mesh is kept unchanged, and vice versa. Table 3.1 gives some detailed mesh parameters. Figure 3.11 compares the effect of axial and radial direction mesh quality on the simulation results. It can be seen from Figure 3.11(a) that the coarse mesh (M1) underestimates the vapor penetration. The obtained results are generally consistent with the conclusions from the literature mentioned above. The mesh M0 is chosen for further simulations because the mesh sensitivity study demonstrates that this mesh is capable of capturing the spray characteristics under the ECN Spray A conditions.

A comparative study of turbulence models

As discussed in Chapter 2, the standard $k-\varepsilon$ and RNG $k-\varepsilon$ model are often used for diesel spray simulations. This section compares the performance of the standard and RNG model, clarifying the reason for using the former one in this work. As shown in Figure 3.12, the RNG model underestimates the vapor penetration after about 0.2 ms ASOI and overestimates the liquid penetration after about 0.9 ms ASOI. This comparison is also consistent with other researchers [68, 69, 119] using OpenFOAM for diesel spray simulations.

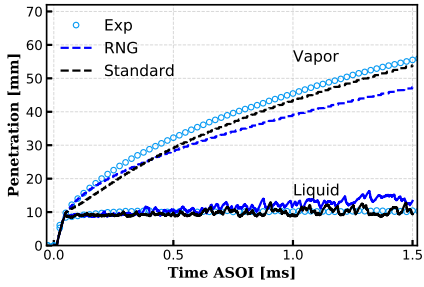

Figure 3.12: Comparison between the RNG and standard $k-\varepsilon$ model

A parametric study of the breakup model

In this section, the function of the breakup length concept is investigated. The penetration plots in Figure 3.13 show that an evident overestimation of liquid penetration is obtained for the simulation case when not accounting for the breakup length. It should also be noted that this case also underestimates the vapor penetration at the near nozzle region. To understand its effect, the left-hand column of Figure 3.14 shows the scatter plots of the droplet size distribution along the spray axis, while figures on the right-hand column show the scatter plots of the droplet velocity distribution.

As discussed in subsection 3.1.2, the blob model is used for the spray injection, and the figures show that the droplet diameter at the injector nozzle exit is equal to the nozzle hole diameter. For an approximate distance contained within the first 15 mm (i.e., $\in [0,15]$ mm), both figures show the existence of extremely small ($< 10\mu$m) droplets, which are due to the breakup of the bigger droplets upstream and their transportation downstream [156]. Both cases predict the diameter reduction due to breakup and evaporation for the near nozzle region [156]

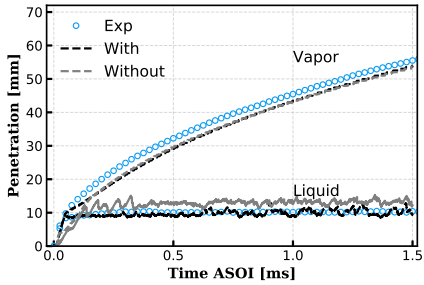

Figure 3.13: Effect of the breakup length concept on the CFD result

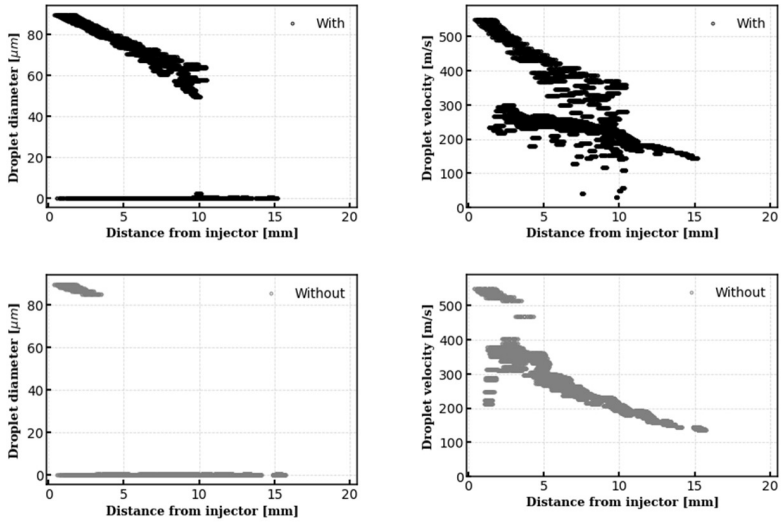

Figure 3.14: Scatter plots of the droplet size and droplet velocity distributions. The abscissa axis for all the plots is the axial distance from the injector. The left-hand column's ordinate axis is the droplet diameter, for the right-hand column it is the droplet velocity. The upper row shows the simulation results considering breakup length, while the lower row represents the results without breakup length. The data around 0 in the droplet diameter figure represent the small droplets produced during the breakup process.

(distance $\in [0,4]$ mm). However, the case incorporating the breakup length concept also produces droplets with moderate size (40μm < D_d < 80μm) at a distance between 4 and 10 mm downstream. These moderate-sized droplets are created by the KH mechanism within the breakup length. As mentioned previously, the RT mechanism is characterized by a fast disintegration that produces a collection of small droplets [106, 134]. The droplet velocity distribution plots on the right-hand side also show that the case without breakup length predicts lower droplet velocity,

thus lower relative velocity between the droplets and the gas phase, reducing the droplets' evaporation rates. These droplets that evaporate slowly probably result in the higher liquid penetration length depicted in Figure 3.13.

In the KH and RT mechanisms, the adjustable model constant B_1 in Eq. (3.12) and C_{RT} in Eq. (3.16) are known to impact the CFD predictions [104, 136]. Different values were used for the simulation to investigate their influence. Although Baumgarten [106] proposed a value range between 1.6 and 60 for B_1, and 1.0 ~ 5.33 for C_{RT}, researchers [107, 157] still determined these values through the calibration of penetration measurements.

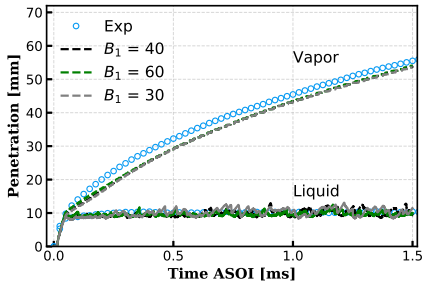

Figure 3.15: Effect of the value of B_1 on the CFD result

Figure 3.15 compares the vapor and liquid penetrations from cases with different B_1 values. The results almost overlap, indicating that the impact of this model constant is minimal. Likewise, Figure 3.16 shows the droplet diameter and velocity distributions. Similarly, a negligible influence can be observed on the droplet velocity distribution. Differences, however, can be seen from the droplet diameter distributions. The plots on the left of Figure 3.16 show that a lower value of B_1 leads to a faster reduction of the droplet diameter within the distance ranging from 0 to about 10 mm downstream from the injector. According to the definition of the KH breakup time scale (Eq. (3.12)), a lower value leads to an increased liquid phase disintegration. In contrast, a higher value results in a reduced breakup. From the results shown here, this effect impacts the droplets within the breakup length. According to Brulatout et al. [157], when a relatively low value (e.g., 0.1) is used for C_{RT}, the RT mechanism dominates the breakup process, which is another possible reason for the negligible effect of B_1 on the CFD results discussed here.

Unlike B_1, the value of C_{RT} has a noticeable effect on the CFD prediction. A higher value results in a higher liquid penetration, but this value has a negligible effect on vapor penetration, which is consistent with Patterson et al. [136]. This is because a higher value produces larger child droplets by the RT mechanism according to Eq.

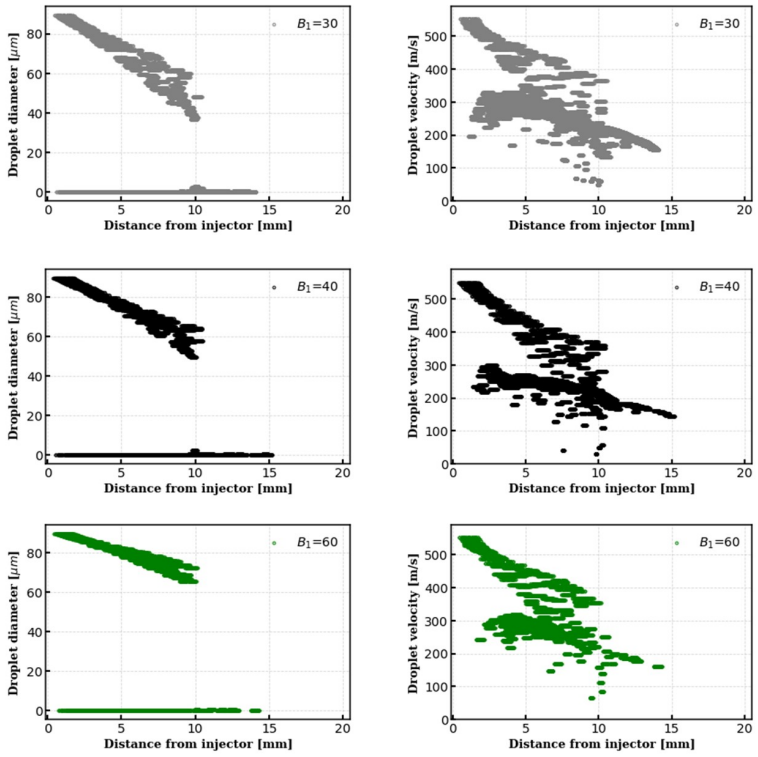

Figure 3.16: The effect of the KH model constant B_1 on the droplet diameter distribution and the droplet velocity distribution. The left column shows the droplet diameter distribution of different B_1 values, while the right column represents the droplet velocity distribution.

(3.16). Figure 3.18 also shows this value has an impact on the droplet diameter and velocity distributions. The droplet diameter distributions show that many moderate-size droplets are created at a distance beyond approximately 10 mm, indicating that the RT breakup mainly occurs on the droplets in the region far from the injector. Due to the relatively large size, these moderate-size droplets have a long evaporation time, which causes the high liquid penetration length shown in Figure 3.17.

The mesh sensitivity study and model parameter study lay a foundation for the simulations in the following parts. The same computational models are then employed for the SD case, in which the nozzle hole diameter is about twice that of the SA case. Figure 3.19(a) illustrates the mesh used for the SD case. It can be observed in Figure 3.19(b) that there is generally good agreement between simulations and measurements.

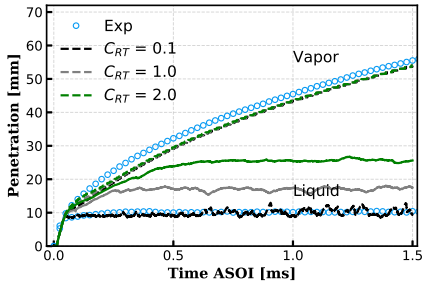

Figure 3.17: Effect of the value of C_{RT} on CFD result

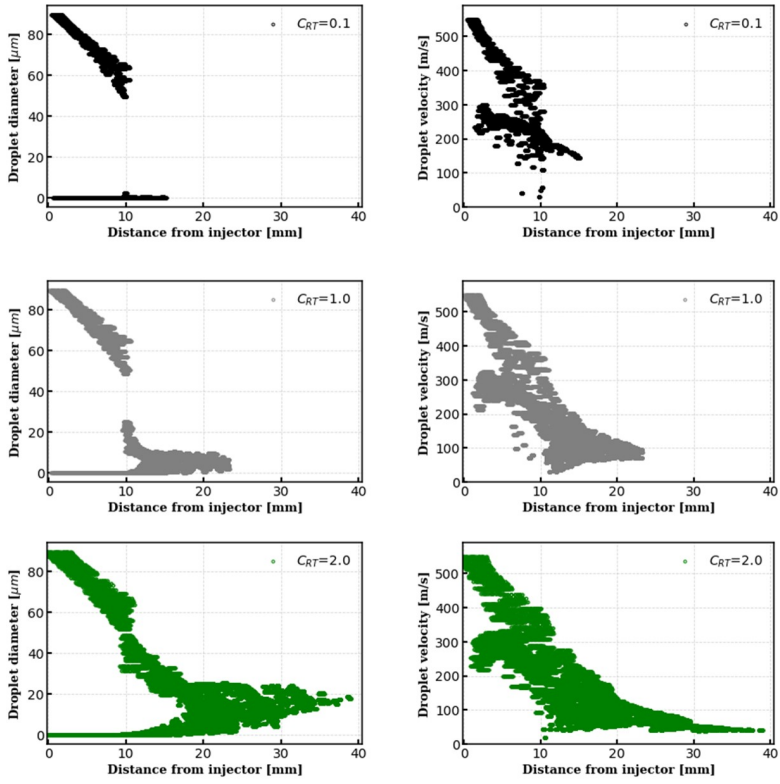

Figure 3.18: The effect of the RT model constant C_{RT} on droplet diameter distribution and droplet velocity distribution. The left column shows the droplet diameter distribution of different C_{RT} values, while the right column represents the droplet velocity distribution.

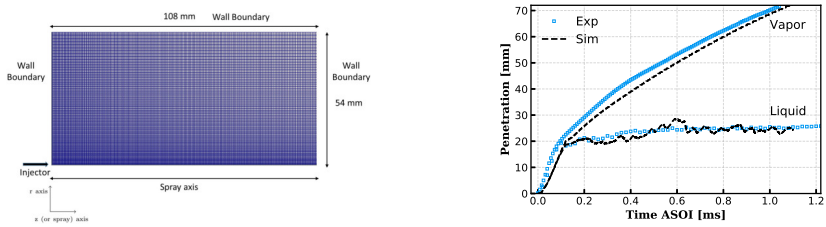

(a) Mesh of Spray D case

(b) Penetration comparison

Figure 3.19: Mesh and CFD result for Spray D

The success of the proposed approach in predictions of the measured data for the ECN cases is encouraging, and suggests that the sub-models have the potential for accurately predicting spray processes in diesel engines. Therefore, the same approach is used in the next section, to simulate the marine engine sprays.

3.3.2 The GUCCI results

Preliminary results

The simulations for the GUCCI Spray (GS) Case4 were first performed, due to its ambient conditions being similar to the SA and SD cases.

The computational mesh used for the GS cases is displayed in Figure 3.20. A uniform mesh is used with a relatively larger cell size in comparison to the simulations of the SA and SD cases. There are two reasons: 1) The cell size should be larger than the liquid drop size, which follows the assumptions of the EL approach [154]; 2) The nozzle hole diameter of marine engines is often larger than the one used in automotive or HD engines. As shown in Table 2.2, the nozzle diameter of the GS cases is about 5 times that of the SA case, and twice that of the SD case. Therefore, the smallest mesh size for the GS case should be larger than about 0.6 mm. This mesh size does not need high computational expense compared to the ECN cases. Accounting for these factors, the mesh shown in Figure 3.20 is proposed. The corresponding mesh sensitivity study will be conducted in the following.

Figure 3.21 shows that both the computed vapor and liquid penetrations differ from the measurement: for example, at 4.0 ms ASOI the vapor and liquid penetration from the CFD are overestimating the measured ones by 18% and 58%,

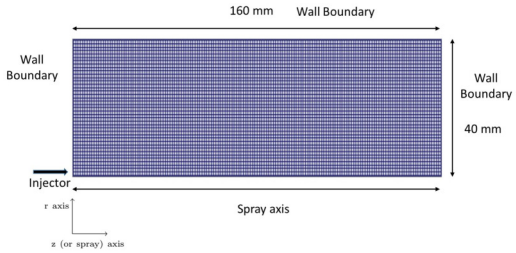

Figure 3.20: The mesh and boundary conditions used for the GS case

respectively. The influence of the mesh on the CFD results is first investigated. Figure 3.22 compares the effect of the axial and radial cell size on the computed results. The results obtained here are consistent with the mesh sensitivity study conducted for the SA case and previous studies [119, 145]. In addition, the mesh sensitivity study also indicates the mesh quality chosen is capable of describing the spray process, and the discrepancy is not caused by the mesh.

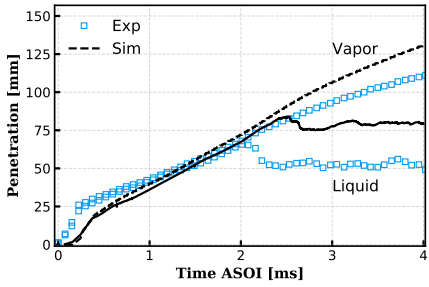

Figure 3.21: Comparison of liquid length and vapor penetration of GS Case4

Similarly, different values for the breakup model are tested to seek improvement. As shown in Figure 3.23, the impact of these adjustable model constants is almost identical for this case compared to the SA case:

- B_1 has a negligible effect on the simulation.
- An increased value of C_{RT} leads to higher liquid penetrations.
- Both of these constants have a slight impact on the vapor penetration.

The effect of the turbulence model coefficients on spray and combustion characteristics has been investigated extensively [68, 70, 72, 119, 158]. These

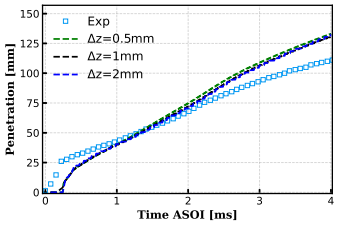

(a) Effect of axial size on vapor phase

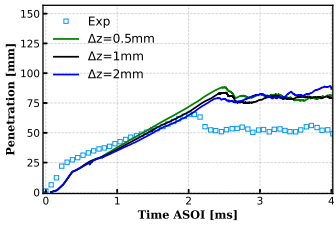

(b) Effect of axial size on liquid phase

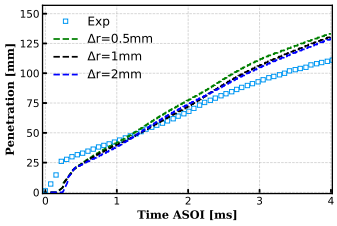

(c) Effect of radial size on vapor phase

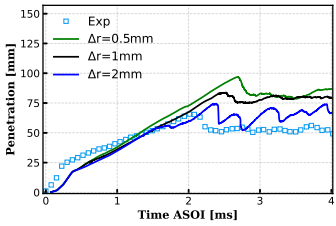

(d) Effect of radial size on liquid phase

Figure 3.22: Effect of cell size on spray penetration for GS Case4

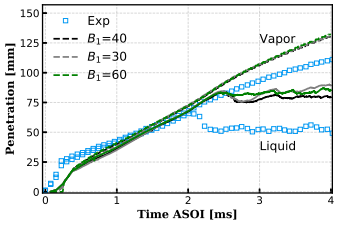

(a) The result of different B_1 value

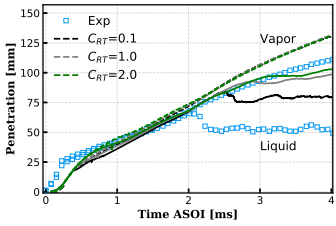

(b) The result of different C_{RT} value

Figure 3.23: Simulation results by varying breakup model constants

authors found that the value of C_1 of the standard $k-\varepsilon$ turbulence model is very important. A correct estimation of this value is necessary to predict the spray development and fuel-air mixing process [158]. Table 3.2 summarizes the values of C_1 used in diesel spray simulations and their injection conditions. Figure 3.24 (a) and (b) are the scatter plots of the relation between the value of C_1 and the nozzle hole diameter and injection velocity, respectively. Although an exact function is difficult to obtain, the general trend is that the value of C_1 should decrease as the nozzle hole diameter increases and the injection velocity drops.

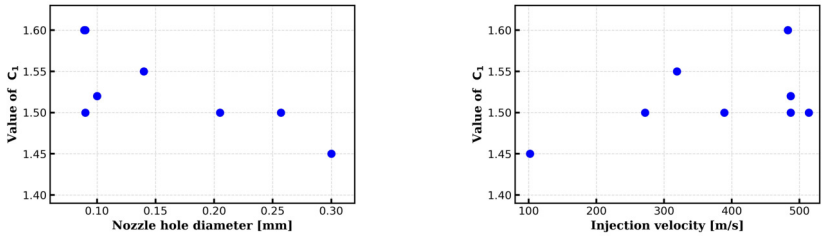

(a) Nozzle hole diameter (b) Injection velocity

Figure 3.24: Scatter plots of C_1 with nozzle hole diameter and injection velocity. As shown in the figures, for high injection velocity and small nozzle conditions, different values of C_1 (i.e., 1.50 and 1.60) were used by different researchers.

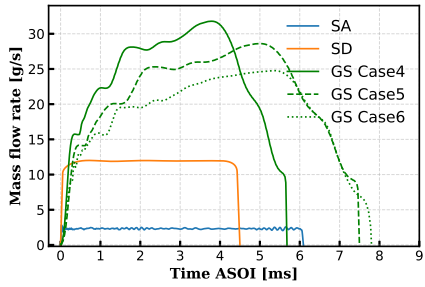

(a) Mass flow rate

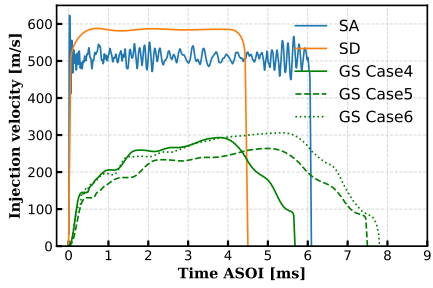

(b) Injection velocity

Figure 3.25: Mass flow rate and injection velocity for each case. The green dashed lines represent GS Case5, the green dotted lines represent GS Case 6, and the green solid lines represent other GS cases.

Table 3.2: The value of C_1 used for spray simulations. Different CFD codes, including commercial and open-source codes, were used by different researchers.

Value of C_1	Nozzle diameter [mm]	Injection velocity [m/s]	Refs
1.45	0.300	102	[131]
1.50	0.205	514	[158]
1.50	0.257	272	[119]
1.50	0.257	389	[119]
1.50	0.090	487	[71]
1.52	0.100	487	[68, 72]
1.55	0.140	319	[119]
1.60	0.089	483	[70, 73, 159]

Figure 3.25 gives the injection profile for each case. It is clear from Figure 3.25(b) that the injection velocity for marine engines is low compared to that of the ECN cases. Given the trends in Figure 3.24, the value of C_1 is then set to a lower value of 1.45.[6] The simulation results with a lower value of C_1 displayed in Figure 3.26 show a good agreement between simulation and measurement.

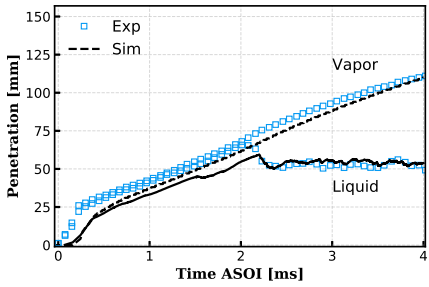

Figure 3.26: Comparison of liquid length and vapor penetration of GS Case4 with C_1 = 1.45

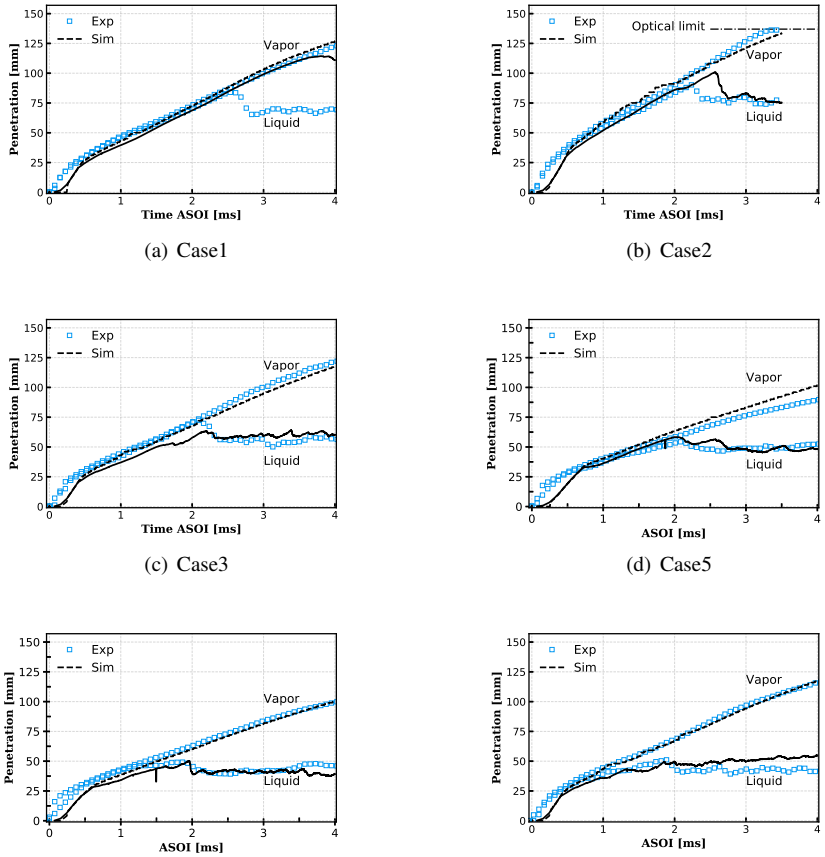

(a) Case1 (b) Case2

(c) Case3 (d) Case5

(e) Case6 (f) Case7

Figure 3.27: Spray penetration comparison of other GS cases

Analysis of the other GS cases

The results of the other GS cases are shown in Figure 3.27. The plots show that there is good agreement between the output of the simulations and the measurements. However, it can be noted that for the low temperature case (Case1, ambient temperature 700 K), the liquid penetration obtained from the simulations is much higher than the measured value, although the simulations predict the vapor penetration correctly.

[6] The sensitivity analysis of other turbulence model constants is performed (see Appendix C), and the results show that these constants have a negligible effect on the CFD results.

The contour plots in Figure 3.28 show the mixture fraction and droplet diameter distribution from 2.5 ms to 4.0 ms, for this GS Case1 where the CFD results disagree with the measurement. It can be seen that there is a locally high fraction of fuel at the spray tip (pointed out by the white arrow in the contour plots of Figure 3.28), while the droplet size and droplet number at these locations are small. It should be noted that the size of the dark droplets on the spray tip is quite small ($< 10\mu$m), and the vapor fuel concentration at the same location is relatively high, as illustrated by the red color. As the spray continues to penetrate, for example, at 3.5 and 4.0 ms, the droplet number at the tip reduces, but the high concentration region still exists. This locally high concentration could be due to the evaporation of a detached ligament.

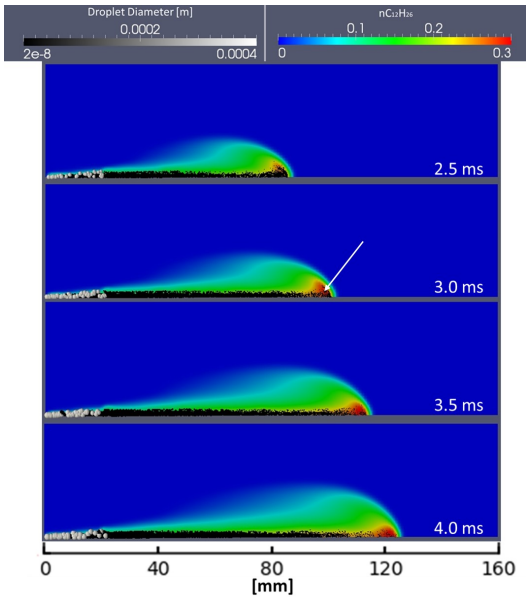

Figure 3.28: Contour plots of GS Case1. The black color represents the small droplets, and the grey color represents the large droplets. The blue color represents low vapor fuel concentration, and the red color represents high concentration. The white arrow points to the detached droplets.

Maes et al. [158] used high-speed DBI imaging for the liquid penetration and also found this ligaments detachment, which mainly results in the fluctuations in liquid penetration. The liquid penetration images that followed the time sequence are shown in Figure 3.29. Two large eddies with white brackets in the right plane of Figure 3.29 are the ligaments that eventually detach. These images also illustrate that the detaching ligaments have a size that is approximately the same as the eddies at the main liquid core's periphery.

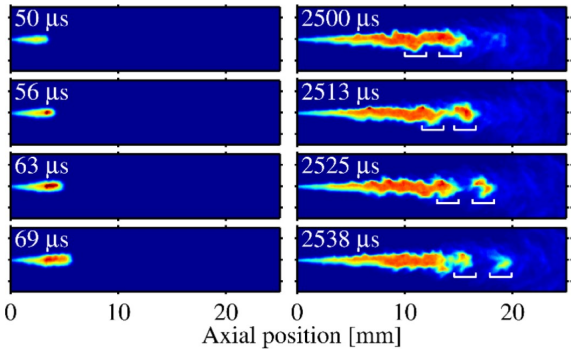

Figure 3.29: The DBI images from Maes et al. [158]

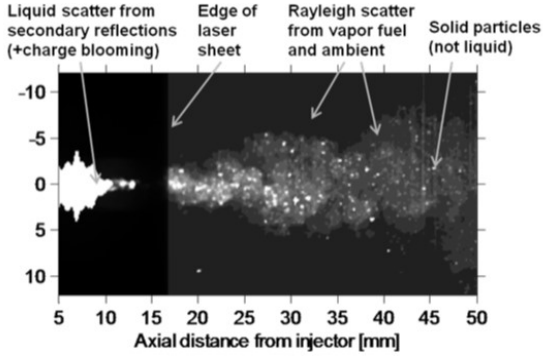

Figure 3.30: The Rayleigh diagnostic from Pickett et al. [160]

Pickett et al. [160] found these 'residual liquid droplets' accidentally when performing the Rayleigh scattering diagnostic for a quantitative vapor-fuel/air mixing [67]. As shown in Figure 3.30, from 5 - 10 mm downstream of the injector, the intense signal by charge blooming is due to the scatter from large liquid droplets. Note that this high-intensity region is defined as the liquid length by the Mie-scattering technique. From about 10 - 15 mm, scatter, which is not saturated, is also detected by the Rayleigh diagnostic. After suitable analysis, this relatively low-intensity scatter was proven to be caused by very low droplet concentrations.

From Figure 3.28, at 4.0 ms ASOI the detached ligaments and the main liquid core can be clearly observed. Thus, a possible explanation for this disagreement is that the Mie-scattering technique employed in the GS measurement did not capture this ligament detachment due to the droplet number at the spray tip being sparse and the fast evaporation there.

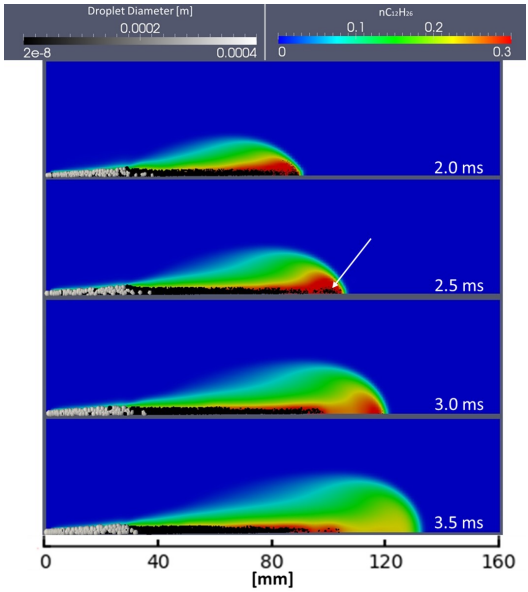

Figure 3.31: Contour plots of GS Case2. The black color represents the small droplets, and the grey color represents the large droplets. The blue color represents low vapor fuel concentration, and the red color represents high concentration. The white arrow points to the detached droplets.

The same ligaments detachment phenomenon is also found under low density conditions (GS Case2). Similarly, from 2.5 ms ASOI, a small group of droplets (pointed at by the white arrow in the contour plots of Figure 3.31) detached from the main liquid core, which might explain the overestimation of liquid penetration from 2.0 ms to 2.5 ms in Figure 3.27(b). At 3.0 ms, the evaporation of these droplets results in the locally high concentration of vapor fuel at the spray tip, as illustrated in the contour plots. Compared to GS Case1, the ligaments detachment occurs earlier, and the evaporation is also faster, which could be attributed to the higher ambient temperature of GS Case2.

It should be noted that the simulated vapor and liquid penetrations before 0.4 ms ASOI underestimate the measurements. Some researchers [107, 108, 157] have also found this similar phenomenon. The main reason for this underestimation is supposed to be that the spray penetration behavior in the near nozzle region is closely related to the flow dynamics inside the nozzle hole, according to the published literature [112, 161, 162]. Therefore, both experimental and numerical, future work is needed in order to obtain a good prediction for all the regions.

3.3.3 Exploration of the modeling difference

The influence of the C_1 coefficient on different diesel sprays is now investigated, as shown in Figure 3.32. Generally, the influence on vapor penetration is obvious for all test cases, including the GS Case4. However, as the nozzle diameter increases, the influence on the liquid penetration becomes more pronounced. The liquid penetrations for the SA case almost collapse, which is consistent with the CFD results by Novella et al. [68] and Wei et al. [72], while for the case SD and GS Case4 it is clear that a higher C_1 value also results in higher liquid penetration. Figure 3.33, which also includes the results from Maes et al. [158], plots the relationship between the value of C_1 and the computed liquid length. These results prove the observation mentioned above that the effect of C_1 becomes notable with an increasing nozzle diameter and lower injection velocity.

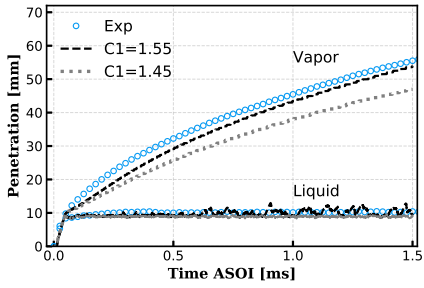

(a) Spray A

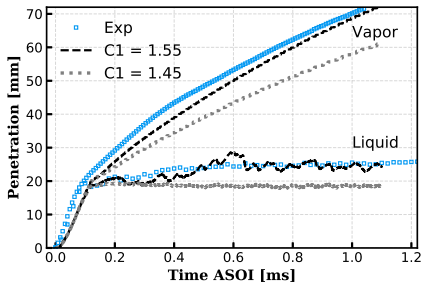

(b) Spray D

Figure 3.32: Computed penetration results from $C_1 = 1.45$ *and* $C_1 = 1.55$

Due to the non-linear nature of the turbulent flow, the effect of C_1 on spray development is difficult to deduce only based on the governing equations (Eqs. (3.7) and (3.8)). To further investigate the detailed effect of C_1, the case SA, which

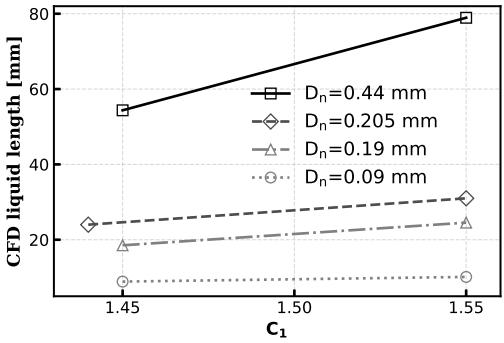

Figure 3.33: The relationship between C_1 and the CFD liquid length. The result of D_n = 0.205 mm is from Ref.[158]

is also the baseline case of ECN, has been used for further study. Figure 3.34 compares the mixture fraction distribution at two different positions downstream of the injector, and Figure 3.35 demonstrates the radial velocity at these positions. The results obtained show that a lower value of C_1 leads to a higher spreading rate and wider radial profile, thus lower penetrations, which is consistent with the conclusions in Refs. [68, 119, 159, 163].

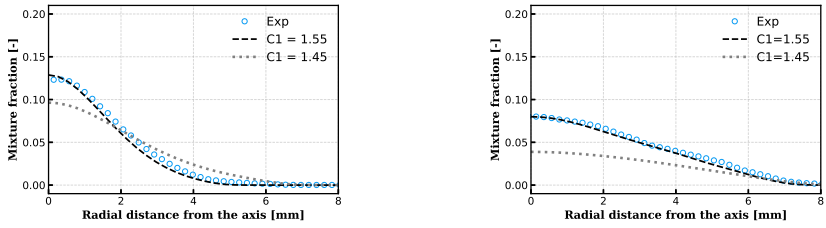

(a) 25 mm (b) 40 mm

Figure 3.34: Comparisons of mixture fraction at different locations

Dec's conceptual model and the "mixing-controlled" concept are concluded to the following sentence by Musculus et al. [52]:

> "For high-pressure diesel injection, vaporization is limited by mixing (i.e., entrainment), not by droplet atomization and vaporization processes."

This summary also supports the simulation research on evaporating diesel sprays

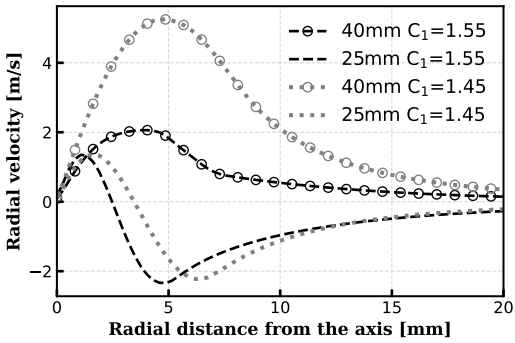

Figure 3.35: Radial velocity at two positions. The positive value represents the expansion motion, while a negative value means surrounding gas is entrained.

in this chapter. The turbulence model, which controls the mixing process, causes the disagreement between the measurement and simulation. Compared to the influence of the turbulence model, the effect of the atomization (or breakup) model is not significant, which is consistent with the summary by Musculus et al. [52].

3.4 Closure

Evaporating spray simulations, under medium speed marine engine-like conditions, were performed using OpenFOAM and Lib-ICE multi-dimensional CFD frameworks. The computational model was validated by a series of evaporating spray experiments with different ambient gas densities (7.6-22.5 kg/m^3) and temperatures (700-950 K).

- The spray sub-models, used for automotive engine sprays, are capable of predicting the fuel injection, breakup, and evaporation processes in the medium speed marine engines, while the model coefficient C_1 in the standard $k-\varepsilon$ turbulence model should be lower.
- The influence of C_1 on the spray development becomes notable with an increasing nozzle diameter. A lower value of C_1 leads to higher radial expanding rates, and thus reduces the spray penetration. Based on the conclusions from literature and the simulation results in the present work, the diesel sprays for marine engines studied in this work have a higher spreading rate than the diesel sprays in heavy-duty engines.

- The disagreement between some of the computed and measured liquid penetration could be caused by the ligaments detachment phenomenon. At low ambient density condition (7.6 kg/m^3), this phenomenon can be observed clearly from the CFD simulations. According to the published literature, the reasons for the phenomenon are not conclusive, and need further study.
- The spray behavior in the near nozzle region is not well captured by the CFD simulation, providing direction for future work on near nozzle region research both numerically and experimentally.

4

Empirical diesel spray penetration modeling

As mentioned earlier, in DI diesel engines, spray penetration is an important parameter for mixture formation. Due to its simplicity, the empirical spray penetration model is used in engine simulation tools (e.g., GT power) to help with engine design and optimization. This chapter focuses on the modeling of spray penetration. Section 4.1 first introduces the development background of the empirical spray penetration modeling. Two widely used models are presented. Section 4.2.1 gives the penetration results predicted by these two models, showing that the performance of the two-stage model is better. Considering the injection characteristics of the marine engine studied in this Ph.D., improvements are proposed to obtain a better description of the spray penetration behavior. Finally, section 4.2.2 explores the spray density distribution following the approach in the literature and discusses the model of Pozorski based on the results obtained in this work.

4.1 Introduction

The transient tip penetration of a diesel fuel spray is a parameter often measured. The injected fuel that penetrates the combustion chamber has an important influence on air utilization and fuel-air mixing rates, which is key for engine performance optimization. The spray tip penetration is a function of the time after injection (see Figure 4.1), which can be described in an empirical spray model.

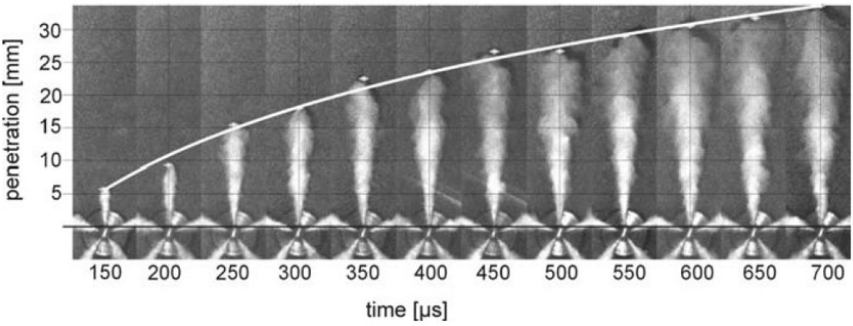

Figure 4.1: Spray development during injection [164]. P_{inj}=70 MPa, P_{amb} = 5 MPa, T_g = 890 K

In ICEs, the distance between the injector nozzle and the combustion chamber wall limits the penetration length. In some engine designs, fuel impingement on the wall is desired due to the hot wall and high air swirl. However, in multi-spray DI diesel combustion engines, over-penetration may result in the formation of a liquid film on the chamber wall, which increases emissions of partially burned or unburned products. On the other hand, under-penetration causes insufficient air utilization because the air further downstream has no contact with the fuel.

Numerous optical experiments and empirical models about diesel spray behavior under conditions typical of diesel engines have been extensively studied. Two empirical penetration models[1] have been widely cited in textbooks (e.g., [1, 51, 165–167]), one by Dent [168] and one by Hiroyasu and Arai [86].

In the model proposed by Dent [168], shown in Eq. (4.1), which includes the effect of ambient gas temperature (T_g), the spray penetration is expressed as:

$$S(t) = 3.07\left(\frac{\Delta P}{\rho_g}\right)^{0.25}\left(D_n t\right)^{0.5}\left(\frac{294}{T_g}\right)^{0.25} \tag{4.1}$$

[1] Detailed derivation of the empirical penetration models is given the Appendix D.

where $\Delta P = P_{inj} - P_{amb}$ in [Pa] is the difference between the injection pressure and the ambient gas pressure, ρ_g is the ambient gas density in [kg/m^3], D_n is the nozzle hole diameter in [m] and t in [s] is the time after the start of injection. Note, ρ_g is a constant value, which is different from the gas phase density in Chapter 3. This also applies to the symbols (e.g., T_g, ρ_l) in the following content of this chapter.

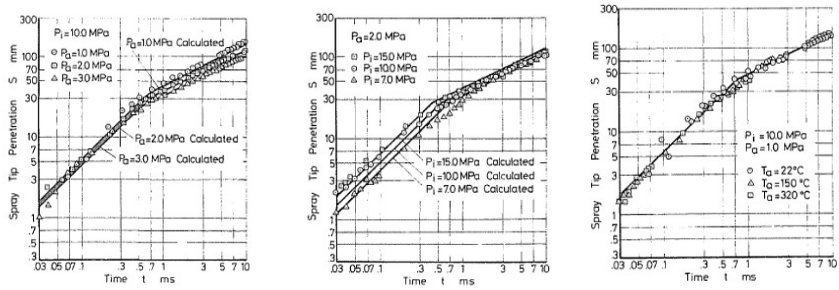

(a) Various ambient gas pressure (b) Various injection pressure (c) Various ambient temperature

Figure 4.2: Spray penetration at various conditions measured by Arai et al. [169]

Arai et al. [169] studied the disintegration process and the characteristics of diesel fuel oil at various conditions, including ambient pressure, injection pressure, and ambient temperature in a constant volume bomb. The results are shown in Figure 4.2, where the spray penetration is plotted in logarithmic scale on the ordinate and the logarithmic time is plotted on the abscissa. These data clearly illustrate that there are two different linear relationship slopes between the logarithmic penetration and time. The slope in the initial stage is 1, but after that, the slope becomes 0.5. In other words, the spray penetration is first proportional to time and after a specific period time it is proportional to the square root of time.

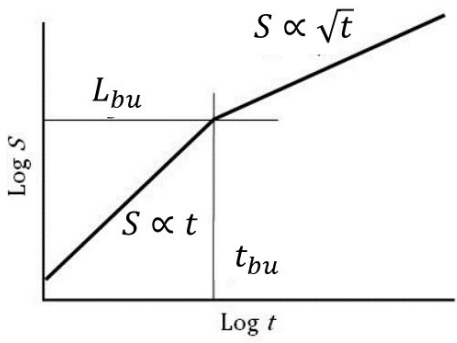

Figure 4.3: Schematic diagram of the two-stage empirical penetration model [169, 170]

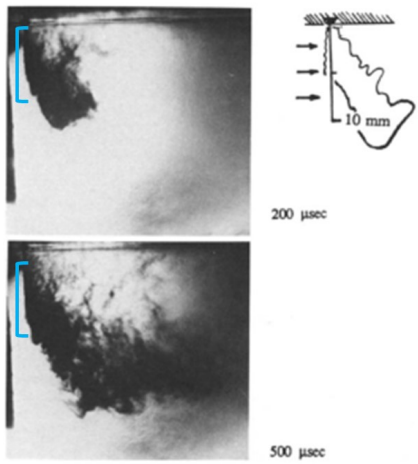

Figure 4.4: Shadowgraphs of spray experiments by Yule et al. [171]. The cross wind direction is from left to right. The blue brackets indicate the breakup region.

Figure 4.3 is the schematic diagram of the two-stage empirical penetration model proposed by Arai et al. [169]. As Arai et al. [169] interpreted, before the breakup time, the liquid fuel jet does not finish its atomization and can still be seen as the unbroken liquid. Therefore the liquid fuel penetrates with a constant velocity. After the breakup time (t_{bu}), the spray develops into a steady jet, as a result of momentum exchange with the ambient gas, which can be explained by the model of Dent [168]. Thus, the spray penetration is proportional to the square root of time. The breakup time and breakup length (L_{bu}) were considered in the further work of Hiroyasu and Arai [86], where they suggest that only in the breakup zone, an approximately linear relationship between spray penetration S and time t should exist.

Although the full understanding of the spray structure within the breakup length is incomplete, it is now commonly accepted that the column of fuel, emerging from an injector, may require a distance or liquid core to atomize fully, that has the same order of magnitude as the nozzle diameter.

To calculate the breakup length, Yule et al. [171] designed experiments with a cross wind to blow off the spray droplets. Figure 4.4 shows diagrammatically the spray injected from a 0.265 mm nozzle into gas with a pressure of 2.5 MPa and temperature of 290 K with a cross flow velocity of 40 m/s. At 200 μs, the spray exhibits a slight deviation. At 500 μs, the droplets detached from the main central body and moved with the cross flow, revealing the breakup zone.

Recently, Crua et al. [172, 173] captured the spray images in the initial stage with high spatial and temporal resolutions (frame rates up to 5 million images per second). Figure 4.5(a) shows the diesel spray evolution at high temperature (540 K) and high pressure (4 MPa) conditions with an injection pressure of 40 MPa. To better capture the spray behavior at the initial stage, Crua et al. conducted measurements at atmospheric conditions (Figure 4.5(b)) because the liquid evaporation could blur the images. It is seen that a coherent liquid diesel jet is emerging from the nozzle, with small droplets being stripped from the jet.

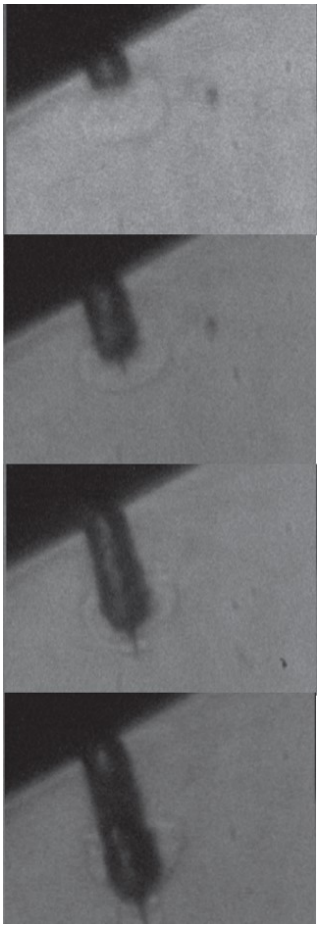

(a) Injection pressure is 40 MPa; gas pressure is 4 MPa; gas temperature is 540 K.

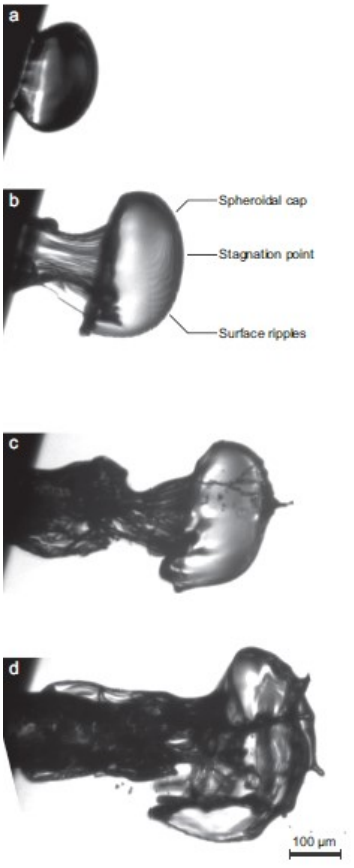

(b) Injection pressure is 40 MPa; gas pressure is 0.1 MPa; gas temperature is 293 K.

Figure 4.5: High-speed spray images in the initial stage [172, 173].

The theoretical empirical penetration model by Naber and Siebers [56], which was derived using the penetration time and length scale, also predicted a linear dependence of penetration on time for short times and a square root dependency on time for longer times. The model proposed by Jung et al. [174], with a slight modification of Hiroyasu's two-stage model, has been used in the GT-Suite simulation code [175] for combustion in Direct-Injection Diesel engines.

A general form of the two-stage model can be written as:

$$
\begin{aligned}
S(t) &= C_{k1}\left(\frac{2\Delta P}{\rho_l}\right)^{0.5} t, \quad t < t_{bu} \\
S(t) &= C_{k2}\left(\frac{\Delta P}{\rho_g}\right)^{0.25}\left(D_n t\right)^{0.5}, \quad t > t_{bu} \\
t_{bu} &= C_{k3}\frac{\rho_l D_n}{\sqrt{\rho_g \Delta P}}
\end{aligned}
\tag{4.2}
$$

Here ρ_l is the density of liquid fuel (n-dodecane in the present work). The constants (C_{k1}, C_{k2} and C_{k3}) for the models mentioned above are given in Table 4.1. The area contraction coefficient (C_a), discharge coefficient (C_{dc}) and velocity coefficient (C_v) are related by $C_{dc} = C_a \cdot C_v$. θ is the spray spreading angle and a is a tuning constant.

Table 4.1: Model constants of two-stage model

Authors	C_{k1}	C_{k2}	C_{k3}
Hiroyasu et al. [86]	0.39	2.95	28.65
Naber et al. [56]	C_v	$\frac{C_v^{1/2}(2C_a)^{1/4}}{(a\cdot tan(\theta/2))^{1/2}}$	$\frac{(0.5C_a)^{1/2}}{a\cdot C_v\cdot tan(\theta/2)}$
Jung et al. [174]	C_{dc}	2.95	$4.351/(C_{dc})^2$

4.2 Spray penetration prediction

4.2.1 Results

As discussed earlier, the empirical penetration model constants are often treated as tuning (or empirical) constants that need calibration from spray measurement. In this section, the two empirical penetration models (model of Dent, model of

Hiroyasu) mentioned in the previous section are first evaluated by comparing against the ECN data. After that, the models will be used for the marine spray cases.

It can be seen from Figure 4.6 that the model of Dent underestimates the spray penetration for both the SA and SD case. Generally, the model of Hiroyasu gives good agreement with the measurement data, except for the slight underestimation of the SD case during 0.6 to 1.1 ms ASOI. This slight difference can be improved by increasing the value of the empirical model constant C_{k2}. As shown in Figure 4.7, the value of C_{k2} = 3.09 gives a better fit with the experiment than the value of C_{k2} = 2.95 suggested by Hiroyasu. As explained in section 4.1, the value of C_{k2} depends on the nozzle flow conditions of the injector. The physical implication of the effects of increasing of the value of C_{k2} needs further investigation. The results also indicate that the spray penetration is independent of ambient gas temperature.

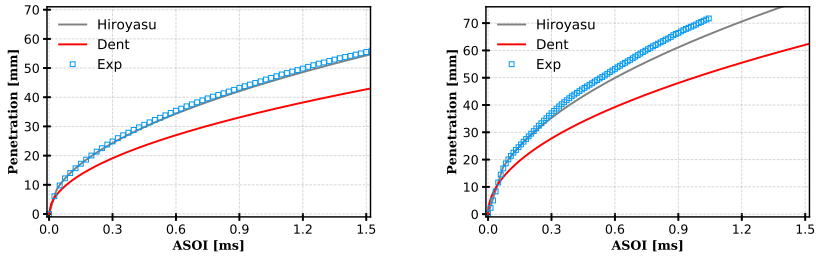

(a) SA case (b) SD case

Figure 4.6: Spray penetration prediction of the ECN cases

In contrast to the common rail system, which shows a “top hat” injection profile, used in the ECN spray cases, the PLN system used for the marine cases has a

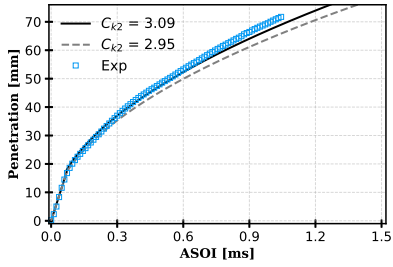

Figure 4.7: Spray penetration prediction with different values of the empirical model constant C_{k2}.

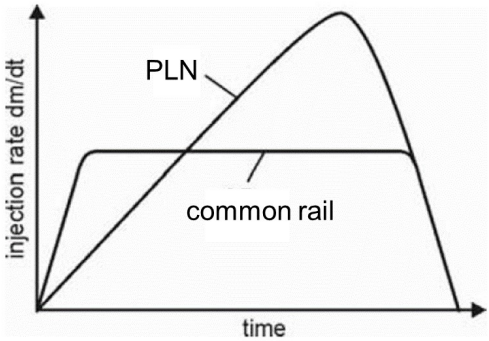

Figure 4.8: Typical injection rate profiles of common rail and pump-line-nozzle system [106]

"triangle-shaped" injection profile (see Figure 4.8). In order to have a better representation of the behavior of a PLN system, a time-dependent injection pressure profile is considered here for the empirical spray penetration model prediction. The updated form of Dent's model, Eq. (4.1), is written in the following discretized form:

$$\begin{aligned} S(t) &= \sum_{i=0}^{t} S(t_i) = \sum_{i=0}^{t} 3.07\Big(\frac{\Delta P_i}{\rho_g}\Big)^{0.25} (D_n)^{0.5} (\frac{294}{T_g})^{0.25} (t_i)^{0.25} \\ &= 3.07\Big(\frac{294}{\rho_g T_g}\Big)^{0.25} (D_n)^{0.5} \sum_{i=0}^{t} (\Delta P(t_i))^{0.25} (t_i)^{0.5} \end{aligned} \tag{4.3}$$

where $\Delta P(t_i)$ is the pressure difference ΔP in Eq. (4.2) at time t_i. The time step Δt = 0.0248 ms, determined by the data acquisition system, is used in this work. The same approach is utilized for the two-stage models.

In Figure 4.9, the solid lines are the results using a constant (peak) injection pressure value, whereas the dashed lines represent the results using the updated time-dependent injection pressure profile. This comparison shows that the dashed lines have a smaller discrepancy with the measurement. The evident distinction indicates that it is necessary to use the time-dependent approach for the spray penetration with a PLN system, although further improvements are necessary, as explored below.

Many theoretical works [168, 176–178] based on mass and momentum conservation and experimental results show that the spray penetration is a function of the pressure difference ΔP, the density of the liquid fuel ρ_l or the ambient gas ρ_g, the injector nozzle diameter D_n, and the time after the start of injection, which

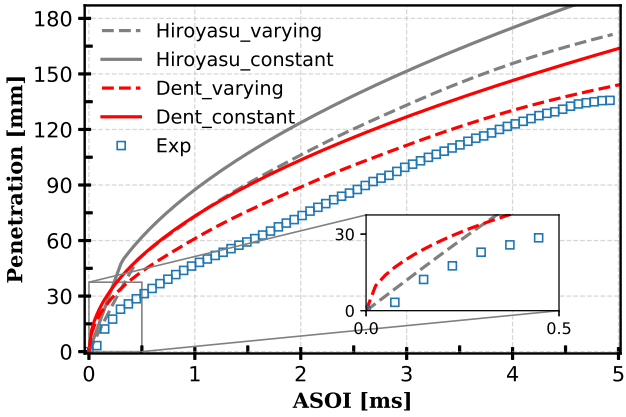

Figure 4.9: Comparison of different algorithms for the GS Case1

can be written in the equation below:

$$S(t) = K \cdot (\Delta P)^a \cdot \rho^b \cdot (D_n)^c \cdot t^d \tag{4.4}$$

where K is a tuning constant to fit the experimental data. It should be noted that parameters such as orifice area coefficient C_a, velocity coefficient C_v and spray spreading angle θ are also affecting the penetration. The accurate values of these parameters, however, are usually difficult to obtain in real engine test benches. For this reason, the effect of these parameters is not taken into account in Eq. (4.4), and the tuning constant K is employed instead to represent the combined effect. Replacing the variables in Eq. (4.4) with their units gives:

$$\begin{aligned} m &= \left(\frac{kg}{m \cdot s^2}\right)^a \left(\frac{kg}{m^3}\right)^b \cdot m^c \cdot s^d \\ &= kg^{(a+b)} \cdot m^{(c-a-3b)} \cdot s^{(d-2a)} \end{aligned} \tag{4.5}$$

Through dimensional analysis [179] the relation between the four exponents can be obtained:

$$\begin{aligned} a + b &= 0 \\ c - a - 3b &= 1 \\ d - 2a &= 0 \end{aligned} \tag{4.6}$$

It is clear in Figure 4.9 that in the very early stage of the spray, the $S \propto t$ relation shows better agreement than the $S \propto \sqrt{t}$ relation. Therefore, the two-stage model is used for further investigation.

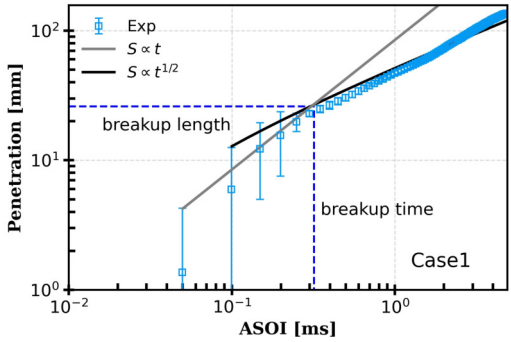

(a) Spray penetration versus time in log-log coordinates

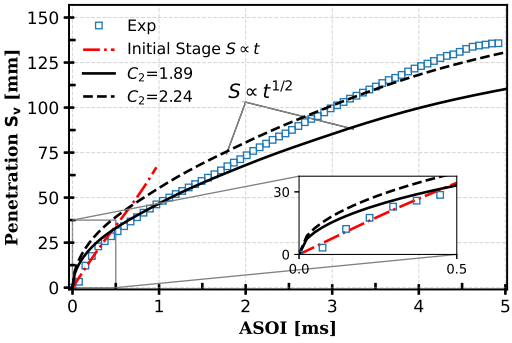

(b) Comparison between measurement and model prediction

Figure 4.10: Empirical spray penetration model of the GS Case1

Figure 4.10(a) is a plot of the spray penetration (S_v) versus time in log-log coordinates. Consistent with other research [56, 58, 86, 180], the spray penetration shows different behavior according to time after injection: an initial stage, where a linear behavior of penetration with time $S \propto t$ can be observed; and the fully developed or second stage where the penetration is a function of the square root of time $S \propto \sqrt{t}$. Figure 4.10(b) shows a good agreement between the measurements and the two-stage model prediction from 0 to 2 ms with $C_{k1} = 0.25$, $C_{k2} = 1.89$, whereas the deviation is evident after 2 ms. With a larger value of C_{k2} (dashed black line), the model overestimates the spray penetration, although a good agreement is shown from 3 to 5 ms.

The research summarized in Table 4.2 found that for the fully developed spray, the penetration scales proportional with the square root of time $S \propto \sqrt{t}$. Naber

Table 4.2: Overview of empirical spray penetration models with experimental validation

Authors	Time span [ms]	Penetration [mm]	Ambient density [kg/m^3]	Ambient Temperature [K]
Naber et al. [56]	< 3	< 100	3.6-124	451/1000
Sazhin et al. [181]	< 2.2	< 100	1.16-12.33	300-480
Desantes et al. [177]	< 2	< 60	12-69	300
Payri et al. [180]	< 2	< 65	10-40	306
Gimeno et al. [91]	< 2.5	< 100	7.6-35	700-900

et al. [56] used integral control surface techniques to analyze incompressible jets and sprays. Unlike the work of Naber [56], the theoretical model proposed by Desantes et al. [177] assumed that the axial velocity follows a Gaussian distribution. Contrary to the models above, Sazhin et al. [181] developed the empirical penetration model from the general equation describing the dynamics of an individual droplet and also found the $S \propto \sqrt{t}$ relation.

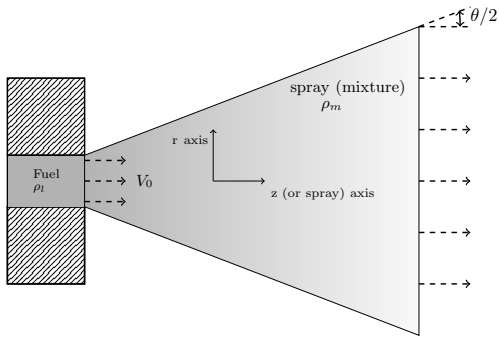

Figure 4.11: Schematic of the spray model proposed by Pozorski et al. [182]. Pozorski et al. assumed that the density distribution in the r axis is not a constant but follows the function of Eq. (4.7)*.*

In the analytical expression by Pozorski et al. [182], following the approach similar to Sazhin et al. [181], but considering the effects of turbulence in the fuel-air mixing region, the spray penetration at large distances from the nozzle is expected to be proportional to $t^{2/3}$. Instead of assuming that the density of the gas and fuel droplets mixture (ρ_m) is constant in the planes perpendicular to the spray axis inside the spray (the conical-shape region in Figure 4.11), the authors

presumed that it depends on the distance from the spray axis:

$$\rho_m = \rho_{m0}(z)\exp\Big(-\frac{V_0 r^2}{4D_t z}\Big) \tag{4.7}$$

where ρ_{m0} is the mixture density at the spray axis, D_t in [m^2/s] is the turbulent diffusion coefficient, V_0 is the injection velocity. As shown in Figure 4.11, the $S \propto \sqrt{t}$ model is obtained with the hypothesis that the density of the fuel-air mixture remains constant inside the spray.

The solution of Eq. (4.6) can be acquired when $d = 2/3$. The combination of measurement data and Eq. (4.4) then gives the following equation:

$$S(t) = 0.46\Big(\frac{\Delta P}{\rho_g}\Big)^{1/3}\Big(D_n\Big)^{1/3} t^{2/3} \tag{4.8}$$

The solid black lines in Figures 4.12 to 4.15 are the results from Eq. (4.8), while the other two lines represent the prediction of Eq. (4.2). Again, the difference between measurement and prediction of the two-stage model (Eq. (4.2), with C_{k1} = 0.25 and C_{k2} = 1.89) is evident as the spray penetrates further in the combustion chamber. Noticeably better fits are provided by the plot of $S \propto t^{2/3}$. The small difference between the model of $S \propto t^{1/2}$ and $S \propto t^{2/3}$ in Figures 4.12 to 4.15 reveals that the turbulence effect becomes stronger as the spray penetrates further in the combustion chamber.

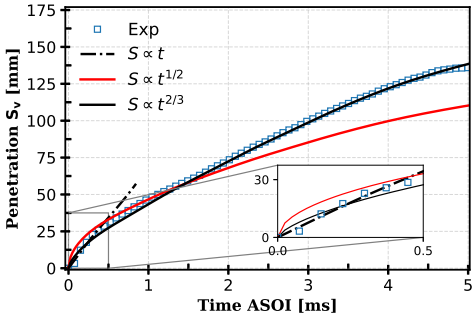

Figure 4.12: Spray penetration comparison of the GS Case1

Under high density (22.5 kg/m^3) conditions, however, the spray penetration at larger distances is proportional to $t^{1/2}$ (red line), which is shown in Figures 4.16 to 4.18. The results from Eq. (4.8) show a relatively large deviation for the GS Case 4, 5 and 6. The corresponding model coefficients for the two-stage model (Eq. (4.2)) are as follows: C_{k1} = 0.39 (for GS Case 4,5,6); C_{k2} = 2.19 (for GS Case 4,6) and C_{k2} = 1.79 (for GS Case5).

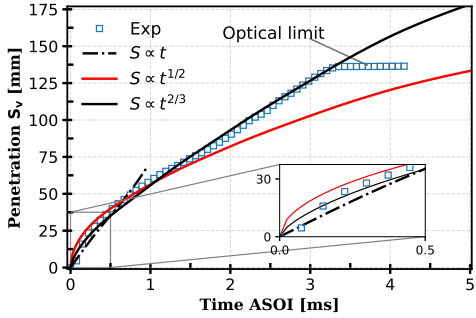

Figure 4.13: Spray penetration comparison of the GS Case2

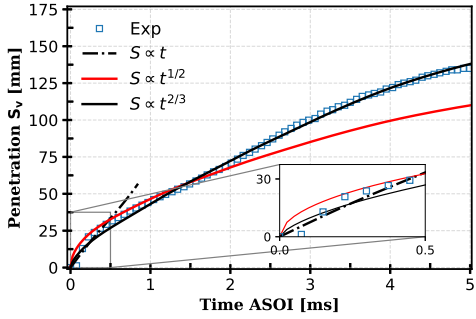

Figure 4.14: Spray penetration comparison of the GS Case3

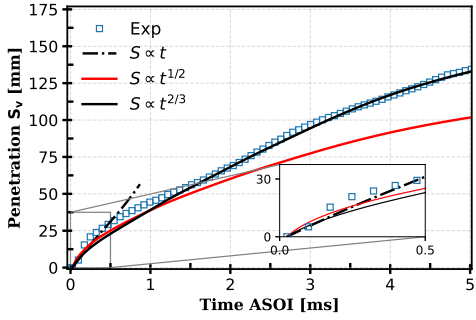

Figure 4.15: Spray penetration comparison of the GS Case7

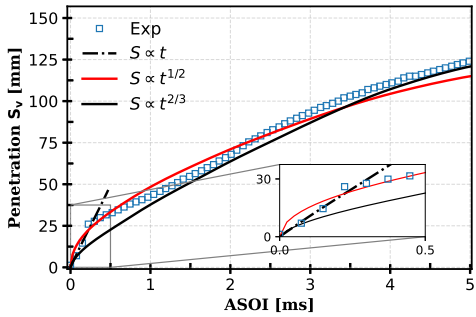

Figure 4.16: Spray penetration comparison of the GS Case4

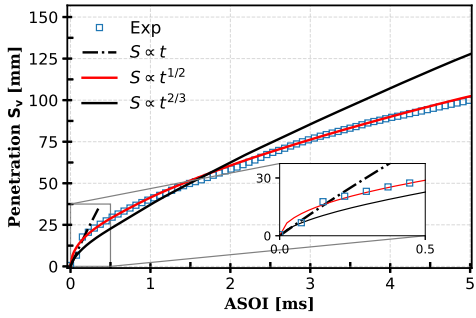

Figure 4.17: Spray penetration comparison of the GS Case5

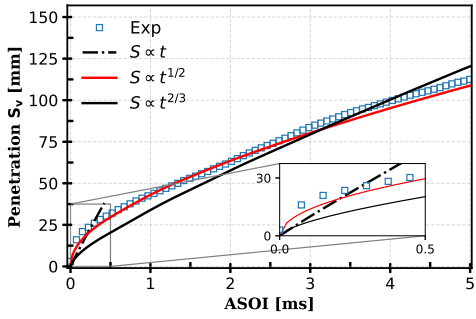

Figure 4.18: Spray penetration comparison of the GS Case6

The results of Figures 4.12 to 4.15 and Figures 4.16 to 4.18 demonstrate that the effect of turbulence is evident at low density conditions (7.6 and 15.2 kg/m^3) and the spray penetration at larger distances from the nozzle exit then is a function of $t^{2/3}$.

The influence of engine load can be better explained combined with the spray correlation mentioned above. It can be seen in Figure 4.16 that the $S \propto t^{1/2}$ model begins to underestimate the spray penetration from about 3 ms ASOI, but the model is still able to predict the result of the GS Case5. The injection profiles show different trends: for GS Case4, the injection pressure begins to drop after about 3 ms ASOI, when the peak injection pressure is reached; for GS Case5, the peak injection pressure is reached at about 4.7 ms ASOI. From the discussion above, the spray penetration behavior ($S \propto t^{1/2}$ or $S \propto t^{2/3}$) is also affected by the injection pressure characteristic of the fuel injection system.

4.2.2 Discussion on the model of Pozorski

In the last section, Pozorski et al. [182] hypothesized that the density distribution inside the spray region follows a Gaussian function (normal distribution) at large distances from the nozzle. In this section, the hypothesis proposed by Pozorski et al. [182] will be tested by using the CFD results obtained in Chapter 3.

Pozorski et al. [182] assumed that the density outside the spray region is zero. Following this assumption, the normalized density ρ_{nor} is defined as follows

$$\rho_{nor} = \frac{\rho_m - \rho_{m0}}{\rho_{m0}} \tag{4.9}$$

That is, the density in the spray region minus the density at the spray axis and then divided by the density at the spray axis.

The normalized density for each case is plotted as a function of radial distance from the spray axis in Figure 4.19. The distribution profile at 3.5 ms ASOI is chosen because the spray has then reached the steady state. In Ref. [182], Pozorski et al. found that the $t^{2/3}$ plot provides a better fit than the $t^{1/2}$ at large distances from the nozzle. Therefore, different cross-sections at the far field downstream the nozzle are employed due to the different ambient conditions. For example, the spray penetration of GS Case2 is about 125 mm at 3.5 ms ASOI, while the penetration of GS Case6 is around 80 mm at that time.

As illustrated in Figure 4.19, the density distribution at the far field of the nozzle generally follows a Gaussian function, except for the slight deviation of GS Case1

and GS Case2, which is probably due to the evaporation of a detached ligament as analyzed in Chapter 3. This is not surprising because the fluid concentration in a fully developed turbulent jet is Gaussian, as explained by Pope [183].

The Gaussian distribution function in Figure 4.19 in terms of radial distance from the spray axis r_m (in [mm]) can be expressed in the following form:

$$\rho_{nor} = \exp\Big(-\frac{r_m^2}{2{\sigma_m}^2}\Big) \tag{4.10}$$

where σ_m represents the standard deviation of the distribution function. The values of σ_m for all cases are listed in Table 4.3.

Table 4.3: The value of σ_m for each case

Case	σ_m
Case1	7.06
Case2	7.18
Case3	9.77
Case4	8.12
Case5	6.86
Case6	7.41
Case7	6.68

From the discussion above, although the $t^{2/3}$ law gives a better prediction than the $t^{1/2}$ law, both experimental and theoretical studies in this direction are needed for further research [133]. This would be useful in marine engine designs because the injection duration for marine engines is relatively long compared to that for automotive engines, and the fuel spray tip versus the moving piston should also be considered in an operating engine.

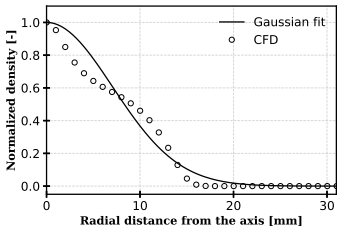

(a) Case1, 100mm downstream the injector

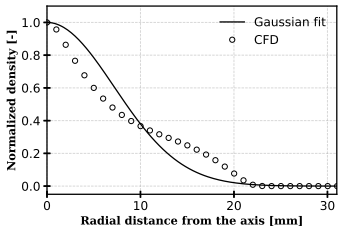

(b) Case2, 100mm downstream the injector

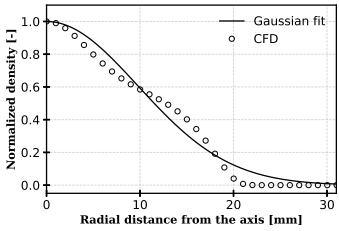

(c) Case3, 95mm downstream the injector

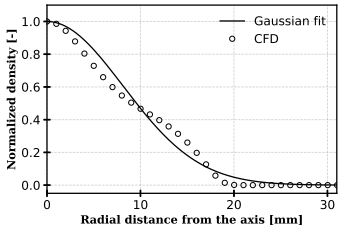

(d) Case4, 85mm downstream the injector

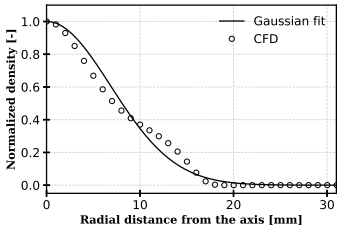

(e) Case5, 75mm downstream the injector

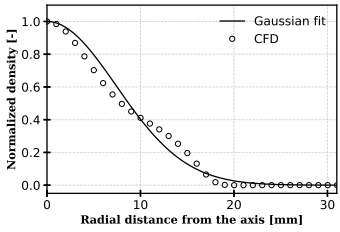

(f) Case6, 90mm downstream the injector

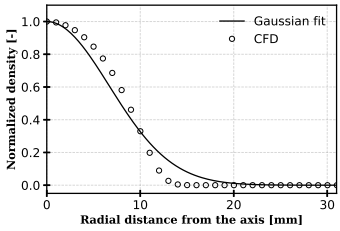

(g) Case7, 100mm downstream the injector

Figure 4.19: Normalized density distribution along radial distance from the spray axis.

4.3 Closure

Compared to the CFD simulation, the empirical spray penetration model is relatively simple and thus is also widely used for engine simulations. After reviewing the development of empirical penetration models, two models were adopted for further research. Based on the injection characteristics of the PLN system used in the setup, the algorithm for an existing empirical spray penetration model has been updated to take the varying injection pressure into account. From the analysis of the measurement results and model evaluation, the following conclusions are drawn:

- The comparison in this chapter shows that the two-stage empirical penetration model provides a better prediction than Dent's model, indicating that the spray penetration is independent of ambient gas temperature. Combining the research in the literature and analysis performed in this chapter, the spray penetration is a function of the pressure difference, the density of liquid fuel or/and the density of ambient gas, and the injector nozzle diameter.
- The good prediction of the two-stage empirical penetration model and the recent publication [169–171] further reveals the existence of a breakup time and breakup length. The injected fuel can be regarded as unbroken within the breakup length near the nozzle exit. Beyond the breakup length, the liquid fuel is fully atomized.
- The prediction performance of the empirical penetration model can be improved by adjusting the value of the model constants. However, the value depends on the details of the injection conditions (e.g., nozzle designs, nozzle flows). Further studies are still needed to obtain a more accurate expression of the empirical penetration model.
- A time-dependent injection pressure profile is essential for a transient injection profile, such as for PLN systems, when using the spray empirical model to predict the spray tip penetration.
- The spray penetration at lower ambient gas density conditions (7.6 and 15.2 $\mathrm{kg/m^3}$) is found to be a three-stage function of time after injection. At the initial stage, the penetration is linear with time $S \propto t$. At large distances from the nozzle the penetration is proportional to $t^{2/3}$. For intermediate distances, the $t^{2/3}$ model and $t^{1/2}$ model both have a small deviation.
- The penetration for a fully developed spray is a function of $t^{1/2}$ at high density (22.5 $\mathrm{kg/m^3}$) conditions.

5 Conclusions

5.1 Conclusions of present work

Due to higher technical demands and expense, research targeting medium speed four-stroke marine engines is still rare. Based on the previous in-house measurements in the GUCCI setup, this research focuses on the modeling work of evaporating sprays under engine-like conditions. The modeling work includes two parts: a CFD simulation using a RANS approach and the empirical spray penetration model.

The spray data within the ECN were first used to validate the CFD code and study the influence of the mesh and sub-models on the CFD results. After that, the same approaches were applied to the sprays for marine engines. A relatively large discrepancy was found between the measured data and the simulated results. As guided by the "mixing-controlled" concept, the turbulence coefficient (C_1 in the standard $k-\varepsilon$ model), which governs the mixing process of sprays, was proven to cause the discrepancy. In addition, this work summarized the value of this coefficient used by different researchers for diesel spray simulations. A general trend was found that for large nozzle diameter and low injection velocity, a lower value was suggested. This finding indicated that the spray process in marine engines, targeted in this work, has a higher spreading rate than those in

the automotive- and truck-sized engines.

The spray tip penetration, which represents a parameter for the air utilization in diesel engines, is also vital for engine design and optimization. The empirical spray penetration model is widely used in engine simulation codes due to its simplicity. Similar to the methodology adopted in the CFD research, two classical empirical penetration models were employed to predict the penetration results of the ECN cases before using them for the marine engine sprays. Considering the injection characteristics of marine engines, a varying injection profile was suggested to describe the actual process better. Although improvement was made by accounting for the varying injection profile, disagreement was still found between the measurements and the predicted results for some cases. The $S \propto t^{2/3}$ model, which differs from the classical $S \propto t^{1/2}$ model, was proposed by previous studies and used in this work. Under low ambient gas density (7.6 and 15.2 kg/m^3) conditions, the $S \propto t^{2/3}$ model gave a better agreement with measurement, while the $S \propto t^{1/2}$ model remained valid under high density (22.5 kg/m^3) conditions.

5.2 Recommendations for future work

This work can be seen as a preliminary modeling study for the spray process in medium speed marine engines. Future work is needed to deepen the understanding of the relevant physical (or/and chemical) processes. At the end of this Ph.D., some recommendations for future work are given below.

Experimental data is definitely essential to support the modeling work. The results in Chapter 3 showed that the simulation underestimates the measurement in the near nozzle region. As discussed in Chapter 2, the near nozzle region behavior has a limited influence on the global quantities or the downstream characteristics. Thus, this work does not concentrate on near-nozzle research. But further research is necessary to provide insight into the relationship between the nozzle flow behavior and the global spray quantities. According to the publication from Argonne National Laboratory [112, 113], this might, however, face many challenges and difficulties, especially in the experimental system. The ligament detachment, a possible reason for the disagreement between the CFD results and the measurements at low temperature conditions, also needs further studies. More advanced optical techniques may be utilized to detect this phenomenon. In terms of the CFD simulation, the mixing process in marine engines differs from that in the smaller-sized engines. But there is no (to the author's knowledge) experimental research on the mixing process in marine engines.

As is the trend, the PLN system is being replaced by the common rail injection system in marine engines (as mentioned in Chapter 2). ABC has designed and developed new engines (e.g., 6/8DL36 engine family) equipped with common rail systems. The current PLN system has a different injection feature ("triangle-shaped" profile) from the common rail system ("top hat" profile). Thus, a common rail system is recommended to install on the GUCCI setup to study the spray characteristics. This would enable a direct comparison of the features of PLN versus common rail and provide suggestions on the selection of injection systems.

For the modeling work, as mentioned in the previous paragraph, the spray behavior at the near nozzle region, which is related to the flow conditions in the injector nozzle, also needs CFD simulation. This also suggests that the Eulerian-Eulerian approach should be employed. This work discussed the effect of the turbulence model coefficient on evaporating (non-reacting) sprays. Its effect on reacting (or combusting) sprays is even more worthwhile because this is closer to the real engine conditions.

List of Appendices

A

OpenFOAM code

A.1 Gas phase

Conservation equation of mass:

$$\frac{\partial \rho}{\partial t} + \nabla \cdot (\rho U) = \dot{S}_p$$

```
for (label i = 0; i< Y.size(); i++)
{
    if (dieselSpray.isLiquidFuel()[i])
    {
       Sevap += dieselSpray.evaporationSource(i);
    }
}

{
    solve
    (
        fvm::ddt(rho)
      + fvc::div(phi)
      ==
        Sevap
    )
}
```

Conservation of species:

$$\frac{\partial Y_i}{\partial t} + \nabla \cdot (\rho U Y_i) = \nabla \cdot \left[(\mu + \mu_t) \nabla Y_i \right] + \dot{S}_{p,i} + \dot{S}_{chem,i}$$

```
for (label i = 0; i< Y.size(); i++)
{
    if (Y[i].name() != inertSpecie)
    {
        volScalarField& Yi = Y[i];

        solve
        (
            fvm::ddt(rho, Yi)
          + mvConvection->fvmDiv(phi, Yi)
          - fvm::laplacian(thermo.mu() + rSct * turbulence->mut(), Yi)
          ==
            dieselSpray.evaporationSource(i)
          + chemistry.RR(i),
            mesh.solver("Yi")
        );

        Yi.max(0.0);
        Yt += Yi;
    }
    else
    {
        inertIndex = i;
    }
}
```

Conservation of momentum:

$$\frac{\partial \rho U}{\partial t} + \nabla \cdot (\rho U U) = -\nabla p + \nabla \cdot \left[(\mu + \mu_t)(\nabla U + (\nabla U)^T) \right] - \nabla \cdot \left[(\mu + \mu_t)(\frac{2}{3}\mathbf{tr}(\nabla U)^T) \right] + \rho g + \dot{S}_M$$

```
   fvVectorMatrix UEqn
   (
       fvm::ddt(rho, U)
     + fvm::div(phi, U)
     + turbulence->divDevRhoReff(U)
    ==
       rho*g
     + dieselSpray.momentumSource()
   );

   UEqn.relax();

   if (pimple.momentumPredictor())
   {
      solve(UEqn == -fvc::grad(p));
   }
```

Conservation equation of energy:

$$\frac{\partial \rho h}{\partial t} + \nabla \cdot (\rho U h) = \nabla \cdot \left[(\alpha + \alpha_t) \nabla h \right] + \dot{S}_Q + \frac{Dp}{dt}$$

```
solve
(
    fvm::ddt(rho, hs)
  + mvCovection->fvmDiv(phi, hs)
  - fvm::laplacian(turbulence->alphaEff(), hs)
 ==
    DpDt
  + dieselSpray.heatTransferSource()().dimensionedInternalField()
  + chemistrySh
);
```

Turbulent kinetic energy k:

$$\frac{\partial}{\partial t}(\rho k) + \nabla \cdot (\rho U k) = \nabla \cdot \left[(\mu + \frac{\mu_t}{\sigma_k}) \nabla k \right] + G - \frac{2}{3} \rho k (\nabla \cdot U) - \rho \varepsilon + \dot{S}_k$$

```
// Turbulent kinetic energy equation

tmp<fvScalarMatrix> kEqn
(
    fvm::ddt(rho_, k_)
  + fvm::div(phi_, k_)
  - fvm::laplacian(DkEff(), k_)
 ==
    G
  - fvm::SuSp((2.0/3.0)*rho_*divU, k_)
  - fvm::Sp(rho_*epsilon_/k_, k_)
);

// Re-calculate viscosity
mut_ = rho_*Cmu_*sqr(k_)/epsilon_;
mut_.correctBoundaryConditions();

// Re-calculate thermal diffusivity
alphat_ = mut_/Prt_;
alphat_.correctBoundaryConditions();
```

Turbulent dissipation ε:

$$\frac{\partial}{\partial t}(\rho \varepsilon) + \nabla \cdot (\rho U \varepsilon) = \nabla \cdot \left[(\mu + \frac{\mu_t}{\sigma_\varepsilon}) \nabla \varepsilon \right] + C_1 G \frac{\varepsilon}{k} - (\frac{2}{3} C_1 - C_3) \rho \varepsilon (\nabla \cdot U) - C_2 \rho \frac{\varepsilon^2}{k} + \dot{S}_\varepsilon$$

```
tmp<volTensorField> tgradU = fvc::grad(U_);
volScalarField G(GName(), mut_*(tgradU() && dev(twoSymm(tgradU()))));
tgradU.clear();

// Update epsilon and G at the wall
epsilon_.boundaryField().updateCoeffs();

// Dissipation equation
tmp<fvScalarMatrix> epsEqn
(
```

```
      fvm::ddt(rho_, epsilon_)
    + fvm::div(phi_, epsilon_)
    - fvm::laplacian(DepsilonEff(), epsilon_)
   ==
      C1_*G*epsilon_/k_
    - fvm::SuSp(((2.0/3.0)*C1_ + C3_)*rho_*divU, epsilon_)
    - fvm::Sp(C2_*rho_*epsilon_/k_, epsilon_)
    );
```

A.2 Liquid phase

Drag model

Drag coefficient

$$C_d = \begin{cases} \frac{24}{Re_d}\left(1 + \frac{1}{6}Re_d^{2/3}\right), & Re < 1000 \\ 0.424, & Re > 1000 \end{cases}$$

```
scalar standardDragModel::Cd
(
    const scalar Re,
    const scalar dev
) const
{
    scalar drag = CdLimiter_;

    if (Re < ReLimiter_)
    {
        drag =  24.0*(1.0 + preReFactor_*pow(Re, ReExponent_))/Re;
    }

    // correct for deviation from sphericity
    drag *= (1.0 + Cdistort_*dev);

    return drag;
}
```

The momentum relaxation time

$$\tau_u = \frac{4}{3}\frac{\rho_d D}{\rho C_d |u_d - u|}$$

```
Foam::scalar Foam::standardDragModel::relaxationTime
(
    const vector& URel,
    const scalar diameter,
    const scalar rho,
    const scalar liquidDensity,
    const scalar nu,
    const scalar dev
) const
{
    scalar time = GREAT;
```

```
    scalar Re = mag(URel)*diameter/nu;

    if (Re > 0.1)
    {
        time = 4.0*liquidDensity*diameter/(3.0*rho*Cd(Re, dev)*mag(URel));
    }
    else
    {
        time = liquidDensity*diameter*diameter
               /(18*rho*nu*(1.0 + Cdistort_*dev));
    }

    return time;
}
```

Evaporation model

The Sherwood number:

$$Sh = 2.0 + 0.6 Re^{1/2} Sc^{1/3}$$

```
scalar standardEvaporationModel::Sh
(
    const scalar ReynoldsNumber,
    const scalar SchmidtNumber
) const
{
    return
        2.0
      + preReScFactor_
       *pow(ReynoldsNumber, ReExponent_)
       *pow(SchmidtNumber, ScExponent_);
}
```

The evaporation relaxation time:

$$\tau_{\text{evap}} = \frac{\rho_d D_d^2}{6 \mathcal{D} \rho_v Sh \ln(1+B)}$$

```
Foam::scalar Foam::standardEvaporationModel::relaxationTime
(
    const scalar diameter,
    const scalar liquidDensity,
    const scalar rhoFuelVapor,
    const scalar massDiffusionCoefficient,
    const scalar ReynoldsNumber,
    const scalar SchmidtNumber,
    const scalar Xs,
    const scalar Xf,
    const scalar m0,
    const scalar dm,
    const scalar dt
) const
{
    scalar time = GREAT;
    scalar lgExpr = 0.0;
```

```
    scalar Xratio = (Xs - Xf)/max(SMALL, 1.0 - Xs);

    if (Xratio > 0.0)
    {
        lgExpr = log(1.0 + Xratio);
    }


    scalar denominator =
        6.0*massDiffusionCoefficient
       *Sh(ReynoldsNumber, SchmidtNumber)
       *rhoFuelVapor*lgExpr;

    if (denominator > SMALL)
    {
        time = max(VSMALL, liquidDensity*sqr(diameter)/denominator);
    }

    return time;
}
```

Heat transfer model

The Nusselt number:

$$Nu = 2.0 + 0.6Re^{1/2}Pr^{1/3}$$

```
scalar RanzMarshall::Nu
(
    const scalar ReynoldsNumber,
    const scalar PrandtlNumber
) const
{
    return
        2.0
      + preRePrFactor_
       *pow(ReynoldsNumber, ReExponent_)
       *pow(PrandtlNumber, PrExponent_);
}
```

The heat transfer relaxation time:

$$\tau_h = \frac{m_d c_{l,d}}{\pi D_d \kappa Nu} = \frac{\rho_d D_d^2 c_{l,d}}{6\kappa Nu}$$

```
scalar RanzMarshall::relaxationTime
(
    const scalar liquidDensity,
    const scalar diameter,
    const scalar liquidcL,
    const scalar kappa,
    const scalar ReynoldsNumber,
    const scalar PrandtlNumber
) const
{
    scalar time =
```

```
        liquidDensity
       *sqr(diameter)
       *liquidcL
       /(6.0*kappa*Nu(ReynoldsNumber, PrandtlNumber));

    time = max(SMALL, time);

    return time;
}
```

B

Source terms in governing equations

It is an extremely complex problem to solve the dynamics of spray droplets and their interactions with the gas phase [184]. Instead of tracking every individual droplet which is computationally demanding, a probability distribution function is often used [121, 184].

The droplet distribution function f_d accounts for eleven independent variables, i.e., three droplet position components *vecx*, three droplet velocity components *vecv*, droplet radius r, droplet temperature T_d, distortion from sphericity y, time change rate of distortion $\dot{y} = dy/dt$, and time t.

The probable number of droplet per unit volume at position $\vec{x}$ and time t with velocities in the interval $(\vec{v}, \vec{v} + \mathrm{d}\vec{v})$, radii in the interval $(r, r + \mathrm{d}r)$, temperatures in the interval $(T_d, T_d + \mathrm{d}T_d)$, and displacement parameters in the intervals $(y, y + \mathrm{d}y)$ and $(\dot{y}, \dot{y} + \mathrm{d}\dot{y})$ can be calculated from the equation below:

$$f_d(\vec{x}, \vec{v}, r, T_d, y, \dot{y}, t)\mathrm{d}\vec{v}\ \mathrm{d}r\ \mathrm{d}T_d\ \mathrm{d}y\ \mathrm{d}\dot{y} \tag{B.1}$$

The spray equation can be expressed as the time evolution of f_d:

$$\frac{\partial f_d}{\partial t} + \nabla_{\vec{x}} \cdot (f_d \vec{v}) + \nabla_{\vec{v}} \cdot (f_d \vec{F}) + \frac{\partial}{\partial r}(f_d R) + \frac{\partial}{\partial T_d}(f_d \dot{T}_d) + \frac{\partial}{\partial y}(f_d \dot{y}) + \frac{\partial}{\partial \dot{y}}(f_d \ddot{y}) = \dot{f}_{coll} + \dot{f}_{bu} \tag{B.2}$$

where $\vec{F}$, R, $\dot{T}_d$, and $\ddot{y}$ are the time rates of change, following an individual drop, of its velocity, radius, temperature, and oscillation velocity $\dot{y}$. The quantities $\dot{f}_{coll}$ and $\dot{f}_{bu}$ are the source terms due to droplet collisions and breakup. By solving the spray equation (Eq. (B.2)) the source terms that describe the phase interactions can be obtained.

The source term of mass exchange in Eq. (3.1) is given as:

$$\dot{S}_p = -\int f_d \rho_d 4\pi r^2 R \mathrm{d}\vec{v}\, \mathrm{d}r\, \mathrm{d}T_d\, \mathrm{d}y\, \mathrm{d}\dot{y} \tag{B.3}$$

The source term of momentum exchange in Eq. (3.4) is given as:

$$\dot{S}_M = -\int f_d \rho_d \left(\frac{4}{3}\pi r^3 \vec{F}' + 4\pi r^2 R \vec{v}\right) \mathrm{d}\vec{v}\, \mathrm{d}r\, \mathrm{d}T_d\, \mathrm{d}y\, \mathrm{d}\dot{y} \tag{B.4}$$

where $\vec{F}' = \vec{F} - \vec{g}$ is the difference between the droplet and the gravitational accelerations [121].

The source term of energy exchange in Eq. (3.5) is given as:

$$\dot{S}_Q = \int f_d \rho_d \left\{ 4\pi r^2 R \left[I_l + \frac{1}{2}(\vec{v} - \vec{u})^2 \right] + \frac{4}{3}\pi r^3 \left[c_l \dot{T}_d + \vec{F}' \cdot (\vec{v} - \vec{u} - \vec{u}') \right] \right\} \mathrm{d}\vec{v}\, \mathrm{d}r\, \mathrm{d}T_d\, \mathrm{d}y\, \mathrm{d}\dot{y} \tag{B.5}$$

where $\vec{v} - \vec{u}$ is the relative velocity between the droplet and surrounding gas, $\vec{u}'$ is the turbulent fluctuation of the gas phase velocity, I_l is the internal energy of the droplet.

The source term of turbulent kinetic energy in Eq. (3.7) is given as:

$$\dot{S}_k = \int f_d \rho_d \frac{4}{3}\pi r^3 \vec{F}' \cdot \vec{u}' \mathrm{d}\vec{v}\, \mathrm{d}r\, \mathrm{d}T_d\, \mathrm{d}y\, \mathrm{d}\dot{y} \tag{B.6}$$

The source term $\dot{S}_\varepsilon$ of turbulent kinetic energy dissipation rate in Eq. (3.8) is equal to $(3\varepsilon/2k)\dot{S}_k$ [131, 184].

C

Sensitivity analysis of turbulence model constants on spray simulation results

This appendix performs the sensitivity analysis of other turbulence model constants (C_3, σ_k and σ_ε). The results show that the value of these model constants has an insignificant influence on the simulations.

C.1 Sensitivity analysis

The value of C_1 (of the $k-\varepsilon$ turbulence model) impacts the spray simulation results, and Chapter 3 also discusses its physical meaning. In this appendix, the sensitivity analysis of other model constants in the $k-\varepsilon$ model is performed to study their effects on the CFD results.

In Chapter 3, the CFD simulation with C_1 = 1.45, C_2 = 1.92, C_3 = 0.33, σ_k and σ_ε = 1.3 gives a good agreement with experimental data. When the value of C_1 is increased to 1.55, an obvious difference is shown for the marine engine spray cases (the GUCCI cases). Therefore, the sensitivity analysis here will be performed on

the GUCCI case (e.g., GS Case4). Similar to the variation of C_1, a larger variation (10%) is considered in this sensitivity analysis, as shown in Table C.1.

To the author's knowledge, the value of C_2 is set to 1.92 for the publications [71, 106, 119, 127, 131, 138, 184, 185] so far. Therefore in this analysis, its value is kept unchanged.

Table C.1: The value of C_1 used for spray simulations

Case	C_3	σ_k	σ_ε
Baseline	-0.33	1.0	1.3
Tc1	-0.297	1.0	1.3
Tc2	-0.363	1.0	1.3
Tc3	-0.33	0.9	1.3
Tc4	-0.33	1.1	1.3
Tc5	-0.33	1.0	1.17
Tc6	-0.33	1.0	1.43

Figures C.1, C.2, C.3 show the sensitivity analysis of C_3, σ_k, and σ_ε, respectively. The results from different cases almost overlap with each other. It is clear that the variation of these constants has a minor influence on the simulation results.

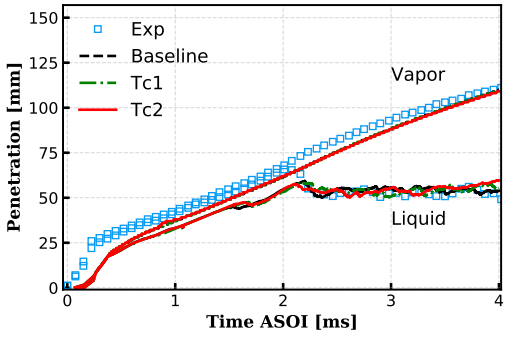

Figure C.1: Sensitivity analysis of the value of C_3 on simulation results

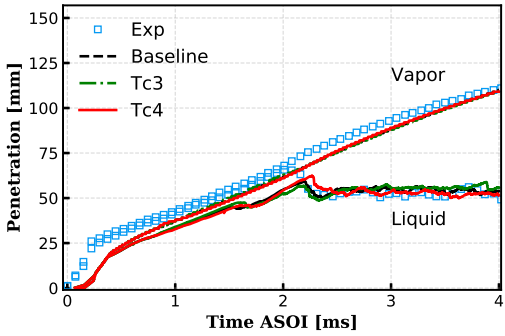

Figure C.2: Sensitivity analysis of the value of σ_k on simulation results

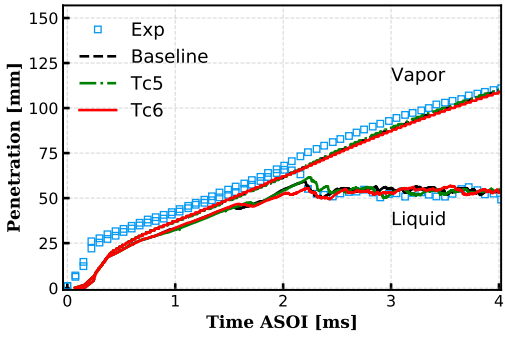

Figure C.3: Sensitivity analysis of the value of σ_ε on simulation results

D

Empirical penetration model derivation

This appendix presents the empirical spray penetration model derivations by Wakuri et al. [176] and Naber [56]. The derivation of Naber was based on the method of Wakuri, but with some modification. Therefore, the analysis by Wakuri et al. is given first, followed by the work of Naber.

D.1 The derivation by Wakuri

Assumptions made by Wakuri et al. [176]:

1. The size of fuel droplet is very small compared to the spray area.
2. The spray only has axial velocity and no velocity on radial direction. The axial velocity is uniform at a certain location.
3. There is no velocity slip between the fuel droplets and the entrained gas. That is, the relative velocity between the liquid fuel droplets and ambient gas can be ignored.
4. The fuel injection velocity is constant during the spray development process.

5. The spray shape is an idealized conical with a constant angle.

The fourth assumption does not account for the conditions in which the injection profile has a relatively long transient profile at the early injection stage. The real spray shape is illustrated in Figure D.1. As introduced in previous chapters, there is a head region at the spray tip caused by the vortex. In the derivation of spray penetration, this region is not considered, and the shape of the spray is simplified to be conical, as indicated by the dashed yellow line in Figure D.1. Figure D.1 gives a schematic illustration of a simplified spray used for empirical penetration model derivation.

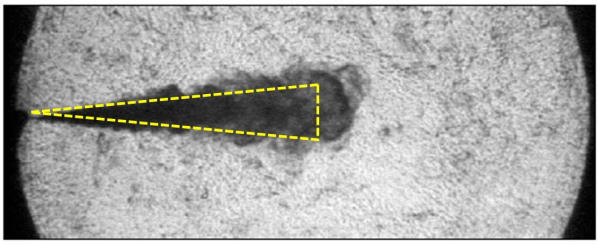

Figure D.1: Real spray shape and simplified shape (indicated by dashed yellow line) in derivation. Spray image is taken from Ref. [56].

As shown in Figure D.2, at the nozzle exit, the spray contains only liquid fuel. Therefore, the mass m_0 and momentum M_0 at the nozzle exit (location of $z = 0$) are

$$\text{Mass} \quad m_0 = \frac{\pi}{4} d_n^2 \rho_l V_0 \tag{D.1}$$

$$\text{Momentum} \quad M_0 = m_0 V_0 = \frac{\pi}{4} d_n^2 \rho_l V_0^2 \tag{D.2}$$

where d_n, ρ_l, and V_0 are nozzle diameter, liquid fuel density, and fuel injection velocity, respectively.

The mass $m(z)$ at a certain location z is is equal to the sum of liquid fuel mass and entrained gas mass:

$$m(z) = \frac{\pi}{4} d_n^2 \rho_l V_0 + \left\{ \pi \left[z \tan\left(\frac{\theta}{2}\right) + \frac{d_n}{2} \right]^2 V(z) - \frac{\pi}{4} d_n^2 V_0 \right\} \rho_g \tag{D.3}$$

where $V(z)$ is the velocity at location z.

The corresponding momentum at location z is $M(z) = m(z) \cdot V(z)$. According the momentum conservation $M_0 = M(z)$, the equation below can be obtained:

$$\frac{\pi}{4} d_n^2 \rho_l V_0^2 = \frac{\pi}{4} d_n^2 V_0 (\rho_l - \rho_g) V(z) + \pi \left[z \tan\left(\frac{\theta}{2}\right) + \frac{d_n}{2} \right]^2 \rho_g V(z)^2 \tag{D.4}$$

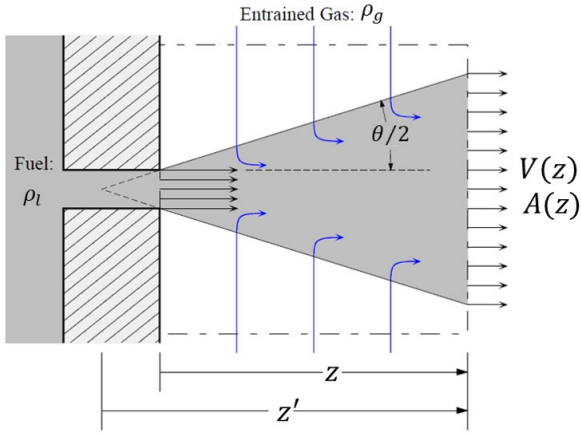

Figure D.2: Schematic of the empirical spray penetration model

Equation (D.4) can be rewritten into:

$$\left[z\tan(\frac{\theta}{2})+\frac{d_n}{2}\right]^2\rho_g V^2(z)+\frac{1}{4}d_n^2V_0(\rho_l-\rho_g)V(z)-\frac{1}{4}d_n^2\rho_l V_0^2=0 \tag{D.5}$$

Equation (D.5) can be simplified to Eq. (D.6) by letting $\delta = z/d_n$ and $\tilde{\rho} = \rho_l/\rho_g$ [1],

$$\left[\delta\tan(\frac{\theta}{2})+\frac{1}{2}\right]^2V(z)^2+\frac{1}{4}V_0(\tilde{\rho}-1)V(z)-\frac{1}{4}\tilde{\rho}V_0^2=0 \tag{D.6}$$

From Eq. (D.6) the velocity $V(z)$ can be obtained:

$$V(z)=\frac{V_0}{8}\frac{\sqrt{(\tilde{\rho}-1)^2+16\tilde{\rho}\left[\delta\tan(\frac{\theta}{2})+\frac{1}{2}\right]^2}-(\tilde{\rho}-1)}{\left[\delta\tan(\frac{\theta}{2})+\frac{1}{2}\right]^2} \tag{D.7}$$

As stated, Wakuri et al. [176] postulated the values of V_0, $\tilde{\rho}$, $\tan(\frac{\theta}{2})$ are constant when the spray is fully developed or reaches a steady state. Equation (D.8) can be obtained by considering the boundary condition ($\delta = 0$ at $t = 0$) in Eq. (D.7)

[1] δ represents the ratio of penetration length and nozzle diameter, and $\tilde{\rho}$ represent the ratio of liquid fuel density and ambient gas density.

$$\frac{1}{4\tan(\frac{\theta}{2})}\left(\frac{\tilde{\rho}-1}{\tilde{\rho}}\right)\left\{\left[\delta\tan(\frac{\theta}{2})+\frac{1}{2}\right]\cdot\right.$$
$$\left[\sqrt{1+\frac{16\tilde{\rho}}{(\tilde{\rho}-1)^2}\left[\delta\tan(\frac{\theta}{2})+\frac{1}{2}\right]^2}+2\right]-\frac{1}{2}\left[\sqrt{1+\frac{4\tilde{\rho}}{(\tilde{\rho}-1)^2}}+2\right]$$
$$\left.+\frac{\tilde{\rho}-1}{4}\sqrt{\frac{1}{\tilde{\rho}}}\ln\left|\frac{\frac{4}{\tilde{\rho}-1}\sqrt{\tilde{\rho}}\left[\delta\tan(\frac{\theta}{2})+\frac{1}{2}\right]+\sqrt{1+\frac{16\tilde{\rho}}{(\tilde{\rho}-1)^2}\left[\delta\tan(\frac{\theta}{2})+\frac{1}{2}\right]^2}}{\frac{2}{\tilde{\rho}-1}\sqrt{\tilde{\rho}}+\sqrt{1+\frac{4\tilde{\rho}}{(\tilde{\rho}-1)^2}}}\right|\right\}=V_0\frac{t}{d_n} \tag{D.8}$$

For sprays under diesel engine conditions, the value of δ ranges from 40 to 60, and the value of $\tilde{\rho}$ is from 300 to 400 expect the near nozzle region [176]. Thus, an approximation form of Eq. (D.8) can be expressed as:

$$\sqrt{\frac{1}{\tilde{\rho}}}\delta^2\tan(\frac{\theta}{2})\approx V_0\frac{t}{d_n} \tag{D.9}$$

The relationship between penetration length z and time t can be obtained:

$$z\approx\left(\frac{\rho_l V_0^2}{\rho_g}\right)^{0.25}\left(\frac{td_n}{\tan(\frac{\theta}{2})}\right)^{0.5} \tag{D.10}$$

Equation (D.10) can written into:

$$z\approx\left(\frac{2\Delta P}{\rho_g}\right)^{0.25}\left(\frac{td_n}{\tan(\frac{\theta}{2})}\right)^{0.5} \tag{D.11}$$

where $V_0=(2\Delta p/\rho_l)^{0.5}$ is the constant injection velocity.

D.2 The derivation by Naber

From the derivation shown in the last section, Wakuri et al. [176] mainly focus on the steady-state spray penetration. A major difference in the derivation by Naber [56] is the use of non-dimensionalization, which will be introduced in this section. The assumptions proposed by Wakuri et al. [176] also apply to the derivation by Naber.

The fuel mass balance and overall momentum are conserved:

$$\rho_l\cdot A_l(0)\cdot V_0=\rho_l\cdot A_l(z)\cdot V(z) \tag{D.12}$$

and

$$\rho_l \cdot A_l(0) \cdot V_0^2 = \rho_l \cdot A_l(z) \cdot V(z)^2 + \rho_g \cdot A_g(z) \cdot V(z)^2 \tag{D.13}$$

The terms $A_l(0), A_l(z)$ and $A_g(z)$ represent the cross-section area of the liquid fuel at the nozzle exit, the cross-section areas of liquid fuel and ambient gas at location z, respectively.

The cross-sectional area of the jet at location z occupied by air is:

$$A_g(z) = A(z) - a_0 \cdot A_l(z) \tag{D.14}$$

The area $A(z)$ is the total cross-sectional area of the jet at z and a_0 is a parameter with a value of 0 or 1.

The $V(z)$ can be expressed in terms of $A_l(0)$, $A(z)$, V_0 by combining Eqs. (D.12)-(D.14):

$$V(z) = \frac{V_0}{2} \cdot \frac{A_l(0)}{A(z)} \cdot \left(\frac{\rho_l}{\rho_g} - a_0\right)\left(\sqrt{1 + 4 \cdot \frac{\frac{A(z)}{A_l(0)} \cdot \frac{\rho_l}{\rho_g}}{(\frac{\rho_l}{\rho_g} - a_0)^2}} - 1\right) \tag{D.15}$$

Equation (D.15) can be simplified to the non-dimensionalized form:

$$\frac{d\tilde{z}}{d\tilde{t}} = \frac{2}{\sqrt{1 + 16\tilde{z}^2} + 1} \tag{D.16}$$

by considering the follow equations

$$\begin{aligned}
z_0 &= \frac{a_0}{2} \cdot \frac{d_n}{\tan(\frac{\theta}{2})} \\
z' &= z + z_0 \\
\frac{dz'}{dt'} &= \frac{dz}{dt} = V(z) \\
A(z) &= \pi \cdot [z' \cdot \tan(\frac{\theta}{2})]^2 \\
A_l(0) &= \frac{\pi}{4} d_n^2 \\
z^+ &= d_n \cdot \sqrt{\tilde{\rho}} \cdot (\frac{\tilde{\rho} - a_0}{\tilde{\rho}}) \frac{1}{\tan(\frac{\theta}{2})} \\
t^+ &= d_n \cdot \sqrt{\tilde{\rho}} \cdot (\frac{\tilde{\rho} - a_0}{\tilde{\rho}}) \frac{1}{V_0 \tan(\frac{\theta}{2})} \\
\tilde{z} &= z'/z^+ \\
\tilde{t} &= t'/t^+
\end{aligned}$$

Integrating Eq. (D.16) from from $\tilde{z} = 0$ to $\tilde{z} = \tilde{S}$ ($\tilde{S} = S'/z^+$), the relationship between the dimensionless time and dimensionless penetration is expressed as:

$$\tilde{t} = \frac{\tilde{S}}{2} + \frac{\tilde{S}}{4} \cdot \sqrt{1 + 16\tilde{S}^2} + \frac{1}{16} \cdot \ln\left(4 \cdot \tilde{S} + \sqrt{1 + 16\tilde{S}^2}\right) \tag{D.17}$$

When $\tilde{t}$ approaches zero (i.e., near nozzle region), the relationship for the short time limit is:

$$\lim_{\tilde{t} \to 0} \quad \Big| \quad \tilde{S} = \tilde{t} \tag{D.18}$$

When $\tilde{t}$ approaches infinity (i.e., far field downstream the nozzle), the relationship for the long time limit is:

$$\lim_{\tilde{t} \to \infty} \quad \Big| \quad \tilde{S} = \tilde{t}^{1/2} \tag{D.19}$$

This method shows that the spray penetration first has a linear dependence on time and then converts to a square root dependence for a longer time. As discussed in Chapter 4, the spray is dominated by the injected liquid fuel in the early stage and then dominated by the entrained gas.

References

[1] John B Heywood. *Internal combustion engine fundamentals*. McGraw-Hill Education, 2018.

[2] RD Reitz, H Ogawa, R Payri, T Fansler, S Kokjohn, Y Moriyoshi, AK Agarwal, D Arcoumanis, D Assanis, C Bae, et al. *IJER editorial: The future of the internal combustion engine*. International Journal of Engine Research, 21(1):3–10, 2020.

[3] B Looney. *Statistical Review of World Energy 2020*. 2020.

[4] Thomas Stocker. *Climate change 2013: the physical science basis: Working Group I contribution to the Fifth assessment report of the Intergovernmental Panel on Climate Change*. Cambridge university press, 2014.

[5] MS Eide and Ø Endresen. *Assessment of measures to reduce future CO2 emissions from shipping*. Position Paper, 5, 2010.

[6] JoAnn Slama Lighty, John M Veranth, and Adel F Sarofim. *Combustion aerosols: factors governing their size and composition and implications to human health*. Journal of the Air & Waste Management Association, 50(9):1565–1618, 2000.

[7] Hannah Ritchie and Max Roser. *CO2 and Greenhouse Gas Emissions*. Our World in Data, 2017.

[8] J Berkeley. *The death of the internal combustion engine*. The Economist, 12, 2017.

[9] Reed T Doucette and Malcolm D McCulloch. *Modeling the CO2 emissions from battery electric vehicles given the power generation mixes of different countries*. Energy Policy, 39(2):803–811, 2011.

[10] Jana Hofmann, Dabo Guan, Konstantinos Chalvatzis, and Hong Huo. *Assessment of electrical vehicles as a successful driver for reducing CO2 emissions in China*. Applied energy, 184:995–1003, 2016.

[11] Xinmei Yuan, Lili Li, Huadong Gou, and Tingting Dong. *Energy and environmental impact of battery electric vehicle range in China*. Applied Energy, 157:75–84, 2015.

[12] Gilles Decan. *Towards a framework for optimizing dual-fuel engines: computing in-cylinder heat transfer and modeling dual-fuel combustion*. PhD thesis, Ghent University, 2020.

[13] Troy R Hawkins, Bhawna Singh, Guillaume Majeau-Bettez, and Anders Hammer Strømman. *Comparative environmental life cycle assessment of conventional and electric vehicles*. Journal of industrial ecology, 17(1):53–64, 2013.

[14] Da Deng. *Li-ion batteries: basics, progress, and challenges*. Energy Science & Engineering, 3(5):385–418, 2015.

[15] Elsa A Olivetti, Gerbrand Ceder, Gabrielle G Gaustad, and Xinkai Fu. *Lithium-ion battery supply chain considerations: analysis of potential bottlenecks in critical metals*. Joule, 1(2):229–243, 2017.

[16] Linda Gaines. *The future of automotive lithium-ion battery recycling: Charting a sustainable course*. Sustainable Materials and Technologies, 1:2–7, 2014.

[17] Gautam Kalghatgi. *Is it really the end of internal combustion engines and petroleum in transport?* Applied energy, 225:965–974, 2018.

[18] Tobias Gustafsson and Anders Johansson. *Comparison between Battery Electric Vehicles and Internal Combustion Engine Vehicles fueled by Electrofuels-From an energy efficiency and cost perspective*. Master's thesis, Chalmers University of Technology, 2015.

[19] IMO. *Third IMO GHG Study 2014 - Executive Summary and Final Report*. International Maritime Organization (IMO), 2014.

[20] Jiaojun Deng, Xiaochen Wang, Zhilong Wei, Li Wang, Chenyu Wang, and Zhenbin Chen. *A review of NOx and SOx emission reduction technologies for marine diesel engines and the potential evaluation of liquefied natural gas fuelled vessels*. Science of The Total Environment, page 144319, 2020.

[21] Lokukaluge P Perera and Brage Mo. *Emission control based energy efficiency measures in ship operations*. Applied Ocean Research, 60:29–46, 2016.

[22] Simone Lion, Ioannis Vlaskos, and Rodolfo Taccani. *A review of emissions reduction technologies for low and medium speed marine Diesel engines and their potential for waste heat recovery*. Energy Conversion and Management, 207:112553, 2020.

[23] R Miller and HU Lieberherr. *The Miller supercharging system for diesel and gas engines operating characteristics*. CIMAC proceedings, Zurich, pages 787–803, 1957.

[24] Roel Verschaeren, Wouter Schaepdryver, Thomas Serruys, Marc Bastiaen, Lieven Vervaeke, and Sebastian Verhelst. *Experimental study of NOx reduction on a medium speed heavy duty diesel engine by the application of EGR (exhaust gas recirculation) and Miller timing*. Energy, 76:614–621, 2014.

[25] Sipeng Zhu, Bo Hu, Sam Akehurst, Colin Copeland, Andrew Lewis, Hao Yuan, Ian Kennedy, Johan Bernards, and Ciaran Branney. *A review of water injection applied on the internal combustion engine*. Energy conversion and management, 184:139–158, 2019.

[26] Shaolong Yang, Xinxiang Pan, Zhitao Han, Dongsheng Zhao, Bojun Liu, Dekang Zheng, and Zhijun Yan. *Removal of NOx and SO2 from simulated ship emissions using wet scrubbing based on seawater electrolysis technology*. Chemical Engineering Journal, 331:8–15, 2018.

[27] Selma Brynolf, Maria Taljegard, Maria Grahn, and Julia Hansson. *Electrofuels for the transport sector: A review of production costs*. Renewable and Sustainable Energy Reviews, 81:1887–1905, 2018.

[28] Jeroen Dierickx, Louis Sileghem, and Sebastian Verhelst. *Efficiency and emissions of a high-speed marine diesel engine converted to dual-fuel operation with methanol*. In CIMAC World Congress on Combustion Engine. CIMAC, 2019.

[29] Jeroen Dierickx, Jip Verbiest, Tom Janvier, Jens Peeters, Louis Sileghem, and Sebastian Verhelst. *Retrofitting a high-speed marine engine to dual-fuel methanol-diesel operation: A comparison of multiple and single point methanol port injection*. Fuel Communications, 7:100010, 2021.

[30] Pablo García Valladolid, Per Tunestål, Javier Monsalve-Serrano, Antonio García, and Jari Hyvönen. *Impact of diesel pilot distribution on the ignition process of a dual fuel medium speed marine engine*. Energy Conversion and Management, 149:192–205, 2017.

[31] Wei Fang, Bin Huang, David B Kittelson, and William F Northrop. *Dual-fuel diesel engine combustion with hydrogen, gasoline, and ethanol as fumigants: effect of diesel injection timing*. Journal of engineering for gas turbines and power, 136(8), 2014.

[32] Pavlos Dimitriou and Rahat Javaid. *A review of ammonia as a compression ignition engine fuel*. International Journal of Hydrogen Energy, 45(11):7098–7118, 2020.

[33] Aaron J Reiter and Song-Charng Kong. *Combustion and emissions characteristics of compression-ignition engine using dual ammonia-diesel fuel*. Fuel, 90(1):87–97, 2011.

[34] Bernard Challen and Rodica Baranescu. *Diesel engine reference book*. McFarland, 1999.

[35] Konrad Reif. *Diesel engine management*. Springer, 2014.

[36] Dawei Wang, Lei Shi, Sipeng Zhu, Bo Liu, Yuehua Qian, and Kangyao Deng. *Numerical and thermodynamic study on effects of high and low pressure exhaust gas recirculation on turbocharged marine low-speed engine*. Applied Energy, 261:114346, 2020.

[37] Global Market Insights. *Marine Diesel Engine Market Size By Technology, By Application*. Global Market Insights, 2020.

[38] Gilles Decan, Tommaso Lucchini, Gianluca DErrico, and Sebastian Verhelst. *A novel technique for detailed and time-efficient combustion modeling of fumigated dual-fuel internal combustion engines*. Applied Thermal Engineering, page 115224, 2020.

[39] Xinyi Zhou, Tie Li, Zheyuan Lai, and Bin Wang. *Theoretical study on similarity of diesel combustion*. Technical report, SAE Technical Paper, 2018.

[40] Christos Chryssakis and Lambros Kaiktsis. *Evaluation of Fuel Spray Atomization Models for Conditions Applicable to Large Marine Diesel Engines*. In 22nd European Conference on Liquid Atomization and Spray Systems, 2008.

[41] Haohan Li, Roel Verschaeren, Gilles Decan, Tarek Beji, and Sebastian Verhelst. *Evaluation of breakup models for marine diesel spray simulations*. In 29th European Conference on Liquid Atomization & Spray Systems, 2019.

[42] Reto Balz, Beat von Rotz, and David Sedarsky. *In-nozzle flow and spray characteristics of large two-stroke marine diesel fuel injectors*. Applied Thermal Engineering, 180:115809, 2020.

[43] Beat Von Rotz. *Experimental investigation of spray characteristics and ignition processes at conditions representative of large two-stroke marine diesel engines*. PhD thesis, ETH Zurich, 2015.

[44] Haiqiao Wei, Xi Chen, Guofu Wang, Lei Zhou, Shijia An, and Gequn Shu. *Effect of swirl flow on spray and combustion characteristics with heavy fuel oil under two-stroke marine engine relevant conditions*. Applied Thermal Engineering, 124:302–314, 2017.

[45] Lei Zhou, Aifang Shao, Haiqiao Wei, and Xi Chen. *Sensitivity analysis of heavy fuel oil spray and combustion under low-speed marine engine-like conditions*. Energies, 10(8):1223, 2017.

[46] John E Dec. *A conceptual model of Dl Diesel combustion based on laser-sheet imaging*. SAE transactions, pages 1319–1348, 1997.

[47] Dennis L Siebers. *Recent developments on diesel fuel jets under quiescent conditions*. In Flow and combustion in reciprocating engines, pages 257–308. Springer, 2008.

[48] John E Dec and Edward B Coy. *OH radical imaging in a DI diesel engine and the structure of the early diffusion flame*. In SAE Technical Paper, pages 1127–1148. SAE International, 1996.

[49] Patrick F Flynn, Russell P Durrett, Gary L Hunter, Axel O zur Loye, Omowoleola C Akinyemi, John E Dec, and Charles K Westbrook. *Diesel combustion: an integrated view combining laser diagnostics, chemical kinetics, and empirical validation*. SAE transactions, pages 587–600, 1999.

[50] B YA. *The oxidation of nitrogen in combustion and explosions*. Acta Physicochim. URSS, 21:557, 1946.

[51] Richard Stone. *Introduction to internal combustion engines*. 1999.

[52] Mark PB Musculus, Paul C Miles, and Lyle M Pickett. *Conceptual models for partially premixed low-temperature diesel combustion*. Progress in energy and combustion science, 39(2-3):246–283, 2013.

[53] Mark PB Musculus and Kyle Kattke. *Entrainment waves in diesel jets*. SAE International Journal of Engines, 2(1):1170–1193, 2009.

[54] ALIREZA GHASEMI KHOURINIA. *Numerical simulation of non-reactive evaporative Diesel sprays using OpenFOAM*. 2017.

[55] Dennis L Siebers. *Liquid-phase fuel penetration in diesel sprays*. SAE transactions, pages 1205–1227, 1998.

[56] Jeffrey D Naber and Dennis L Siebers. *Effects of gas density and vaporization on penetration and dispersion of diesel sprays*. SAE transactions, pages 82–111, 1996.

[57] Dennis L Siebers. *Scaling liquid-phase fuel penetration in diesel sprays based on mixing-limited vaporization*. SAE transactions, pages 703–728, 1999.

[58] Raul Payri, Jaime Gimeno, Gabriela Bracho, and Daniel Vaquerizo. *Study of liquid and vapor phase behavior on Diesel sprays for heavy duty engine nozzles*. Applied Thermal Engineering, 107:365–378, 2016.

[59] Raul Payri, Jaime Gimeno, Juan P Viera, and Alejandro H Plazas. *Needle lift profile influence on the vapor phase penetration for a prototype diesel direct acting piezoelectric injector*. Fuel, 113:257–265, 2013.

[60] Lyle M Pickett, Caroline L Genzale, Gilles Bruneaux, Louis-Marie Malbec, Laurent Hermant, Caspar Christiansen, and Jesper Schramm. *Comparison of diesel spray combustion in different high-temperature, high-pressure facilities*. SAE International Journal of Engines, 3(2):156–181, 2010.

[61] Lyle Pickett, Gilles Bruneaux, and Raul Payri. *Engine combustion network special issue*. 2020.

[62] Jesús Benajes, Raúl Payri, Michele Bardi, and Pedro Martí-Aldaraví. *Experimental characterization of diesel ignition and lift-off length using a single-hole ECN injector*. Applied thermal engineering, 58(1-2):554–563, 2013.

[63] Jose V Pastor, Jose M Garcia-Oliver, Antonio Garcia, and Andrés Morales López. *An experimental investigation on spray mixing and combustion characteristics for spray C/D nozzles in a constant pressure vessel*. Technical report, SAE Technical Paper, 2018.

[64] Tiemin Xuan, Jose M Desantes, Jose V Pastor, and Jose M Garcia-Oliver. *Soot temperature characterization of spray a flames by combined extinction and radiation methodology*. Combustion and Flame, 204:290–303, 2019.

[65] Scott A Skeen, Julien Manin, Lyle M Pickett, Emre Cenker, Gilles Bruneaux, Katsufumi Kondo, Tets Aizawa, Fredrik Westlye, Kristine Dalen, Anders Ivarsson, et al. *A progress review on soot experiments and modeling in the engine combustion network (ECN)*. SAE International Journal of Engines, 9(2):883–898, 2016.

[66] Noud Maes, Scott A Skeen, Michele Bardi, Russell P Fitzgerald, Louis-Marie Malbec, Gilles Bruneaux, Lyle M Pickett, Koji Yasutomi, and Glen Martin. *Spray penetration, combustion, and soot formation characteristics of the ECN Spray C and Spray D injectors in multiple combustion facilities*. Applied Thermal Engineering, page 115136, 2020.

[67] Lyle M Pickett, Julien Manin, Caroline L Genzale, Dennis L Siebers, Mark PB Musculus, and Cherian A Idicheria. *Relationship between diesel fuel spray vapor penetration/dispersion and local fuel mixture fraction*. SAE International Journal of Engines, 4(1):764–799, 2011.

[68] R Novella, A García, José Manuel Pastor, and V Domenech. *The role of detailed chemical kinetics on CFD diesel spray ignition and combustion modelling*. Mathematical and Computer Modelling, 54(7-8):1706–1719, 2011.

[69] Sibendu Som, Gianluca D'Errico, Douglas Longman, and Tommaso Lucchini. *Comparison and standardization of numerical approaches for the prediction of non-reacting and reacting diesel sprays*. Technical report, SAE Technical Paper, 2012.

[70] Qingluan Xue, Michele Battistoni, Sibendu Som, Shaoping Quan, PK Senecal, Eric Pomraning, and David Schmidt. *Eulerian CFD modeling of coupled nozzle flow and spray with validation against X-ray radiography data*. SAE International Journal of Engines, 7(2):1061–1072, 2014.

[71] Yuanjiang Pei, Evatt R Hawkes, Sanghoon Kook, Graham M Goldin, and Tianfeng Lu. *Modelling n-dodecane spray and combustion with the transported probability density function method*. Combustion and Flame, 162(5):2006–2019, 2015.

[72] Haiqiao Wei, Xi Chen, Wanhui Zhao, Lei Zhou, and Rui Chen. *Effects of the turbulence model and the spray model on predictions of the n-heptane jet fuel–air mixing and the ignition characteristics with a reduced chemistry mechanism*. Proceedings of the Institution of Mechanical Engineers, Part D: Journal of Automobile Engineering, 231(14):1877–1888, 2017.

[73] A Pandal, Raul Payri, José M García-Oliver, and JM Pastor. *Optimization of spray break-up CFD simulations by combining Σ-Y Eulerian atomization model with a response surface methodology under diesel engine-like conditions (ECN Spray A)*. Computers & Fluids, 156:9–20, 2017.

[74] Louis Nicholson, Xiaohang Fang, Joseph Camm, Martin Davy, and David Richardson. *Comparison of Transient Diesel Spray Break-Up between Two*

Computational Fluid Dynamics Codes. Technical report, SAE Technical Paper, 2018.

[75] U Waldenmaier, J Metzger, P Porten, P Stiech, T Heidenreich, and U Wagner. *Optical and numerical investigations of the combustion process in a single cylinder medium speed diesel engine*. In 26th CIMAC Congress, 2010.

[76] Jin Xia, Zhong Huang, Leilei Xu, Dehao Ju, and Xingcai Lu. *Experimental study on spray and atomization characteristics under subcritical, transcritical and supercritical conditions of marine diesel engine*. Energy Conversion and Management, 195:958–971, 2019.

[77] Wenzheng Zhang, Xiang Li, Li Huang, and Mingzhi Feng. *Experimental study on spray and evaporation characteristics of diesel-fueled marine engine conditions based on optical diagnostic technology*. Fuel, 246:454–465, 2019.

[78] Hiroyuki Hiroyasu, Masataka Arai, and Michihiko Tabata. *Empirical equations for the sauter mean diameter of a diesel spray*. SAE transactions, pages 868–877, 1989.

[79] George Anitescu, Ronghong Lin, and Lawrence L Tavlarides. *Preparation, injection and combustion of supercritical fluids*. In Directions in Engine-Efficiency and Emissions Research (DEER) Conference, Dearborn, MI, 2009.

[80] Ronghong Lin and Lawrence L Tavlarides. *Thermophysical properties needed for the development of the supercritical diesel combustion technology: Evaluation of diesel fuel surrogate models*. The Journal of Supercritical Fluids, 71:136–146, 2012.

[81] Ronghong Lin. *Issues on clean diesel combustion technology using supercritical fluids: Thermophysical properties and thermal stability of diesel fuel*. PhD thesis, Syracuse University, 2011.

[82] Jin Xia, Zhong Huang, Lijun Zhang, Qiankun Zhang, Liang Zheng, Rui Liu, Dehao Ju, and Xingcai Lu. *Experimental comparisons on injection and atomization characteristics of diesel and its six-component surrogate under different critical conditions of marine engine*. Energy Conversion and Management, 205:112397, 2020.

[83] Jin Xia, Qiankun Zhang, Zhong Huang, Dehao Ju, and Xingcai Lu. *Experimental study of injection characteristics under diesels sub/trans/supercritical conditions with various nozzle diameters and injection pressures*. Energy Conversion and Management, 215:112949, 2020.

[84] Zhong Huang, Wenzheng Zhang, Jin Xia, Dehao Ju, and Xingcai Lu. *A multi-component surrogate of commercial diesel for trans-critical and supercritical injections study*. Fuel, 243:590–602, 2019.

[85] Jose M Desantes, Jose V Pastor, Raul Payri, and Jose M Pastor. *Experimental characterization of internal nozzle flow and diesel spray behavior. Part II: evaporative conditions*. Atomization and sprays, 15(5), 2005.

[86] Hiro Hiroyasu and Masataka Arai. *Structures of fuel sprays in diesel engines*. SAE transactions, pages 1050–1061, 1990.

[87] Francisco Ruiz and Norman Chigier. *Parametric experiments on liquid jet atomization spray angle*. Atomization and Sprays, 1(1), 1991.

[88] Roel Verschaeren. *An Optical Study of Evaporating Fuel Sprays for Medium Speed Engines*. PhD thesis, Ghent University, 2019.

[89] Jonas Galle, Joachim Demuynck, Jeroen Vancoillie, and Sebastian Verhelst. *Spray parameter comparison between diesel and vegetable oils for non-evaporating conditions*. Technical report, SAE Technical Paper, 2012.

[90] Jonas Galle, Christophe Van De Maele, Sander Defruyt, Sebastian Verhelst, and Roel Verschaeren. *Evaluation of Some Important Boundary Conditions for Spray Measurements in a Constant Volume Combustion Chamber*. Technical report, SAE Technical Paper, 2013.

[91] Jaime Gimeno, Gabriela Bracho, Pedro Martí-Aldaraví, and Jesús E Peraza. *Experimental study of the injection conditions influence over n-dodecane and diesel sprays with two ECN single-hole nozzles. Part I: Inert atmosphere*. Energy conversion and management, 126:1146–1156, 2016.

[92] Raul Payri, Francisco Javier Salvador, Jaime Gimeno, and Jesús E Peraza. *Experimental study of the injection conditions influence over n-dodecane and diesel sprays with two ECN single-hole nozzles. Part II: Reactive atmosphere*. Energy conversion and management, 126:1157–1167, 2016.

[93] Lyle M Pickett, Sanghoon Kook, and Timothy C Williams. *Visualization of diesel spray penetration, cool-flame, ignition, high-temperature combustion, and soot formation using high-speed imaging*. SAE international journal of engines, 2(1):439–459, 2009.

[94] Peter M Lillo, Lyle M Pickett, Helena Persson, Oivind Andersson, and Sanghoon Kook. *Diesel spray ignition detection and spatial/temporal correction*. SAE International Journal of Engines, 5(3):1330–1346, 2012.

[95] Haobu Gao, Xiangrong Li, Jiye Xue, Honglin Bai, Xu He, and Fushui Liu. *A modification to the WAVE breakup model for evaporating diesel spray*. Applied Thermal Engineering, 108:555–566, 2016.

[96] Sanghoon Kook, Minh Khoi Le, Srinivas Padala, and Evatt R Hawkes. *Z-type Schlieren setup and its application to high-speed imaging of gasoline sprays*. 2011.

[97] Zhaowen Wang, Shuguo Shi, Sheng Huang, Jie Tang, Tao Du, Xiaobei Cheng, Ronghua Huang, and Jyh-Yuan Chen. *Effects of water content on evaporation and combustion characteristics of water emulsified diesel spray*. Applied energy, 226:397–407, 2018.

[98] SE Parrish and RJ Zink. *Development and application of a high-speed planar laser-induced fluorescence imaging system to evaluate liquid and vapor phases of sprays from a multi-hole diesel fuel injector*. Measurement Science and Technology, 24(2):025402, 2012.

[99] Jose Pastor, Jose M Garcia-Oliver, Antonio Garcia, Wenjun Zhong, Carlos Micó, and Tiemin Xuan. *An experimental study on diesel spray injection into a non-quiescent chamber*. SAE International Journal of Fuels and Lubricants, 10(2):394–406, 2017.

[100] Jonas Galle. *Spray atomization of alternative fuels in medium speed diesel engines*. PhD thesis, Ghent University, 2013.

[101] F Payri, Raul Payri, MICHELE Bardi, and M Carreres. *Engine combustion network: influence of the gas properties on the spray penetration and spreading angle*. Experimental Thermal and Fluid Science, 53:236–243, 2014.

[102] Adrian Sabau. *Pressure Waves Simulation in Diesel Engine Injection System*. In Advanced Materials Research, volume 837, pages 477–482. Trans Tech Publ, 2014.

[103] Jose V Pastor, Raul Payri, Jose M Garcia-Oliver, and Francisco J Briceno. *Analysis of transient liquid and vapor phase penetration for diesel sprays under variable injection conditions*. Atomization and Sprays, 21(6):503–520, 2011.

[104] Rolf D Reitz. *Modeling atomization processes in high-pressure vaporizing sprays*. Atomisation and Spray Technology, 3(4):309–337, 1987.

[105] TF Su, MA Patterson, Rolf D Reitz, and PV Farrell. *Experimental and numerical studies of high pressure multiple injection sprays*. SAE transactions, pages 1281–1292, 1996.

[106] Carsten Baumgarten. *Mixture formation in internal combustion engines*. Springer Science & Business Media, 2006.

[107] Ruitian He, Ping Yi, Tie Li, Xinyi Zhou, and Yumeng Gu. *Evaluations of the KH-RT breakup and dynamic structure SGS models for evaporating sprays under diesel engine-like conditions*. Atomization and Sprays, 30(3), 2020.

[108] S Som and Suresh Aggarwal. *Assessment of atomization models for diesel engine simulations*. Atomization and Sprays, 19(9), 2009.

[109] S Som, AI Ramirez, SK Aggarwal, AL Kastengren, E El-Hannouny, DE Longman, CF Powell, and PK Senecal. *Development and validation of a primary breakup model for diesel engine applications*. Technical report, SAE Technical Paper, 2009.

[110] S Som and SK Aggarwal. *Effects of primary breakup modeling on spray and combustion characteristics of compression ignition engines*. Combustion and Flame, 157(6):1179–1193, 2010.

[111] Balaji Mohan, Wenming Yang, and Siaw kiang Chou. *Development of an accurate cavitation coupled spray model for diesel engine simulation*. Energy conversion and management, 77:269–277, 2014.

[112] AI Ramirez, S Som, Suresh K Aggarwal, AL Kastengren, EM El-Hannouny, DE Longman, and CF Powell. *Quantitative X-ray measurements of high-pressure fuel sprays from a production heavy duty diesel injector*. Experiments in fluids, 47(1):119–134, 2009.

[113] AI Ramirez, S Som, SK Aggarwal, AL Kastengren, EM El-Hannouny, DE Longman, and CF Powell. *Characterizing Spray Behavior of Diesel Injection Systems Using X-Ray Radiography*. Technical report, SAE Technical Paper, 2009.

[114] Jingyu Zhu, Olawole Abiola Kuti, and Keiya Nishida. *Effects of Injection Pressure and Ambient Gas Density on Fuel-Ambient Gas Mixing and Combustion Characteristics of DI Diesel Spray*. Technical report, SAE Technical Paper, 2011.

[115] Jingyu Zhu, Olawole Abiola Kuti, and Keiya Nishida. *An investigation of the effects of fuel injection pressure, ambient gas density and nozzle hole diameter on surrounding gas flow of a single diesel spray by the laser-induced fluorescence–particle image velocimetry technique*. International Journal of Engine Research, 14(6):630–645, 2013.

[116] Cheng Gong, Mehdi Jangi, Tommaso Lucchini, Gianluca DErrico, and Xue-Song Bai. *Large eddy simulation of air entrainment and mixing in reacting and non-reacting diesel sprays*. Flow, turbulence and combustion, 93(3):385–404, 2014.

[117] Zhiyu Han and Rolf D Reitz. *Turbulence modeling of internal combustion engines using RNG κ-ε models*. Combustion science and technology, 106(4-6):267–295, 1995.

[118] Federico Perini, Kan Zha, Stephen Busch, and Rolf Reitz. *Comparison of linear, non-linear and generalized RNG-based k-epsilon models for turbulent diesel engine flows*. In SAE Technical Paper. SAE International, 2017.

[119] Anne Kösters and Anders Karlsson. *A comprehensive numerical study of diesel fuel spray formation with openfoam*. Technical report, SAE Technical Paper, 2011.

[120] Milan Vujanović, Zvonimir Petranović, Wilfried Edelbauer, and Neven Duić. *Modelling spray and combustion processes in diesel engine by using the coupled Eulerian–Eulerian and Eulerian–Lagrangian method*. Energy conversion and management, 125:15–25, 2016.

[121] Xi Jiang, GA Siamas, K Jagus, and TG Karayiannis. *Physical modelling and advanced simulations of gas–liquid two-phase jet flows in atomization and sprays*. Progress in energy and combustion science, 36(2):131–167, 2010.

[122] Patrick Jenny, Dirk Roekaerts, and Nijso Beishuizen. *Modeling of turbulent dilute spray combustion*. Progress in Energy and Combustion Science, 38(6):846–887, 2012.

[123] Fadl Moukalled, L Mangani, Marwan Darwish, et al. *The finite volume method in computational fluid dynamics*, volume 113. Springer, 2016.

[124] Akireza Ghasemi Khourinia. *Numerical simulation of non-reactive evaporative Diesel sprays using OpenFOAM*. Master's thesis, Politecnico Milano, 2017.

[125] Andrei Nikolaevich Kolmogorov. *The local structure of turbulence in incompressible viscous fluid for very large Reynolds numbers*. Proceedings of the Royal Society of London. Series A: Mathematical and Physical Sciences, 434(1890):9–13, 1991.

[126] Alessandro D'Ausilio. *Numerical Study of a Turbulent Spray Flame with Large Eddy Simulations Coupled with the Conditional Moment Closure Method*. PhD thesis, Ghent University, 2020.

[127] Cedomir Kralj. *Numerical simulation of Diesel spray processes*. PhD thesis, Imperial College, University of London, 1995.

[128] Yoshihide Tominaga and Ted Stathopoulos. *Turbulent Schmidt numbers for CFD analysis with various types of flowfield*. Atmospheric Environment, 41(37):8091–8099, 2007.

[129] Daniel Valero and Daniel B Bung. *Sensitivity of turbulent Schmidt number and turbulence model to simulations of jets in crossflow*. Environmental Modelling & Software, 82:218–228, 2016.

[130] Christopher J Greenshields. *OpenFOAM user guide*. OpenFOAM Foundation Ltd, version, 3(1):47, 2015.

[131] Rolf D Reitz and R Diwakar. *Structure of high-pressure fuel sprays*. SAE transactions, pages 492–509, 1987.

[132] SS Hwang, Z Liu, and Rolf D Reitz. *Breakup mechanisms and drag coefficients of high-speed vaporizing liquid drops*. Atomization and Sprays, 6(3), 1996.

[133] Sergei Sazhin. *Droplets and sprays*, volume 345. Springer, 2014.

[134] Jun Xin, L Ricart, and RD Reitz. *Computer modeling of diesel spray atomization and combustion*. Combustion science and technology, 137(1-6):171–194, 1998.

[135] Rickard Solsjö and Xue-Song Bai. *Injection of fuel at high pressure conditions: Les study*. Technical report, SAE Technical Paper, 2011.

[136] Mark A Patterson and Rolf D Reitz. *Modeling the effects of fuel spray characteristics on diesel engine combustion and emission*. SAE transactions, pages 27–43, 1998.

[137] Sibendu Som and Suresh K Aggarwal. *A numerical investigation of non-evaporating and evaporating diesel sprays*. In ASME 2008 International Mechanical Engineering Congress and Exposition, pages 281–290. American Society of Mechanical Engineers Digital Collection, 2008.

[138] PA Niklas Nordin. *Complex chemistry modeling of diesel spray combustion*. PhD thesis, Chalmers University of Technology Sweden, 2001.

[139] AA Amsden, JD Ramshaw, PJ O'rourke, and JK Dukowicz. *KIVA: A computer program for two-and three-dimensional fluid flows with chemical reactions and fuel sprays*. Technical report, Los Alamos National Lab., NM (USA), 1985.

[140] R Byron Bird. *Transport phenomena*. Appl. Mech. Rev., 55(1):R1–R4, 2002.

[141] W. E. Ranz and W. R. Marshall. *Evaporation from drops, Parts I*. Chem Eng Prog., 48:141–146, 1952.

[142] W. E. Ranz and W. R. Marshall. *Evaporation from drops, Parts II*. Chem Eng Prog., 48:173–180, 1952.

[143] Tommaso Lucchini, Gianluca D'Errico, F Brusiani, and Bianchi GM. *A Finite-Element Based Mesh Motion Technique For Internal Combustion Engine Simulations (MS: Modeling and Simulation, General Session Papers)*. In The Proceedings of the International symposium on diagnostics and modeling of combustion in internal combustion engines 2008.7, pages 671–678. The Japan Society of Mechanical Engineers, 2008.

[144] Tommaso Lucchini, Gianluca DErrico, Daniele Ettorre, and Giancarlo Ferrari. *Numerical investigation of non-reacting and reacting diesel sprays in constant-volume vessels*. SAE International Journal of Fuels and Lubricants, 2(1):966–975, 2009.

[145] Tommaso Lucchini, Gianluca DErrico, and Daniele Ettorre. *Numerical investigation of the spray–mesh–turbulence interactions for high-pressure, evaporating sprays at engine conditions*. International Journal of Heat and Fluid Flow, 32(1):285–297, 2011.

[146] Gilles Decan, Stijn Broekaert, Tommaso Lucchini, Gianluca DErrico, Jan Vierendeels, and Sebastian Verhelst. *Evaluation of wall heat flux calculation methods for CFD simulations of an internal combustion engine under both motored and HCCI operation*. Applied energy, 232:451–461, 2018.

[147] Federico Piscaglia, Andrea Montorfano, Gianluca Montenegro, Angelo Onorati, H Jasak, H Rusche, et al. *Lib-ICE: a C++ object oriented library for ICE simulation-acoustics and aftertreatment*. In Fifth OpenFOAM Workshop, Goteborg, 2011.

[148] Cherian A Idicheria and Lyle M Pickett. *Effect of EGR on diesel premixed-burn equivalence ratio*. Proceedings of the Combustion Institute, 31(2):2931–2938, 2007.

[149] Roberto Torelli. *Novel approaches for CFD modeling of diesel engines*. PhD thesis, Politecnico Milano, 2015.

[150] Amin Maghbouli. *Development of an advanced multi-dimensional CFD framework for modeling low temperature combustion in direct injection compression ignition engines*. PhD thesis, Politecnico Milano, 2017.

[151] Ehsanallah Tahmasebi. *Simulation of internal flow in fuel injection process*. PhD thesis, Politecnico Milano, 2017.

[152] Xinyi Zhou, Tie Li, Yijie Wei, and Sichen Wu. *Scaling spray combustion processes in marine low-speed diesel engines*. Fuel, 258:116133, 2019.

[153] Cheng Gong, Mehdi Jangi, and Xue-Song Bai. *Large eddy simulation of n-dodecane spray combustion in a high pressure combustion vessel*. Applied energy, 136:373–381, 2014.

[154] John K Dukowicz. *A particle-fluid numerical model for liquid sprays*. Journal of computational Physics, 35(2):229–253, 1980.

[155] Tommaso Lucchini, Augusto Della Torre, Gianluca DErrico, Angelo Onorati, Noud Maes, Lambertus MT Somers, and Gilles Hardy. *A comprehensive methodology for computational fluid dynamics combustion modeling of industrial diesel engines*. International Journal of Engine Research, 18(1-2):26–38, 2017.

[156] N Bharadwaj, CJ Rutland, and S-M Chang. *Large eddy simulation modelling of spray-induced turbulence effects*. International Journal of Engine Research, 10(2):97–119, 2009.

[157] Jonathan Brulatout, François Garnier, Christine Mounaïm-Rousselle, and Patrice Seers. *Calibration strategy of diesel-fuel spray atomization models using a design of experiment method*. International Journal of Engine Research, 17(7):713–731, 2016.

[158] Noud Maes, Nico Dam, Bart Somers, Tommaso Lucchini, Gianluca D'Errico, and Gilles Hardy. *Experimental and numerical analyses of liquid and spray penetration under heavy-duty diesel engine conditions*. SAE International Journal of Fuels and Lubricants, 9(1):108–124, 2016.

[159] Adrián Pandal Blanco. *Implementation and Development of an Eulerian Spray Model for CFD simulations of diesel Sprays*. PhD thesis, Universitat Politècnica de València, 2016.

[160] Lyle M Pickett, Caroline L Genzale, Julien Manin, Louis-Marie Malbec, and Laurent Hermant. *Measurement uncertainty of liquid penetration in evaporating diesel sprays*. ILASS2011-111, 2011.

[161] MR Turner, SS Sazhin, JJ Healey, Cyril Crua, and SB Martynov. *A breakup model for transient Diesel fuel sprays*. Fuel, 97:288–305, 2012.

[162] Xinyi Zhou, Tie Li, Ping Yi, Zhifei Zhang, Ning Wang, and Yijie Wei. *On the fuel injection rate profile as boundary conditions for diesel spray combustion simulations*. Fuel, 276:118026, 2020.

[163] J Janicka and N Peters. *Prediction of turbulent jet diffusion flame lift-off using a PDF transport equation*. In Symposium (International) on Combustion, volume 19, pages 367–374. Elsevier, 1982.

[164] J Stegemann, J Seebode, J Baltes, C Baumgarten, and GP Merker. *Influence of throttle effects at the needle seat on the spray characteristics of a multihole injection nozzle*. In Proceedings ILASS-Europe 2002, European Conference on Liquid Atomization and Spray Systems, volume 9, 2002.

[165] Arthur H Lefebvre and Vincent G McDonell. *Atomization and sprays*. CRC press, 2017.

[166] L Bayvel and Z Orzechowski. *Liquid Atomization*. Taylor & Francis, 1993.

[167] Juan Ignacio Ramos. *Internal combustion engine modeling*. Hemisphere publishing corporation, 1989.

[168] JC Dent. *A basis for the comparison of various experimental methods for studying spray penetration*. SAE Transactions, pages 1881–1884, 1971.

[169] M Arai, M Tabata, H Hiroyasu, and M Shimizu. *Disintegrating process and spray characterization of fuel jet injected by a diesel nozzle*. Technical report, SAE Technical Paper, 1984.

[170] M Arai. *Diesel spray behaviour and air entrainment*. J Nanosci Nanotechnol, 2:102, 2018.

[171] AJ Yule and I Filipovic. *On the break-up times and lengths of diesel sprays*. International journal of heat and fluid flow, 13(2):197–206, 1992.

[172] Cyril Crua, Morgan R Heikal, and Martin R Gold. *Microscopic imaging of the initial stage of diesel spray formation*. Fuel, 157:140–150, 2015.

[173] Cyril Crua, Tenzin Shoba, Morgan Heikal, Martin Gold, and Cassandra Higham. *High-speed microscopic imaging of the initial stage of diesel spray formation and primary breakup*. Technical report, SAE Technical Paper, 2010.

[174] Dohoy Jung and Dennis N Assanis. *Multi-zone DI diesel spray combustion model for cycle simulation studies of engine performance and emissions*. SAE transactions, pages 1510–1532, 2001.

[175] Engine Performance Application Manual. *Version 7.3. Westmont, IL: Gamma Technologies*. 2012.

[176] Yutaro Wakuri, Masaru Fujii, Tatsuo Amitani, and Reijiro Tsuneya. *Studies on the penetration of fuel spray in a diesel engine*. Bulletin of JSME, 3(9):123–130, 1960.

[177] Jose Maria Desantes, Raul Payri, Francisco Javier Salvador, and Antonio Gil. *Development and validation of a theoretical model for diesel spray penetration*. Fuel, 85(7-8):910–917, 2006.

[178] R Payri, S Ruiz, FJ Salvador, and J Gimeno. *On the dependence of spray momentum flux in spray penetration: Momentum flux packets penetration model*. Journal of mechanical science and technology, 21(7):1100–1111, 2007.

[179] Frank P Incropera, Adrienne S Lavine, Theodore L Bergman, and David P DeWitt. *Fundamentals of heat and mass transfer*. Wiley, 2007.

[180] Raul Payri, FJ Salvador, Jaime Gimeno, and R Novella. *Flow regime effects on non-cavitating injection nozzles over spray behavior*. International Journal of Heat and Fluid Flow, 32(1):273–284, 2011.

[181] SS Sazhin, G Feng, and MR Heikal. *A model for fuel spray penetration*. Fuel, 80(15):2171–2180, 2001.

[182] Jacek Pozorski, Sergei Sazhin, Marta Wacławczyk, Cyril Crua, David Kennaird, and Morgan Heikal. *Spray penetration in a turbulent flow*. Flow, Turbulence and Combustion, 68(2):153, 2002.

[183] Stephen B. Pope. *Turbulent Flows*. Cambridge University Press, 2000.

[184] Anthony A Amsden, Peter J Orourke, and T Daniel Butler. *KIVA-2: A computer program for chemically reactive flows with sprays*. NASA STI/recon technical report N, 89, 1989.

[185] Gunnar Stiesch. *Modeling engine spray and combustion processes*. Springer Science & Business Media, 2003.

Marine transportation is mainly powered by diesel engines.